Master of Science Thesis

Pharmacokinetic modeling for optimization of radioimmunotherapy – macroscopic and microscopic approach

Mattias Nickel

Supervisor: Sven-Erik Strand

Department of Medical Radiation Physics
Lund University

Table of contents

Abstract 3
Introduction 4
Background 6
Part A: Macroscopic model 10
    Method 10
    Results 18
    Discussion 22
Part B: Microscopic model 25
    Method 25
    Results 28
    Discussion 38
General conclusions 39
Acknowledgement 40
References 41
Appendix 48

Abstract

Purpose: For evaluation, development and optimization of treatment strategies in radionuclide therapy, it is useful to study and model the pharmacokinetics of the therapeutic agent. The aim of this study was to create models for describing the pharmacokinetics of monoclonal antibodies used for radioimmunotherapy.

Method: Two models, based on very different modeling approaches, are presented in this thesis. The first model is a macroscopic compartmental model, i.e. it addresses the pharmacokinetic behavior in a macroscopic scale. The model is not based on actual physiological processes, but is rather a simplified method to describe the pharmacokinetics that can be "seen" with imaging techniques. The basis for the model is measurements of activity distributions in a clinical study of radioimmunotherapy of B-cell lymphoma, and the parameters of the model is iteratively calculated by the model fitting to these data. In the clinical study, extracorporeal adsorbtion (ECAT) is used to lower the radiation dose to the normal organs and improve the therapeutic ratio. This is also implemented in the model as a perturbation, and evaluated.

The second model is a microscopic pharmacokinetic model for studying the pharmacokinetics in a small prevascular tumor nodule, for example a micrometastases. The model is theoretical and based on physiological parameters and the basic mechanisms of transport. The effect of ECAT is evaluated in the microscopic scale and an investigation is made on how the different parameters of the model influence the accumulation of antibodies in the nodule.

Results: The macroscopic compartmental model is successfully fit to the clinical data. In the case of therapy, the model could accurately describe the measured data during the ECAT procedure. By fitting the model to diagnostic data and add the ECAT procedure as a perturbation to the model, the therapeutic data could be predicted. In the microscopic model, it is found that the time for saturation of a microscopic cluster of tumor cells could be described as a simple function of the model parameters.

Conclusion: The overall good fit to the therapy data indicates that the macroscopic model in fact, despite its simplicity, is suitable for describing the pharmacokinetics of monoclonal antibodies in radioimmunotherapy. As the measured therapy data could be predicted by the use of diagnostic data by adding ECAT as a perturbation to the model, it might become useful as a tool for evaluation and optimization of clinical strategies. The microscopic pharmacokinetic model can be used, by combining it with dosimetry, to optimize and evaluate different treatment strategies in the microscopic scale.

Introduction

For a disseminated or diffuse malignant disease a systemic approach to treatment is required. The goal to find selective and systemic therapy cannot be achieved by physical means; it requires exploitation of the biological differences between cancerous and noncancerous cells. Biologically targeted tumor radiotherapy is selectively delivery of curative doses of radiation to malignant sites. In radioimmunotherapy, monoclonal antibodies or their fragments is used for targeting the cancer cells [O'Donoghue 2000].

By studying the pharmacokinetics of the targeting agent, the treatment strategies can be evaluated and optimized [Strand et al 1993]. Optimization for radioimmunotherapy includes finding optimal combinations of pharmacokinetics, for example monoclonal antibodies and fragments with the desired properties [Slavin-Chiorini et al 2000], and physics, for example choosing a radionuclide or combination of radionuclides with desired emission properties and half-life [O'Donoghue 2000].

Optimization may also include strategies for altering the pharmacokinetics during the treatment procedure. This includes concepts as extracorporeal adsorption (ECAT) [Strand et al 2000] or pretargeting techniques [Chinol et al 2000]. ECAT is a method to reduce the concentration of antibodies in the plasma to lower the toxic effect to normal tissues and organs. This is made by filtering the plasma or blood in an affinity column. Pretargeting techniques utilizes un-labeled antibodies for targeting the antigen sites. After allowing a time for the antibodies to bind to the tumor cells most unbound antibodies is cleared from the body. Another radiolabeled molecule is then used for targeting the original antibody.

The goal of optimizing is to find a treatment strategy that gives the highest achievable therapeutic ratio, which is the ratio of the tumor absorbed dose, to the absorbed dose to critical organs. Usually, the average absorbed dose is calculated using the MIRD S-formalism [Loevinger et al 1991] which is based on the use of averaged cumulated activity, estimated or calculated, in different tissues and organs. In the clinical situation, the absorbed dose distribution is generally not uniform because of the spatially non-uniform uptake of the targeting agent, why dosimetry based on averaged quantities may be inaccurate. Also, the ability to resolve small or microscopic lesions by imaging techniques *in vivo* is limited. Optimization should therefore include the absorbed dose spatial distribution and the absorbed dose to assumed microscopic lesions.

Parmacokinetic modeling and optimization could be used in a treatment planning process in radionuclide therapy. Such process would involve several steps (figure 1): diagnostic study of the patient, pharmacokinetic modeling of the data, dosimetry and optimization.

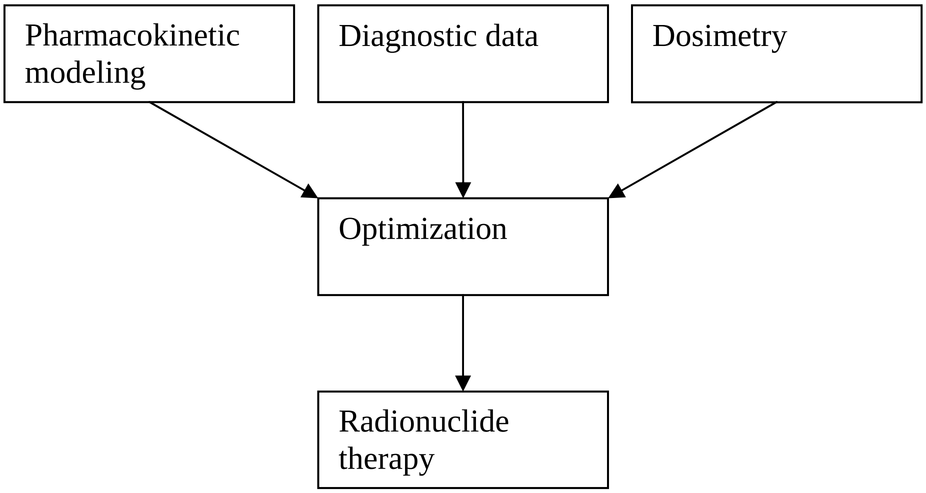

Figure 1: Schematic chart of a treatment planning process in radionuclide therapy.

Purpose of this work

The aim of this work is to create a model for describing the pharmacokinetics of monoclonal antibodies used for radioimmunotherapy. Two different approaches are used.

1. The first is a macroscopic model, based on experimental data from a clinical study of radioimmunotherapy of B-cell lymphoma patients performed in Lund. This model is used to study the overall pharmacokinetics in organs and tissues that can be visualized by external imaging. The model is simple as no values for physiological parameters of the transport are needed. As ECAT is used in this study, this is implemented in the model and used as a perturbation of the system.

2. The second approach is a theoretical model of microscopic clusters of tumor cells. The primary interest of this model is to study the pharmacokinetics in micrometastases located in the circulating plasma. These lesions are too small to be visualized by commonly used imaging techniques *in vivo*, but overall treatment strategy should be optimized including micrometastases as well. The model is based on the physical transportation properties of monoclonal antibodies (diffusion, binding to antigen sites etc.).

Background

The transport of monoclonal antibodies following a systemic administration involves four processes (figure 2): transport within the blood vessel, the transport across vascular walls into surrounding tissues (extravasation) and transport through interstitial space within the tumor [Jain].

Distribution through vascular space

The blood supply to a tumor is often chaotic. While small tumors (<2 mm in diameter) are perfused by vasculature originating from surrounding tissues, further growth of tumors often is accompanied by angiogenic response as newly formed microvessels. Tumor vasculature differs from the vasculature in normal tissues in both function and morphology; for example by being more heterogeneous in distribution with larger sized vessels and being more permeable. Based on the vasculature, three regions of the tumor are categorized; a well-vascularized periphery; a seminecrotic, intermediate zone; and an avascular, necrotic central region [Jang]. In most normal tissues, extravasated macromolecules are taken up and brought back to the central circulation by the lymphatics. Tumors, however, often lacks functional lymphatics and macromolecules must therefore be picked up by the peritumor host lymphatics [Jain].

Transport across microvascular wall

The extravasation of monoclonal antibodies occurs by diffusion and convection. The diffusive flux across the capillary wall is proportional to the vessel's surface area per unit volume, S (cm^2/cm^3), and the difference between the vascular and interstitial concentrations (c_v and c_i respectively). The diffusive flux is related to the difference in concentrations by the vascular permeability coefficient, P (cm/s):

$$\text{Diffusive flux} = PS(c_v - c_i)$$

The convection is proportional to the rate of fluid leakage from the vessel, which in turn is proportional to the vessel's surface area per unit volume (S) and the difference between the vascular and interstitial hydrostatic pressures (p_v and p_i respectively), minus the osmotic reflection coefficient (σ) times the difference between the vascular and interstitial osmotic pressures (π_v and π_i respectively). The fluid leakage is related to the pressure gradient by the hydraulic conductivity, L_p (cm/mm Hg·s) [Jain, Dvorak et al]:

$$\text{Convective flux} = L_p S[(p_v - p_i) - \sigma(\pi_v - \pi_i)]$$

Transport in tumor interstitium

The transport of antibodies in the tumor interstitial space occurs by diffusion and convection. Diffusion is movement due to concentration differences of the molecules and is proportional to the concentration gradients. The diffusive flux is related to the concentration gradients by the interstitial diffusion coefficient for the solute, D (commonly in units of cm^2/s):

$$\text{Diffusive flux} = -D\nabla c$$

with c [M] being the interstitial concentration of antibodies. Convection, movement due to pressure differences, is proportional to the interstitial fluid velocity, which in turn is related to the interstitial pressure gradients by the interstitial hydraulic conductivity, K (in units of $\mathrm{cm}^2/\mathrm{mm\,Hg\cdot s}$) [Jain].

$$\text{Convective flux} = -cR_f K\nabla p$$

R_f is a retardation factor (solute convective velocity / solvent convective velocity) [Dvorak].

The values of these parameters are determined by the structure and composition of the tumor interstitium and by the physical and chemical properties of the solute molecule [Jain].

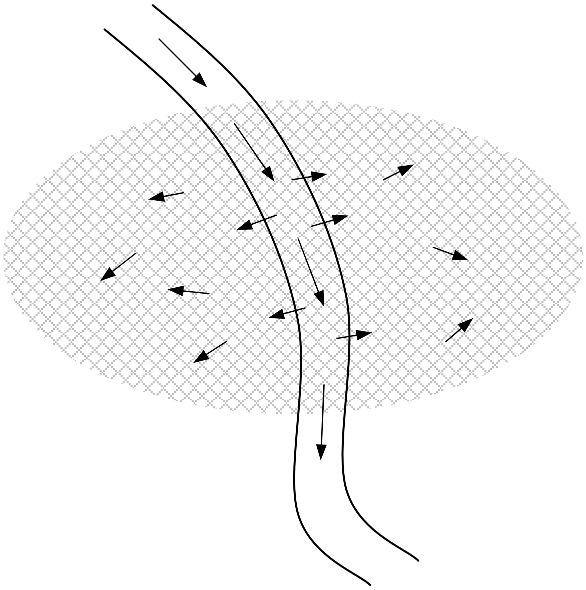

Figure 2: The transport process of systemically administered monoclonal antibodies. The transport involves distribution in the vascular space, extravasation into surrounding tissues and transport in the interstitial space.

Reaction kinetics

The binding of antibodies to antigens is considered as an elementary chemical reaction

$$c + s \underset{k_r}{\overset{k_f}{\leftrightarrow}} \overline{cs}$$

where c [M] is the concentration of antibodies, s [M] is the concentration of free antigens and $\overline{cs}$ [M] is the concentration of the antibody-antigen complex. k_f [$M^{-1}h^{-1}$] and k_r [h^{-1}] represents the forward (association) and reverse (dissociation) rate constants, respectively. The above reaction can be illustrated with a compartment model as

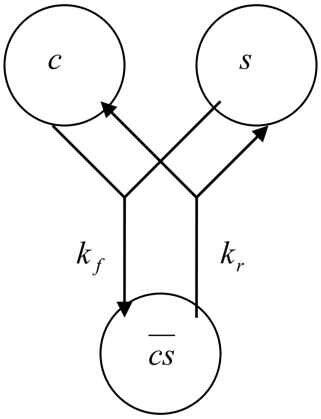

Figure 3: Schematic compartmental model for reaction kinetics where antibodies and antigens interact to form antibody-antigen complexes.

The reaction, together with the compartmental model, gives rise to a system of nonlinear ordinary differential equations of the form

$$\begin{aligned}
\frac{dc}{dt} &= -k_f cs + k_r \overline{cs} \\
\frac{ds}{dt} &= n\left(-k_f cs + k_r \overline{cs}\right) \\
\frac{d\overline{cs}}{dt} &= k_f cs - k_r \overline{cs}
\end{aligned} \qquad \textbf{(eq. 1)}$$

where n is the binding valence (i.e. the number of antigen sites that can be occupied by each antibody).

The affinity of the binding reaction is defined by

$$K_a = \frac{k_f}{k_r} \quad [M^{-1}]$$

Transport in microscopic clusters

In microscopic clusters of tumor cells (a few handred micrometers in diameter), some simplifying assumptions can be made. First of all the microscopic cluster is assumed to not contain a necrotic center [Fujimori et al 1990]. A necrotic center would make the model more complicated since the antibody kinetics would be different in the necrotic region. Secondly, flow is negligible within prevascular spheroids [Graff et al 2003], which has the consequence that there are no significant interstitial pressure gradients, making the transport to be a pure diffusion-reaction process [van Osdol et al 1991]. Also, changes in vascular concentration arising from antibody penetration into or effusion out of the cell cluster can be assumed negligible since the external plasma volume is much greater than the cell cluster volume. Antigens are assumed immobile and uniformly distributed and the diffusion rate coefficient is independent of the space variables.

The transport of antibodies in a microscopic tumor cell cluster (ignoring binding to antigen sites) can then be described by the diffusion equation (otherwise known as Fick's law),

$$\frac{\partial c}{\partial t} = \nabla \bullet \left(D \nabla c \right) \qquad \textbf{(eq. 2)}$$

where ∇ is the nabla operator (in Cartesian coordinates, $\nabla = \hat{x}\frac{\partial}{\partial x} + \hat{y}\frac{\partial}{\partial y} + \hat{z}\frac{\partial}{\partial z}$). Combining this with the reaction kinetics (eq. 1) gives the equation system that describes the temporal and spatial distribution of the antibodies, antigens and antibody-antigen complexes

$$\begin{aligned} \frac{\partial c}{\partial t} &= \nabla \bullet \left(D \nabla c \right) - k_f cs + k_r \overline{cs} \\ \frac{\partial s}{\partial t} &= n\left(-k_f cs + k_r \overline{cs} \right) \\ \frac{\partial \overline{cs}}{\partial t} &= k_f cs - k_r \overline{cs} \end{aligned} \qquad \textbf{(eq. 3)}$$

Part A: Macroscopic model

Method

Basic features

The macroscopic model presented here is an empirical multi-compartmental model, based on uptake measurements in a clinical trial of radioimmunotherapy. Opposed to a physiological based pharmacokinetic model, this model is not set to describe any actual physiological processes but rather study the overall pharmacokinetic behavior in a limited case. The reasons for using such model instead of a physiological based model are several:

1) A physiological approach would require extensive knowledge of physiological parameters in each patient, such as regional blood- and lymph flow rates to each tissue/organ, extravasation parameters (as transcapillary flow rates and permeability surface area products) for each tissue/organ, volumes of plasma and interstitial space in each tissue/organ, and antigen concentrations. The values for parameters like these are seldom possible to measure in patients.
2) The idea here is to use a model as simple as possible and se how well it can describe measured data from the clinical study and then if it can be used to predict the outcome of a perturbation as extracorporeal immunoadsorbtion.

The structure of the model is the simplest possible: every compartment describing tissue uptake is connected only to the plasma compartment. The model is also linear (with no saturable binding processes involved), with fluxes assumed to be directly proportional to the matter present in the compartment. The simplicity of the model assures a minimum of parameters to fit, keeping the degree of freedom relatively low. The purpose of the model is to see how well it can describe the measured quantities in the clinical study, and to investigate the accuracy of predictions that can be made.

There are limiting aspects of a modeling approach like this as it could be suspected that its validity is constrained to the case that it is solved for. For example, the calculated parameters for the case of some amount of administered antibodies may not accurately describe the case with a very different amount. This is because physiological processes could include non-linear elements, for example in the case of saturable binding.

Macroscopic compartments are a rather coarse description of an actual tissues behavior because of the tissues inherent heterogeneity in structure as well as function. With this in mind, the model parameters is not expected to describe an actual physical process, they are rather averaged quantities calculated to make the model results fit to the measured data.

Model structure

The basic model structure is shown in figure 4. As mentioned above, the compartment model is designed with a central compartment containing the plasma. This compartment, in turn, is connected to all other compartments. *k*(i,j) represents the rate constant from compartment *j* to compartment *i*.

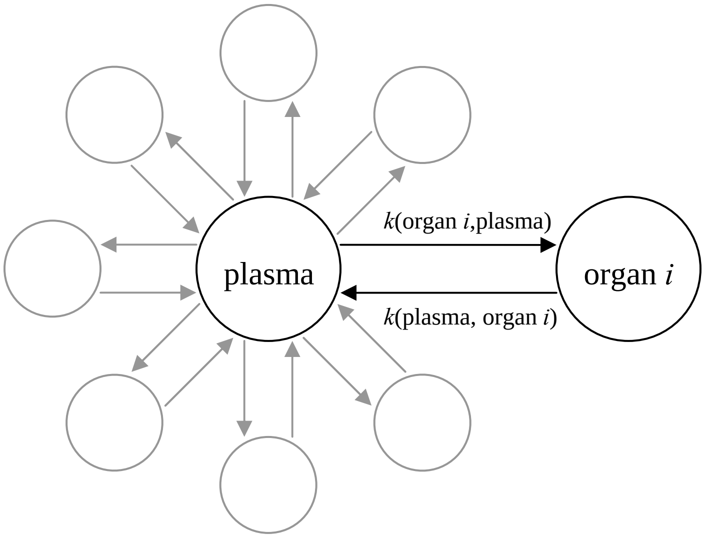

Figure 4: Schematics of the compartmental model. A central plasma compartment is connected to a set of compartments representing various tissues and organs. Each connection is described by the following rate constant *k*(*i*,*j*).

Mathematically, the compartment model is described the following system of ordinary differential equations

$$\frac{dA_p}{dt} = \sum_i \left(k(p,i)A_i - k(i,p)A_p \right)$$
$$\frac{dA_i}{dt} = k(i,p)A_p - k(p,i)A_i \qquad \textbf{(eq. 4)}$$

where A is the activity (expressed here as percentage of administered activity) of the compartment and index (p) and (i) denotes plasma and organ i respectively.

Data

Data from eight patients which were treated with radioimmunotherapy for B-cell lymphoma were available. There is no intention to discuss or evaluate the clinical trial in this thesis, so the study design is only briefly commented. The treatment consists of two parts. In the first part, monoclonal antibodies labeled with ^{111}In are administered for diagnostic/planning purposes. ^{111}In is a radioactive isotope with a half-life of 67.3 hours and is suitable for diagnostic imaging because of the emission of gamma-rays with suitable energy. The activity distribution is then monitored by repeatedly scintillation camera measurements and blood samples. About a week after the first injection, ^{111}In-labeled antibodies and antibodies labeled with ^{90}Y are administered. ^{90}Y is a high-energy beta emitting radionuclide with a half-life of 64.0 hours, suitable for therapy. After a certain time, remaining antibodies in the circulation are removed by extracorporeal adsorption. During this therapeutic phase, the activity distribution is monitored as in the diagnostic phase.

The activity distribution measurements are then used for quantifying the activity contained in different regions of interest (ROI). The regions of interest are outlined in the scintillation camera picture by identifying anatomical and physiological structures. For the different patients, different sets of ROI were quantified. In all patients, activity was quantified for the liver, spleen, kidneys and lungs. For most of the patients, the heart was also quantified. Tumor ROI:s were quantified for patients 3, 4, 5, 7 and 8. Plasma activity concentration at different time points was measured with a well counter and the total plasma activity was calculated by estimating the total plasma volume in the patient. Details about the measurement can be seen in table 1.

Patient #	Diagnostic phase			Therapeutic phase			
	Adm. activity (^{111}In) [MBq]	# time points (ROI)	# time points (plasma)	Adm. activity (^{111}In) [MBq]	# time points (ROI)	# time points (plasma)	ECAT onset time [h p.i.]
1	156	3	9	258	7	18	44.6
2	151	3	9	250	7	17	44.6
3	151	3	9	255	7	17	45.0
4	153	3	9	241	7	18	44.5
5	153	-	9	257	7	18	43.6
6	150	-	8	261	7	17	43.3
7	153	6	10	266	7	19	69.3
8	156	6	9	255	7	16	68.2

Table 1: Details of the measurements. From the data, it is obvious that there are two subsets regarding the number of collected measurements in the diagnostic study and the onset time for ECAT. For patients 1 to 6, the ECAT onset time is about 44 h p.i., while it is about 70 h p.i. for the last two patients. For the diagnostic study, the number of measurements is 3 and 6 respectively. For patients 5 and 6, no organ activity measurements were available from the diagnostic study.

Time-activity curves for different organ/tissues, for the diagnostic and therapeutic phase, can be sees in the appendix, figures A:1-2 respectively.

The use of decay-corrected data in compartmental modeling

The use of decay-corrected data in pharmacokinetic modeling is limited to the models consisting of linear, homogenous differential equations only, as described by a general theorem found by Williams et al [Williams et al 1995]. Although the model described here meets those criterions, uncorrected data is used and physical decay is explicitly entered into the model equations.

Another reason for using uncorrected data is the statistical errors in the measurements. When correcting the data for physical decay, the measured value is multiplied with the value of a function $\exp(\lambda t)$ for the time t of the measurement. As a consequence, the error in the measurement is multiplied as well. Since a constant standard deviation is used in the fitting process, uncorrected data is preferable.

Separating plasma activity from residual tissue activity

Since the time-activity measurements of a ROI performed using a scintillation camera represent a sum of different-behaving kinetics, it would be advantageous if one can separate different behaving regions from others. This is, however, rather difficult since such a separation procedure would introduce new unknown parameters to the model resulting in a higher degree of freedom.

One separation could however be done, namely to separate the plasma content from the compartment of interest. This could be done by making two assumptions: (1) that all activity in the compartment is found in the plasma at very early times after administration and (2) that the plasma kinetics in the ROI follows the global plasma kinetics. The first (1) assumption can be verified by examining the plasma-activity curves. From these, it is obvious that about 94 % of the administered activity is located in the plasma at about one hour after administration. After two hours, about 90 % of the activity is still in the plasma. The drop in plasma activity in earlier times after administration is rapid, suggesting the need for an as early measurement as possible for determining the plasma contents in a ROI. The last assumption (2) could be questioned since the kinetics of the plasma contained in an organ probably is more complicated, again because of the organs heterogenic properties. There should, however, be at least some major part of the plasma contents that rapidly equilibrates with the global plasma compartment because of the apparent quick rise of activity following administration.

By making these assumptions, each compartment is implicitly modeled as a sum of two different parts with separate kinetic behaviors: one part that immediately follows the global plasma kinetics and one part that represents a slower uptake, corresponding to extravasation, interstitial transport by convection and/or diffusion, and binding to antigen sites.

One new parameter is introduced, α_i, which is the fraction of the total plasma volume that is contained in the ROI. The value of the parameter introduced can easily be determined if there exist a very early activity measurement because of the first assumption above. In terms of mathematics, the time-activity curve for each organ can then be described as (see also figure 5)

$$A(t)_i = A(t)_{i,residual} + \alpha_i \cdot A(t)_{plasma} \qquad \textbf{(eq. 5)}$$

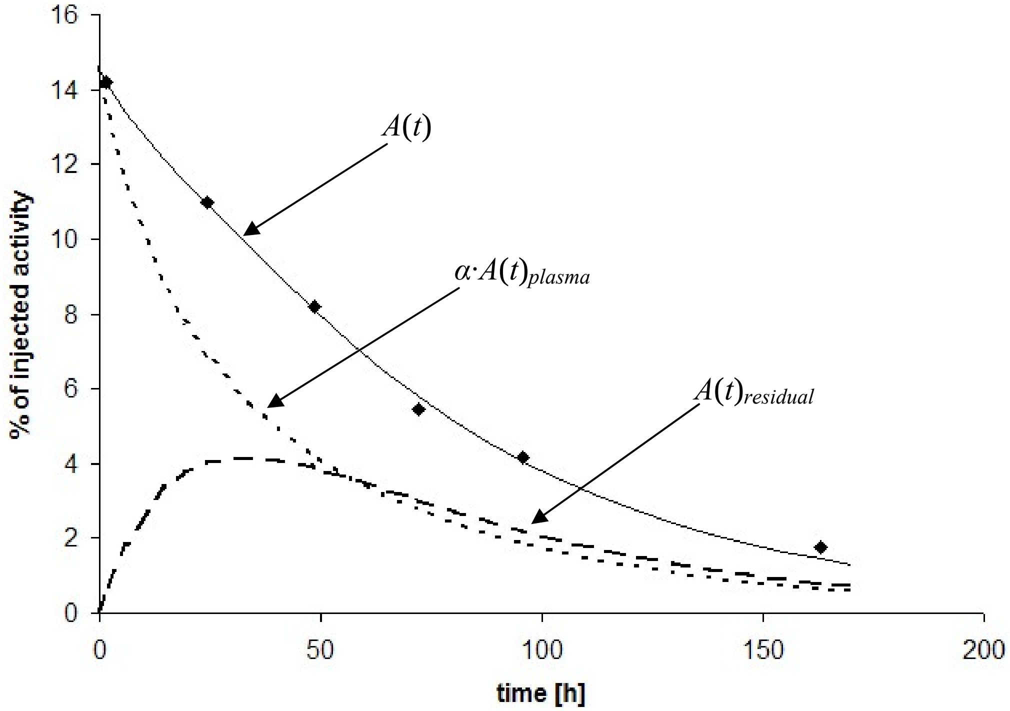

Figure 5: Example of how the kinetics for a ROI is modeled as a sum of two parts. The solid line is the model fit to the data points. The line is a sum of the dotted line, which is the plasma kinetic curve scaled by the factor *α* (the fraction of the plasma volume contained in the ROI), and the dashed line, which represents the uptake.

At a very early time after administration, the activity in the ROI would be (using the above assumption)

$$A(t)_i\big|_{t\approx 0} = \alpha_i \cdot A(t)_{plasma}\big|_{t\approx 0}$$

With early measurements of the activity in both plasma and the ROI, α_i then can be calculated as

$$\alpha_i = \left.\frac{A(t)_i}{A(t)_{plasma}}\right|_{t\approx 0}$$

With accurate activity quantification, where the activity measured in the ROI correlates with the actual activity in the organ which the ROI is set to represent, this fraction would correlate with the fraction of the total plasma volume contained in the organ. Fractions like this have previously been tabulated [Leggett et al].

Setting up the model

For the setup, solving and the fit to data of the model, the computer program SAAM II (Saam Institute, University of Washington) is used. SAAM II is a software for kinetic analysis, which includes an application for compartmental modeling.
Using the SAAM II software, the first step of setting up the model is to simply draw the different compartments and their junctions. Outflows from each compartment are created to handle the physical decay. A ‘remainder’ compartment is created to account for the remaining activity which is not located in the quantified regions.

From the ‘remainder’ compartment, an additional outflow is created for balancing the system and compensate for excretion. The reason for using an outflow from the ‘remainder’ compartment only is, again, to keep the model simple. A more sophisticated excretion model would need additional parameters and require more data (for example urine and/or feces). One example of the model is shown in figure 6.

The next step is to define an input function. Here the input function is modeled as a bolus injection into the plasma compartment. The amount of the administered activity is set to the non-dimensional value of 100, making all compartments describing the percentage of administered activity. The measured data is imported as a text file and associated with the different compartments according to eq. 5.

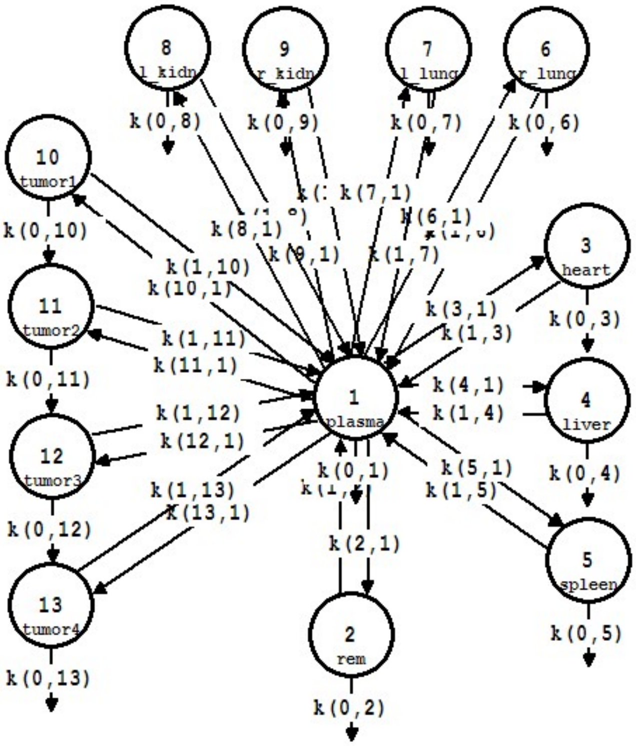
8
l_kidn
9
r_kidn
7
l_lung
6
r_lung
k(0,8)
k(0,9)
k(0,7)
k(0,6)
10
tumor1
k(0,10)
k(7,1)
k(8,1)
k(6,1)
k(9,1)
k(1,7)
k(1,10)
k(10,1)
3
heart
11
tumor2
k(3,1)
k(1,3)
k(0,3)
k(1,11)
k(11,1)
k(0,11)
k(4,1)
k(1,4)
4
liver
1
plasma
k(1,12)
k(12,1)
12
tumor3
k(0,1)
k(5,1)
k(1,5)
k(0,4)
k(1,13)
k(13,1)
k(0,12)
k(2,1)
5
spleen
13
tumor4
2
rem
k(0,5)
k(0,13)
k(0,2)

Figure 6: An example of the compartmental model as viewed in SAAM II. The number of modeled compartment differs between the patients as the number of quantified regions is different.

Solving the system and fit to data

The system of ordinary differential equation is solved using the SAAM II software. Before solving the system, the parameters of the model has to be given start values. These values are also used as the initial "guess" used by the fitting process. Since the fitting process may be sensitive to poor choices for the values for the initial starting values, the starting values are chosen to be in the same order of magnitude of previously published values [Norrgren et al]. The solution is also visually checked for non-physical looking results like strange behaving time-activity curves. The parameters to fit consists of a set of *k(p,i)*, *k(i,p)* and α_i for the *i* compartments, which makes three parameters per modeled compartment.

The fitting to data is done by minimizing the expression

$$w_{i,j} \cdot \left(\mathrm{datum}_{\mathrm{i,j}} - \mathrm{model}_{\mathrm{i,j}}\right)^2$$

which is minimizing the squared difference between the data value and the corresponding model value. $w_{i,j}$ is a weight factor (for the i$^{\text{th}}$ datum in the j$^{\text{th}}$ data set) which is dependent of the error associated with each data point. In general, the weight assigned to each datum is the inverse of its variance

$$w_{i,j} = \frac{1}{Var_{i,j}} = \frac{1}{\bar{v}_j \cdot \sigma_{i,j}^2}$$

where $\sigma_{i,j}^2$ is the standard deviation and $\bar{v}_j$ is a possible unknown constant for the j$^{\text{th}}$ data set. In SAAM II, there are several possibilities regarding the data weights. One possibility is to use fractional standard deviation (FSD), which assigns a constant coefficient of variation as the variance to each datum. In that case, the standard deviation is calculated as

$$\sigma_{i,j} = A \cdot \left|\mathrm{data}_{\mathrm{i,j}}\right|$$

where *A* is the value for the fractional standard deviation. One other possibility is to us a constant standard deviation (SD) and hence variation to each datum. In this case (with *A* as the constant standard deviation)

$$\sigma_{i,j} = A$$

In the case of FSD, the error is a constant percentage of a datum. This means that data with small values contribute more because the weight associated with a small datum is large. For example, in the case of an assumed fractional standard deviation of 5 % (A = 0.05) and absolute weighting ($\bar{v}_j$ equals unity):

$$100 \pm 5 \Rightarrow w = \frac{1}{\sigma^2} = \frac{1}{25} = 0.04$$

$$1.0 \pm 0.05 \Rightarrow w = \frac{1}{\sigma^2} = \frac{1}{0.0025} = 400$$

In the case of a constant standard deviation, the error is constant over all data and the weights of the data are the same. For example, a constant standard deviation of 0.5 (A = 0.5),

$$100 \pm 0.5 \Rightarrow w = \frac{1}{\sigma^2} = \frac{1}{0.25} = 4$$

$$1.0 \pm 0.5 \Rightarrow w = \frac{1}{\sigma^2} = \frac{1}{0.25} = 4$$

In this case, data with large values will contribute more since the term $\left(\mathrm{datum}_{\mathrm{i,j}} - \mathrm{model}_{\mathrm{i,j}}\right)^2$ is normally larger for larger data [SAAM tutorial].

In the presented model used in this work, a constant standard deviation is used. This seems reasonable since data with larger values should contribute more.

SAAM II has a feature to calculate the time-integrals of the model curve. This feature was used to calculate cumulated activities.

Modeling ECAT as an perturbation

Extracorporeal immunoadsorbtion can easily be modeled as a perturbation of the compartment model. This is done using the “Change condition” feature available in the SAAM II software, wherein parameters can be altered during the time of experiment. A new transfer rate coefficient is defined, k(0, plasma), to describe the an additional outflow from the plasma compartment (see figure 7). This parameter is set to equal zero at all times except during the ECAT procedure, where its value is found by the fitting process.

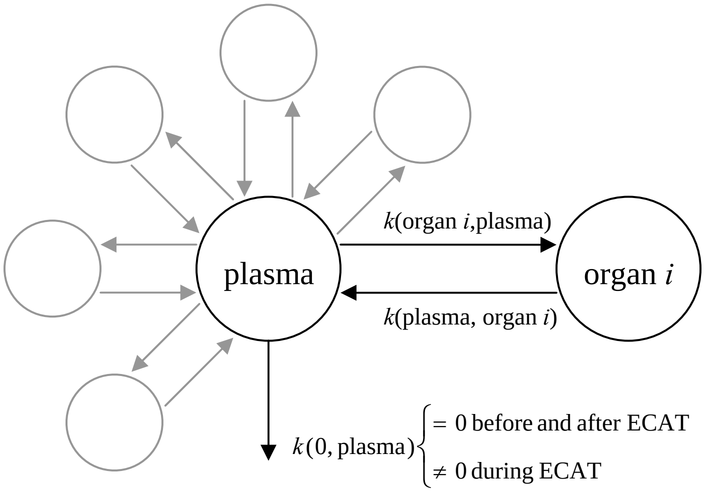
plasma
organ i
k(organ i,plasma)
k(plasma, organ i)
$k(0,\text{plasma})\begin{cases}=0\text{ before and after ECAT}\\ \neq 0\text{ during ECAT}\end{cases}$

Figure 7: Schematics for the ECAT outflow in the compartmental model. The additional outflow from the plasma compartment, with corresponding rate constant *k*(0, plasma), is active only during the ECAT procedure.

Results

A successful model fit was obtained for all patients in the therapeutic study, one example is shown in figures 8-10.

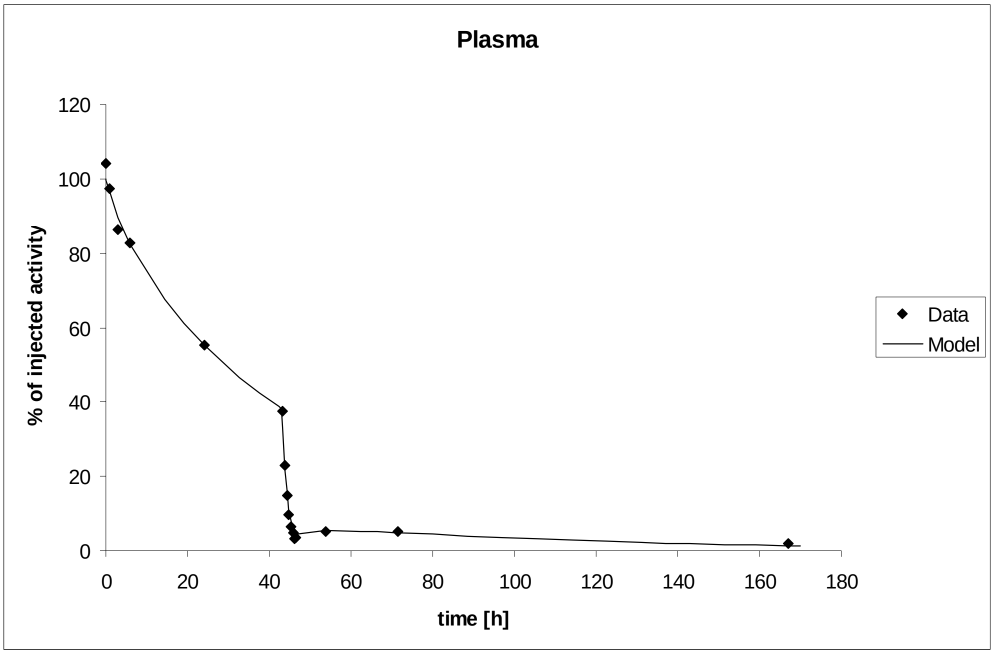

Figure 8: The model (straight line) fit to data for the plasma compartment (in this example for the therapeutic study of patient no. 6). It can be noticed that the ECAT procedure is well described by the model.

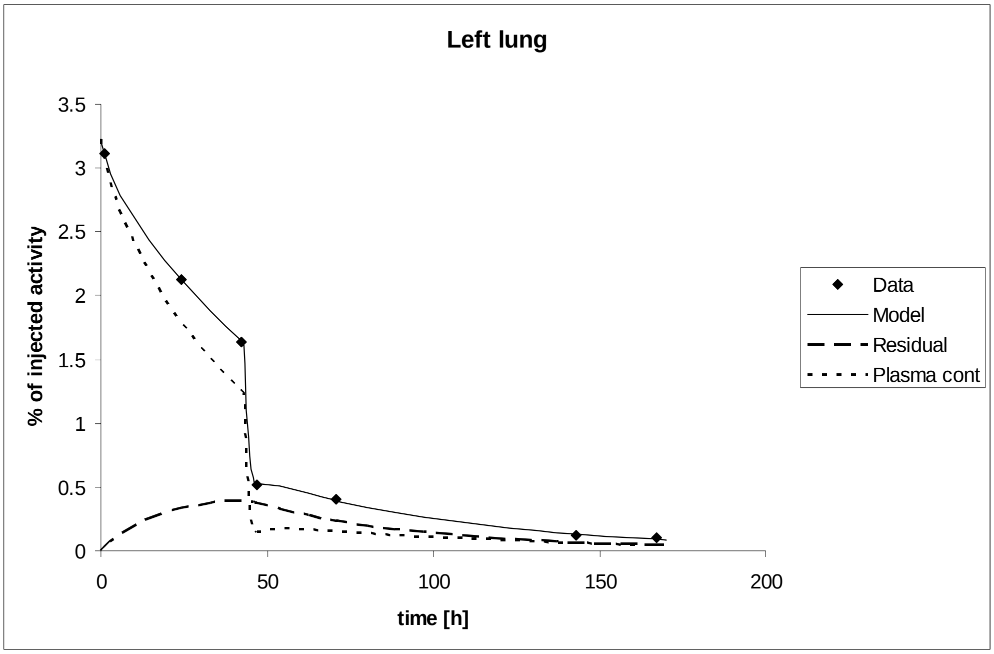

Figure 9: The model fit (straight line) fit to data for the left lung (patient no. 6). The dotted line represents the plasma contents in the organ and the dashed line represents residual activity, which corresponds to an uptake.

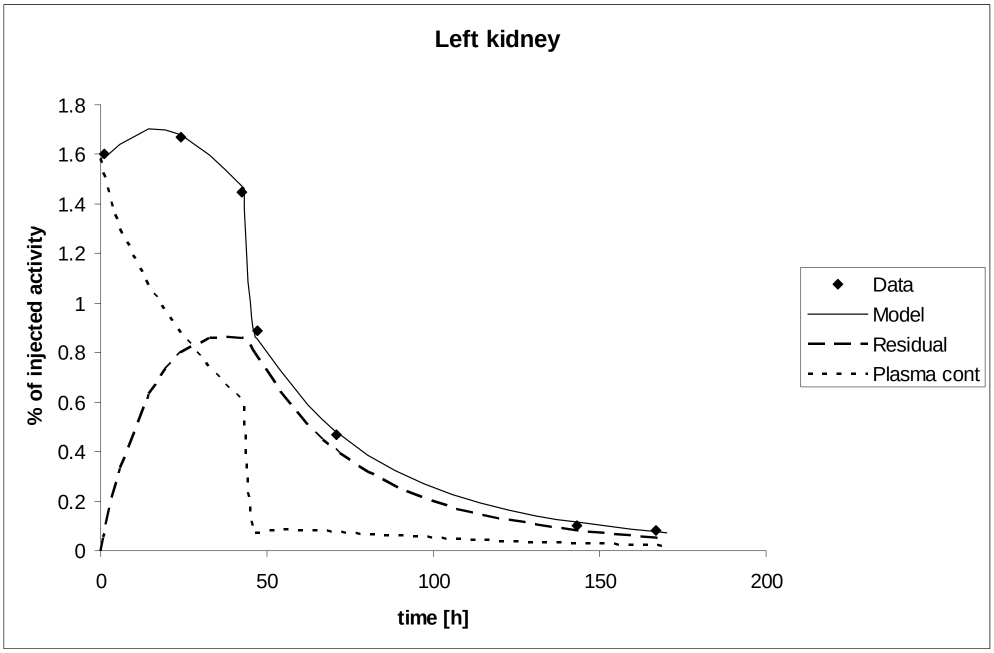

Figure 10: The same plot as previous figure, but now for the left kidney. A completely different shape of the uptake curve can be noticed compared with the one in figure 9, which is a consequence of different pharmacokinetics in this organ.

For the diagnostic study, no fit could be made for the patients with only 3 measurement time points (patients 1 to 4) as expected. As the first measurement for these patients was made at about 48 hours after administration, the fraction of the plasma contained in the organ/tissue (α) was not possible to determine with any reasonable accuracy.

Plots of the data and the model fit for the therapeutic study, and for the diagnostic study for patients 7 and 8, can be seen in the appendix, figures A:3-10. For patient no. 7, the curves have also been corrected for physical decay and can be seen in figure A:11-12.

The fraction of total plasma contained in the organs (α) is compared to tabulated values [Leggett et al] in figure 11.

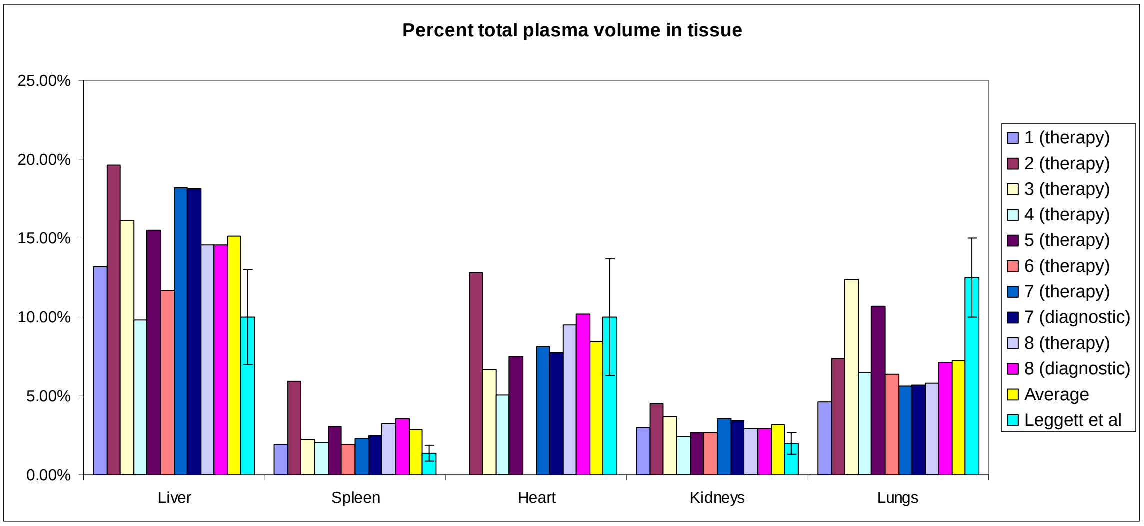

Figure 11: Values for the percentage of the total plasma volume contained in different organs. The two rightmost bars in each group represents the average value (with one standard deviation) and the values published by Leggett et al.

There are quite big differences (sometimes more than a factor two) in percentage of total plasma contained in tissues for the different patients. The kidneys show to have the most uniform values with an average of 3.2 % of total plasma (ranging from 2.4% to 4.5%) compared to 2 % from Leggett et al. The most non-uniform values are for the lungs, with average of 7.2% (range 4.7% to 12.4%) compared to 12.5 % from Leggett et al. No activity quantification was made for the heart in patients 1 and 6.

The ECAT outflow rate, *k*(0, plasma), as found by the fitting process, is shown in figure 12.

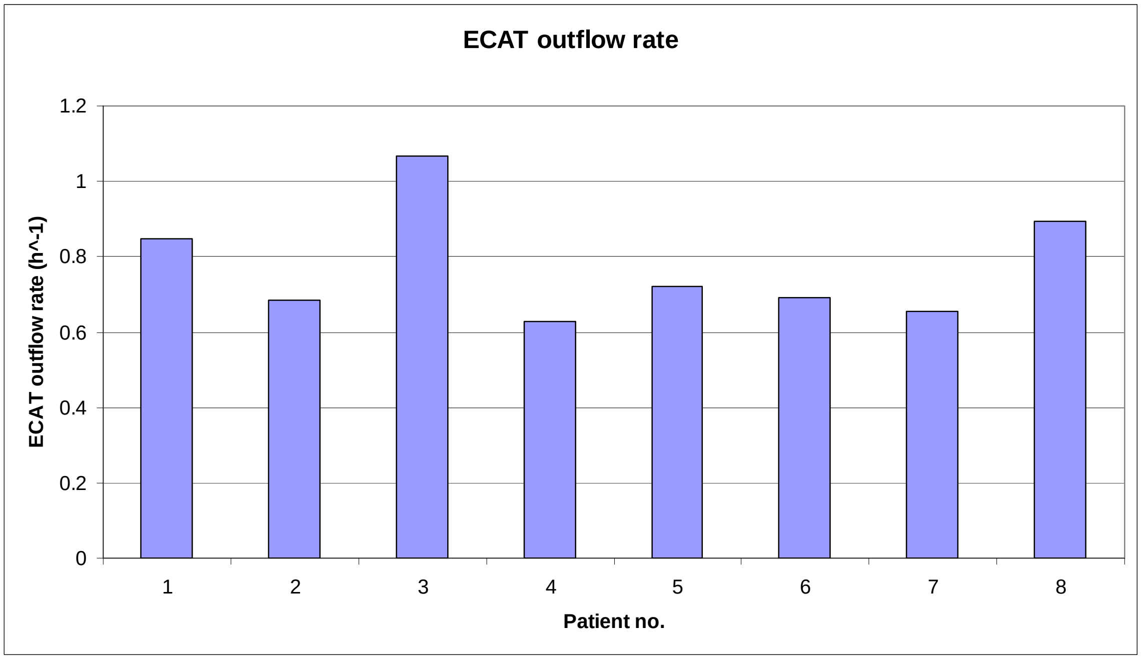

Figure 12: The ECAT outflow rate as calculated during the model fitting process to the therapeutic data. The average value is 0.77 h^{-1}.

One important point of this work was to investigate whether the data from the diagnostic examination could be used for predicting the pharmacokinetics of the therapy by introducing ECAT as a perturbation to the model. This was only possible to do with two of the patients (patients 7 and 8) because of the need of sufficient data in the diagnostic study. The ECAT outflow parameter from the therapeutic model was added to the diagnostic model. The diagnostic model was then re-solved, and the result was compared to the measured data for the therapeutic phase. An example can be seen in figures 13a-13d (plasma and liver for patient no. 7). The complete results can be seen in figures A:13-14 in the appendix. Here, the data points is the measurements from the therapy study while the model curve is based on the diagnostic study with an ECAT outflow added as in the therapy model.

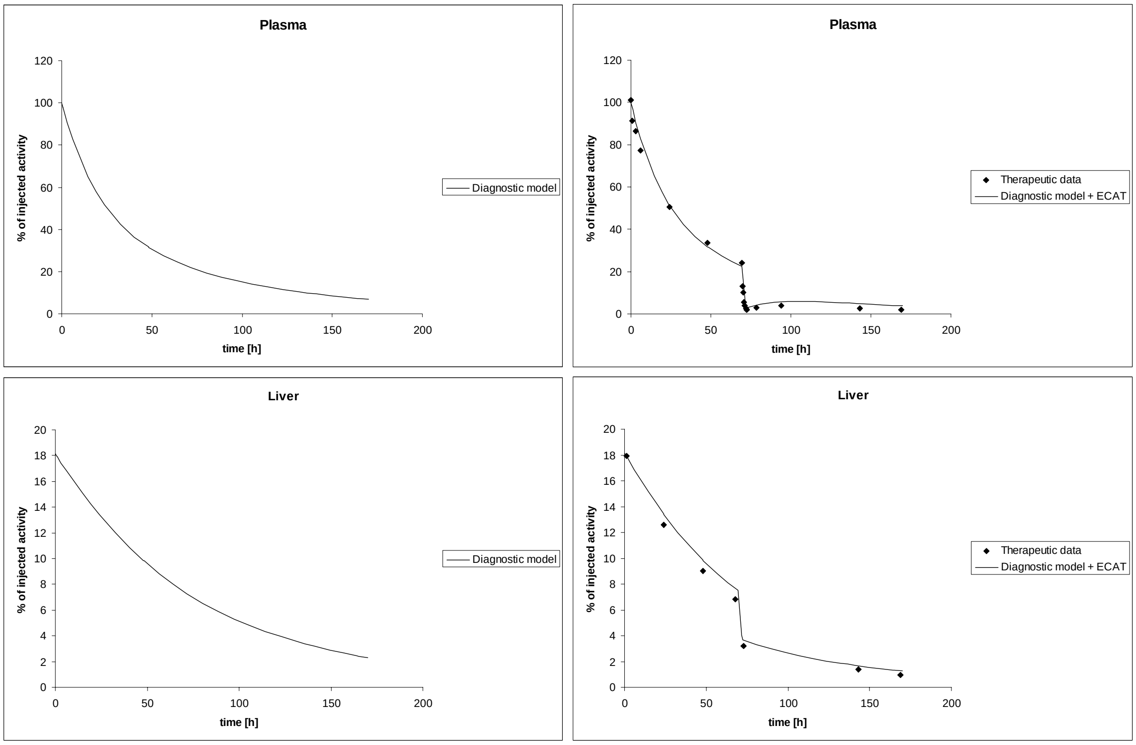

Figure 13a-d: Model prediction compared to therapeutic data for patient no. 7 (plasma and liver). The figures to the left shows the model solutions based on the data from the diagnostic study of the patient. The therapeutic ECAT parameter was added to the model and the model was resolved. The result is compared to the data from the therapeutic study in the figures to the right.

Discussion

An empirical model has been developed to describe the pharmacokinetics in radioimmunotherapy for a set of patients. The model is simple in that it consists of first order linear differential equations and requires no previous knowledge of physiological parameters such as regional blood flows, lymph flows, extravasation rates, and volumes or compositions of different organs/tissues. Despite the simplicity of the model, the fit to data is very good.

One basic assumption for the model is that the plasma contents in each region can be separated out by using the information of the plasma measurements. This makes it possible to study the actual uptake of the organ/tissue.

Regarding the percentage of the total plasma that is contained in the different organs (figure 11), there are substantial differences between the patients but a general trend is clear with the liver containing the largest part of the plasma, followed in order by the heart, lungs, kidneys and spleen. There are several possible sources of errors that will influence these estimations, for example in the outlining of the ROI and activity quantification. Besides, these patients may have tumor involvement in some of the organs.

Several observations can be made from the plots (figures A:3-10 in the appendix):

- The ECAT procedure is well described by an additional outflow from the plasma compartment that is only active for a limited time, which can be seen by noticing the good fit to plasma data in the time of the ECAT treatment (se for example figure 8 above).

- There are distinguishable similarities for the different organs in the patients. For example, the total cumulated activity in heart and lungs is usually dominated by the plasma activity in these organs (about 70-80% of the total cumulated activity), while the kidney activity merely is dominated by the uptake (plasma activity is about 40-50% of total cumulated activity). The liver and spleen represents intermediate cases with plasma activities of about 45-55% and 50-60% of the total cumulated activity respectively. For the modeled tumor ROI:s, plasma activity corresponds to about 40-50% of the total cumulated activity, but there are values ranging from as low as 30% to as high as 70%.

- Certain individual differences are obvious from the plots. Some of them may be artifacts as result of errors in the measurements, quantification and ROI outlining. Some may be due to that the plasma fit is not sufficiently good because the shape of the plasma kinetic curve is crucial in this analysis. Others may have physiological explanations. For example, the kinetics of the right lung in patient 3 shows an unexpected behavior and is completely different from what is usually the case. This observation has a physiological explanation; there are major malignant sites in this patient’s right lung.

The model predictions for the therapy (figures A:13-14), using the diagnostic data, are quite good. The best predictions are made for the compartments containing higher activity, as plasma, liver and heart. The model prediction is little worse for spleen, kidneys and lungs. For the compartments containing less than one percent of the injected activity, which is often the case for the tumors, there is a bigger difference between the model predictions and the data. The probable cause for this is that the statistical uncertainties increase as the measured and quantified activity contents are decreasing.

There are many sources of error influencing the activity quantification and consequently the data used here. For example, the outlining of ROI in the planar scintillation images is in many cases difficult, especially for the tumor regions. For reliable measurements, the ROI:s must be identical for every imaging session. This requires accurate patient positioning or that the positioning can be corrected for. In planar imaging, there is always a problem with the overlapping of organs. This is partly corrected for, but complete separation of organs and tissues would require 3D-imaging.

Throughout the modeling, the data used was not corrected for physical decay and physical decay of the radionuclides was explicitly entered in the model as additional outflows from every compartment. The reason for this was, as mentioned in the method description, to avoid scaling of the errors. By explicitly enter the physical decay, it is easy to modify the physical decay rate to adjust for different radionuclides. This could be convenient, for example, if the radionuclide used for diagnosis has a different half-life than the radionuclide used for therapy.

Part B: Microscopic model

Method

The microscopic model presented here is based on previous works by Sgouros [Sgouros 1992], and Weinstein and colleagues [Fujimori 1990, van Osdol 1991]. The model describes the transport of monoclonal antibodies in a small, prevascual spheroid of tumor cells. The cluster contains an assumed uniform distribution of immobile antigens, represented by the antigen concentration $s(r,t)$. Antibodies outside the cluster, represented by the concentration $c_p(t)$, is transported by diffusion into the cluster and binds to available antigen sited to form antibody-antigen complexes, represented by the concentration $\overline{cs}(r,t)$. Free, mobile antibodies within the cluster is represented by the concentration $c(r,t)$. The basic ideas and properties for the transport of antibodies are found in the background section of this work.

Geometry

The geometry of the model (figure 14) is simple: a sphere with radius R. By choosing different time-antibody concentration curves for the cluster border, simulation can be made for different cases. For example, using the plasma concentration curve as border concentration would correspond to a simulation where the cluster is positioned completely surrounded by plasma.

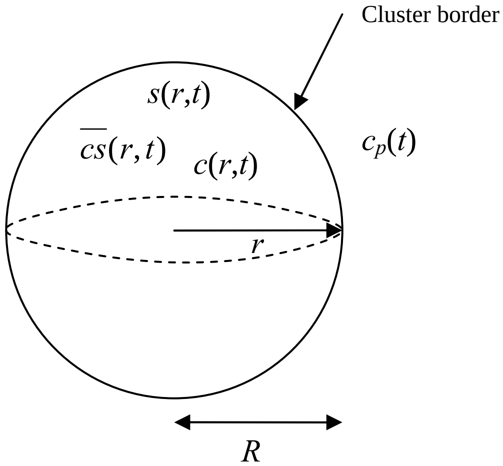

Figure 14: The geometry of the microscopic model.

For simplicity, radial symmetry is assumed in the model. This can be justified if the structure and composition is assumed homogenous and gives much shortened calculation times as the model is reduced to one space dimension. The diffusion equation in spherical coordinates and with radial symmetry can be written as

$$\frac{\partial c}{\partial t} = \nabla \bullet (D \nabla c) = D \nabla^2 c = D\left(\frac{\partial c^2}{\partial^2 r} + \frac{2}{r}\frac{\partial c}{\partial r}\right) \qquad \textbf{(eq. 6)}$$

by using that the diffusion coefficient, D, is invariant in space and by recognizing that the radial part of the laplacian is

$$\nabla^2 = \frac{1}{r^2}\frac{\partial}{\partial r}\left(r^2 \frac{\partial}{\partial r}\right)$$

Equation system

The resulting system of equations describing the spatial and temporal distribution of the three species is (based on equation 3)

$$\begin{aligned}
\frac{\partial c(r,t)}{\partial t} &= D\left(\frac{\partial c(r,t)^2}{\partial^2 r} + \frac{2}{r}\frac{\partial c(r,t)}{\partial r}\right) - k_f c(r,t) s(r,t) + k_r \overline{cs}(r,t) \\
\frac{\partial s(r,t)}{\partial t} &= n\left(-k_f c(r,t) s(r,t) + k_r \overline{cs}(r,t)\right) \qquad \textbf{(eq. 7)} \\
\frac{\partial \overline{cs}(r,t)}{\partial t} &= k_f c(r,t) s(r,t) - k_r \overline{cs}(r,t)
\end{aligned}$$

Solving conditions

The solution of the equation system requires boundary conditions for all boundaries and initial conditions for all dependent variables. Since no spatial movement is possible for the antigens and antibody-antigen complexes, the fluxes are specified to equal zero at all borders. For the antibodies, two different approaches are possible.

The first option is to specify the concentration on the border directly (which corresponds to a Dirichlet boundary condition in the theory of partial differential equations [Mathworld web page]). This would be the case when the cluster is positioned directly in for example plasma, where the administered antibodies are directly accessible to the cell cluster [Sgouros 1992]. This case would also apply to incubated tumor spheroids *in vitro*.

$$c(R,t) = c_p(t)$$

The second option is to specify the border flux rather than the border concentration (which corresponds to a Neumann boundary condition). This form of boundary condition is suitable when modeling a cluster with a system of supplying microvessels attached [Fujimori et al 1990].

$$-D\frac{\partial c_l(r,t)}{\partial r} = P(c_p - c_l)$$

Here, c_l refers to the concentration within the cluster adjacent to the surface. The initial condition is zero concentration for all species but the antigen concentration which is equal to s_0. This also equal the total concentration by the expression (the mass balance)

$$s_0 = s + n\overline{cs}$$

Solution strategy

The model was solved using Femlab (Comsol AB) which is a commercial modeling package for the simulation of physical processes that can be described by partial differential equations. Femlab uses the finite element method for solving the partial differential equation systems. The finite element method is a computational method that subdivides an object into very small but finite-size elements. The physics of one element is approximately described by a finite number of degrees of freedom (DOFs). Each element is assigned a set of characteristic equations (describing physical properties, boundary conditions, and imposed forces), which are then solved as a set of simultaneous equations to predict the object's behavior [Femlab reference guide].

When the geometry and the equation system, along with the boundary and initial conditions are defined, the geometry is subdivided into a structure of finite-sized elements, which is called the mesh. Choosing smaller sized elements makes a finer mesh. The accuracy of the solution is dependent of the size of the elements, but a finer mesh will also make the solving process more computer-intensive and it will take longer time to solve the problem. In this case however, the model geometry is very simple so a very fine mesh can be chosen yet having reasonably short computing times.

Modeling extracorporeal immunoadsorbtion

The effect of ECAT in the microscopic level can easily be modeled; simply by using an ECAT plasma concentration curve as border concentration. However, an analytical expression for such curve is not available which calls for using a numerical representation. This can easily be done in the Femlab package using the built-in "Interpolation functions" feature which includes different forms of interpolation methods for using numerical data as input.

Modeling pretarget protocols

Pretarget protocol, as discussed above, can also be implemented in the microscopic model. This is done by introducing several new species. For example, a protocol which includes administration of biotinylated monoclonal antibodies followed by radiolabeled streptavidin requires six dependent variables in the model (compared to the former three): free biotinylated antibodies, free antigen sites, antibody-antigen complex, free radiolabeled streptavidin, streptavidin-antibody complex and streptavidin-antibody-antigen complex. Modeling the streptavidin plasma concentration as a bolus injection followed by exponential decay might cause a convergence problem for the time-dependent solver because of the sharp gradients. This can however be solved by "smearing" out the gradient using a smoothing function, making the time-derivatives continuous. Modeling pretarget protocols is beyond the scope of this work and will not be analyzed in detail.

Results

Verification of the modeling and solving procedure

As a baseline simulation no antigen-turnover is considered and the valency is set to unity. Also, the Dirichlet boundary condition is used. The values for the different parameters in the model (table 2) are taken from a previous publication by Sgouros [Sgouros 1992]. The plasma clearance parameters are obtained by solving the ordinary differential equation system describing the compartment model in Sgouros's work. The choice of model parameters makes it possible to evaluate the results by comparing to the calculations by the same work.

Parameter	**Value**
Initial antigen concentration, s_0 (nM)	1500
Association rate, k_f (nM^{-1} h^{-1})	1.3
Dissociation rate, k_r (h^{-1})	0.3
Diffusion constant, D (µm^2 h^{-1})	2268
Cluster radius, R (µm)	100
Binding valency, n	1

Table 2: Values for the parameters used for verification of the model setup and solving procedure.

The result of the calculations with these values for the parameters is shown in figures 15a and 15b. The solutions are in excellent agreement, both qualitatively and quantitatively, with the calculations made by Sgouros, which were made by the same choice of parameters but a different solving method (Schmidt forward finite difference scheme implemented in a FORTRAN program). This verifies the model setup and solving procedure.

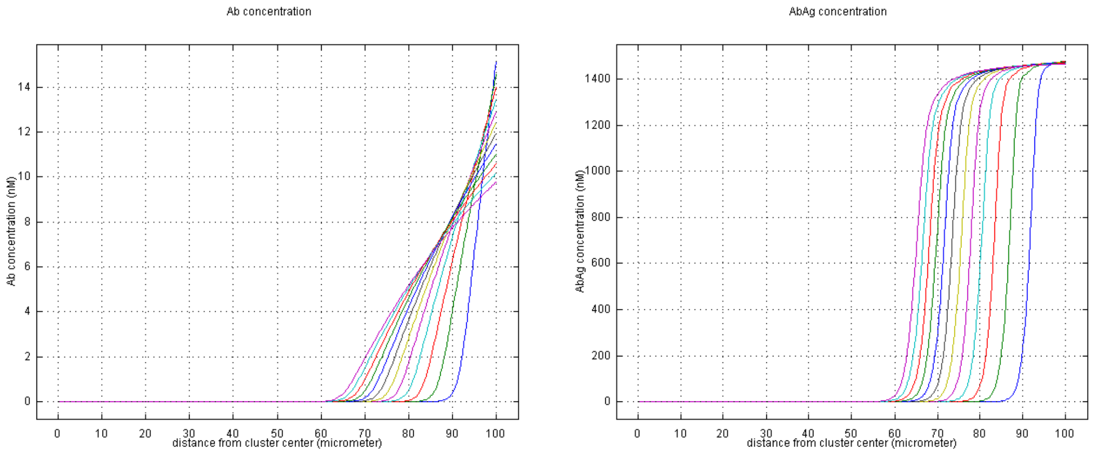

Figure 15a (left) and 15b (right): Solution of the microscopic model with the same choice of parameters as is used in a previous publication by Sgouros. Figure 15a shows the concentration profiles of free antibodies at different times after administration. The rightmost curve is the concentration profile at 2 hours after administration, which is followed by the solutions at every two hours up to 24 hours (the leftmost curve). Figure 15b shows the corresponding concentration profiles for the antibody-antigen complexes.

Baseline simulation

Next step is to use plasma kinetics from the clinical trial as border concentration and make simulations for a “real” case. In this work, the primary interest is to study micrometastases that are located in the circulating plasma. Therefore, only the first boundary condition (Dirichlet) will be applied in this analysis.

As a baseline simulation, the previous values for the parameters will be used and no antigen turnover is assumed. The parameters (see table 3) for plasma kinetics is calculated by doing a least square fit to the plasma measurement (corrected for physical decay) for one of the patients in the radioimmunotherapy study ($c_{p,0}$ is calculated by assuming that the antibody has a mass of 150 kD, the injected amount is about 5 mg and that the plasma volume is about 3500 ml).

Plasma concentration curves is modeled as an bi-exponential equation

$$c_p(t) = c_{p,0}\left(\alpha \exp(-\lambda_1 t) + (1-\alpha)\exp(-\lambda_2 t)\right)$$

where $c_{p,0}$ is the initial concentration, λ_1 and λ_2 are the rate constants for the different phases of the plasma clearance.

Plasma parameter	Value
α	0.7188
λ_1 (h^{-1})	0.0057
λ_2 (h^{-1})	0.1410
$c_{p,0}$ (nM)	10.0

Table 3: The parameters used for the plasma concentration curve outside the tumor cell cluster.

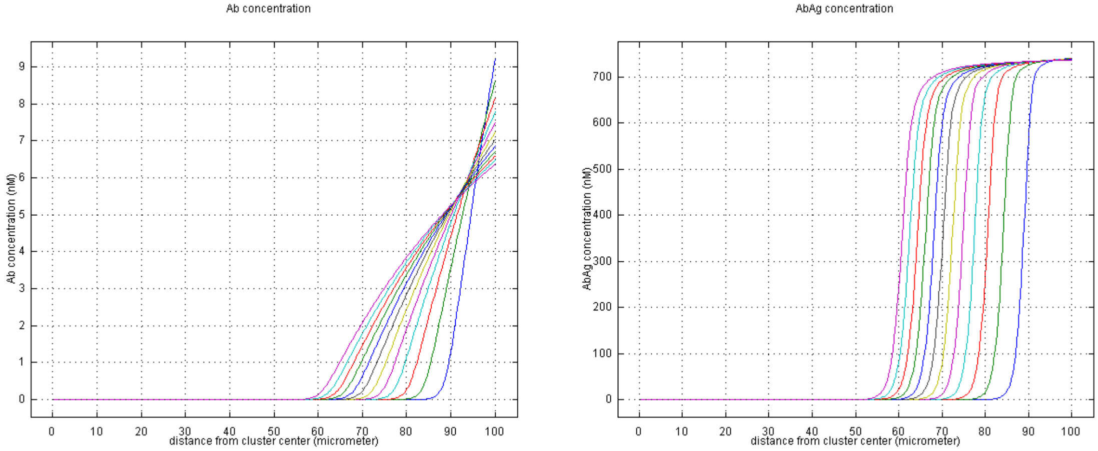

Figure 16a (left) and 16b (right): Solutions for the baseline simulation of the microscopic model. Figure 16a shows the concentration profile of free antibodies at different times after administration. The rightmost curve is the concentration profile at 2 hours after administration, which is followed by the solutions at every two hours up to 24 hours (the leftmost curve). Figure 16b shows the corresponding concentration profiles for the antibody-antigen complexes.

The results of the baseline simulation can be seen in figures 16a-b. When plotted in the same way as before (figure 15a-b), the solution with these parameters looks much similar to the previous solution. A slightly faster transport can be noticed. This is the combined affect of change in the plasma concentration and the change in valence from 1 to 2 (notice also that the maximum concentration of antibody-antigen complex has dropped a factor 2 because of change in valence).

The shape of the antibody-antigen concentration is characteristic, and the phenomenon responsible for it is referred to as the “binding-site barrier” in the literature. The binding-site barrier is the consequence of that the antibody-antigen reaction is associated with a time-scale much shorter than the diffusive transport. As free antibodies diffuse inward the cluster, they almost immediately bind to available antigens because of the high affinity of the reaction. The result is that the antibodies will be retarded in its transport by the fact of its successful binding to antigen on the tumor cell surface [Fujimori et al 1990].

For a longer time perspective, with the same parameters used as in the baseline simulation above, the time that is required to saturate the cluster is revealed (figures 17a and 17b). In this case, the time for completely saturate the cluster is about 95 hours.

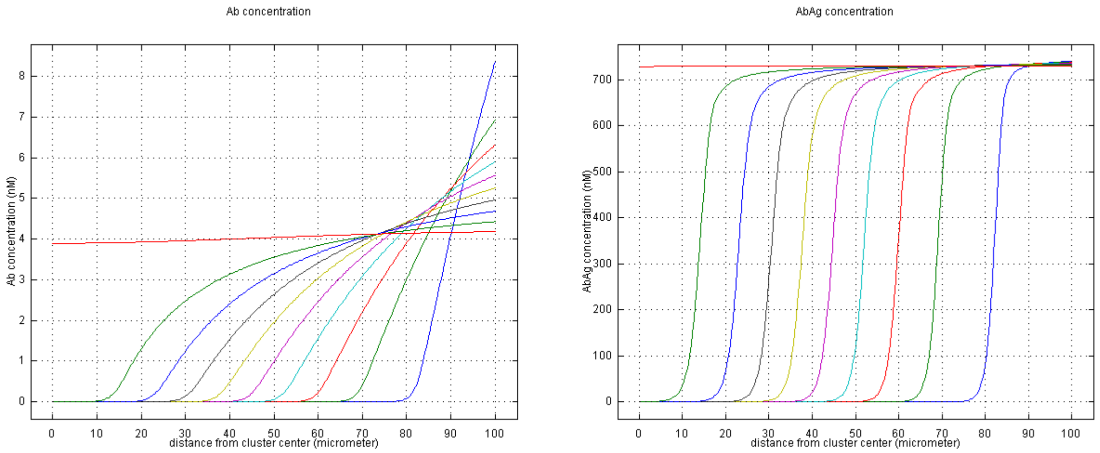

Figure 17a (left) and 17b (right): Solutions for the baseline simulation of the microscopic model. Figure 17a shows the concentration profile of free antibodies at different times after administration, where the rightmost curve is the concentration profile at 5 hours after administration, followed by the solutions for every tenth hours up to 95 hours. Figure 17b shows the corresponding concentration profiles for the antibody-antigen complexes. It can be noticed that the time to completely saturate the cluster is about 95 hours.

The saturation progress can also be visualized by plotting the degree of saturation, $S(\%)$, which is the ratio of occupied antigen sites to the total number of antigen sites (see figure 18). It is calculated as (in one space dimension):

$$S(\%) = \frac{100 \cdot n \cdot \int_{0}^{R} \overline{cs}(r,t)dr}{s_0 \cdot R} \qquad \textbf{(eq. 8)}$$

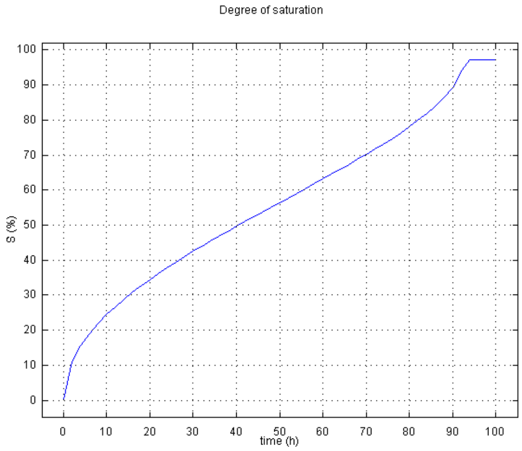

Figure 18: The degree of saturation in the tumor cell cluster as a function of time. The saturation curve is characterized by an initial steep rise followed by an almost-linear part and then a steep rise right before the apparent total saturation. As can be noticed, 100 % saturation does never occur. The reason for this is that there is a constant release and rebinding of antibodies (since it is a finite affinity), leaving a small portion of the antigens free at all times.

In the case of no degradation of antigens and/or antibody-antigen complexes, the release of antibody is a slow process because of the high binding affinity. This can be seen in figures 19a and 19b (notice the time-scale).

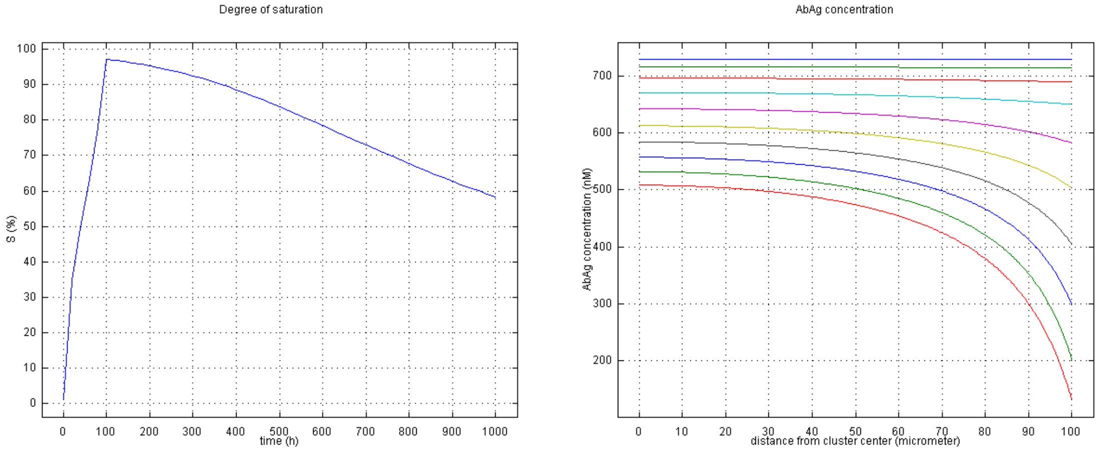

Figure 19a (left) and 19b (right): The release of antibody in the absence of degradation of antigens and/or antibody-antigen complexes. Figure 19a shows the percentage saturation curve as function of time (notice the time-scale). Figure 19b shows the concentration profile of antibody-antigen complexes in the tumor cluster at different times after administration. The upper curve is the solution at 100 hours, followed by solutions every 100 h up to 1000 h.

Modeling ECAT

The next step is now to study the effects of extracorporeal immunoadsorbtion on the microscopic cluster. The plasma concentration function, $c_p(t)$, is then replaced with a numerical representation of the plasma concentration curve from the same patient as in the baseline simulation above, but here from the therapeutic phase. For making the results easy to compare, the initial plasma concentration is set to the same value as above (10 nM). To verify the plasma concentration function, the border concentration of the cluster is plotted in figure 20.

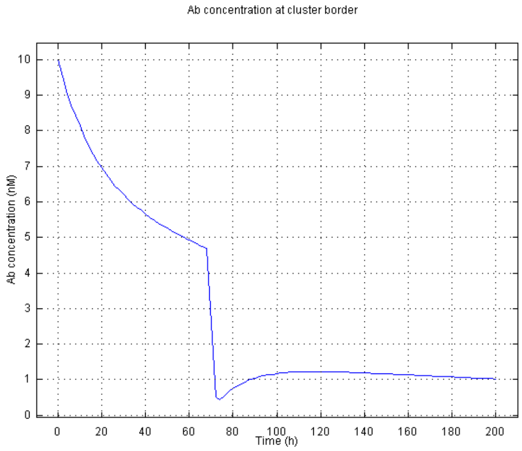

Figure 20: The cluster border concentration in the simulation with ECAT. The ECAT onset time is about 70 h after administration.

The concentration of antibody-antigen complexes is shown in figure 21a. Here, the rightmost curve is the solution for t = 20 h and the following curves for every 20 hours up to t = 140 h. The saturation function is shown in figure 21b.

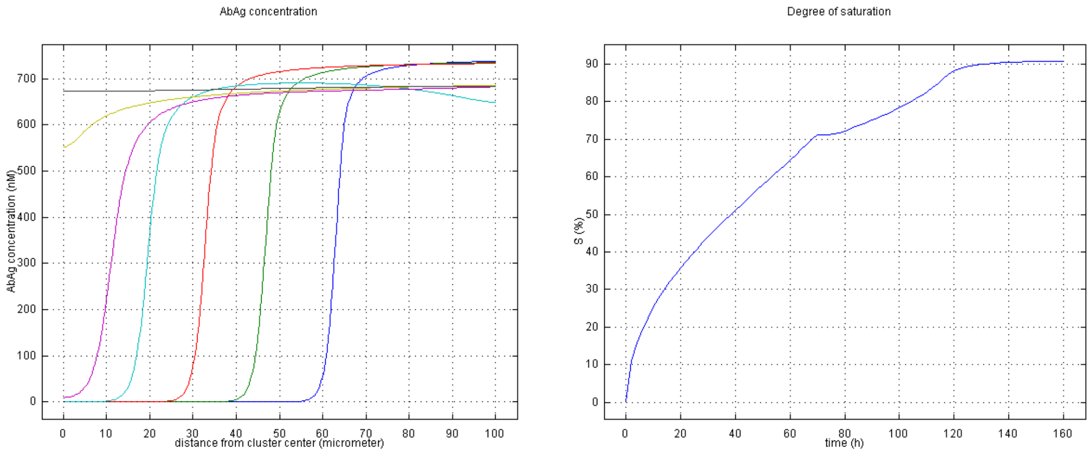

Figure 21a (left) and figure 21b (right): Simulation of the microscopic model with ECAT. Figure 21a shows the antibody-antigen complex concentration distribution and Figure 21b shows the percentage saturation as a function of time. The antibody-antigen complex concentration drops from about 730 nM to 680 nM on the periphery of the cluster as a result of ECAT and the inward transport speed is somewhat slowed. In the saturation plot, a "crack" can be seen at the time of ECAT. The saturation process is stopped for a short time and then resumed with a reduced speed as the border concentration rises. The limit degree of saturation is slightly above 90 % (compared to ca 97 % in the previous case) and the 90 % saturation occurs at about 140 hours (compared to 90 hours previously).

Dependence of model parameters

The next step was to examine how the saturation of the tumor cell cluster depends on the different parameters in the model. It might also be important as the values for the parameters differ quite a lot in the literature [Banerjee et al 2001, Graff et al 2003]. The saturation was examined using a parameter called t_{90}, which is the time it takes to saturate the antigen sites in the cluster to 90 %.

For simplicity a constant antibody concentration outside the cluster is initially assumed ($c_p = c_{p,0}$ in the model). This is not the regular case in the clinical practice, but might be possible to accomplish with a steady i. v. infusion. Constant concentration would, however, normally be the case for incubated tumors *in vitro*. The parameters examined were the cluster radius (R), the initial antigen concentration (s_0), the (constant) antibody concentration outside the cluster (c_p), the diffusion constant (D) and the antibody-antigen affinity (K_a).

The degree of saturation (S) was calculated for a wide range of values for the parameters by varying one parameter at the time and keeping the others fixed. Table 4 shows the initial values used and the range of simulated values for the parameters.

Parameter	Initial value	Range of values	Number of values
Ab conc. in plasma $c_{p,0}$	11 nM	11 – 1100 nM	7
Initial free Ag conc., s_0	1500 nM	100 – 10000 nM	7
Cluster radius, R	100 µm	25 – 250 µm	6
Diffusion constant, D	2268 $\mu m^2\ h^{-1}$	100 – 10000 $\mu m^2\ h^{-1}$	6
Binding affinity, K_a	4.33 nM^{-1}	0.833 – 43.3 nM^{-1}	15

Table 4: Details of the parameters used for investigating different parameters influence on the saturation.

By plotting and curve-fitting it was found that there exist simple relationships between the saturation time and all the parameters of the models, except the affinity (figures 22a-e).

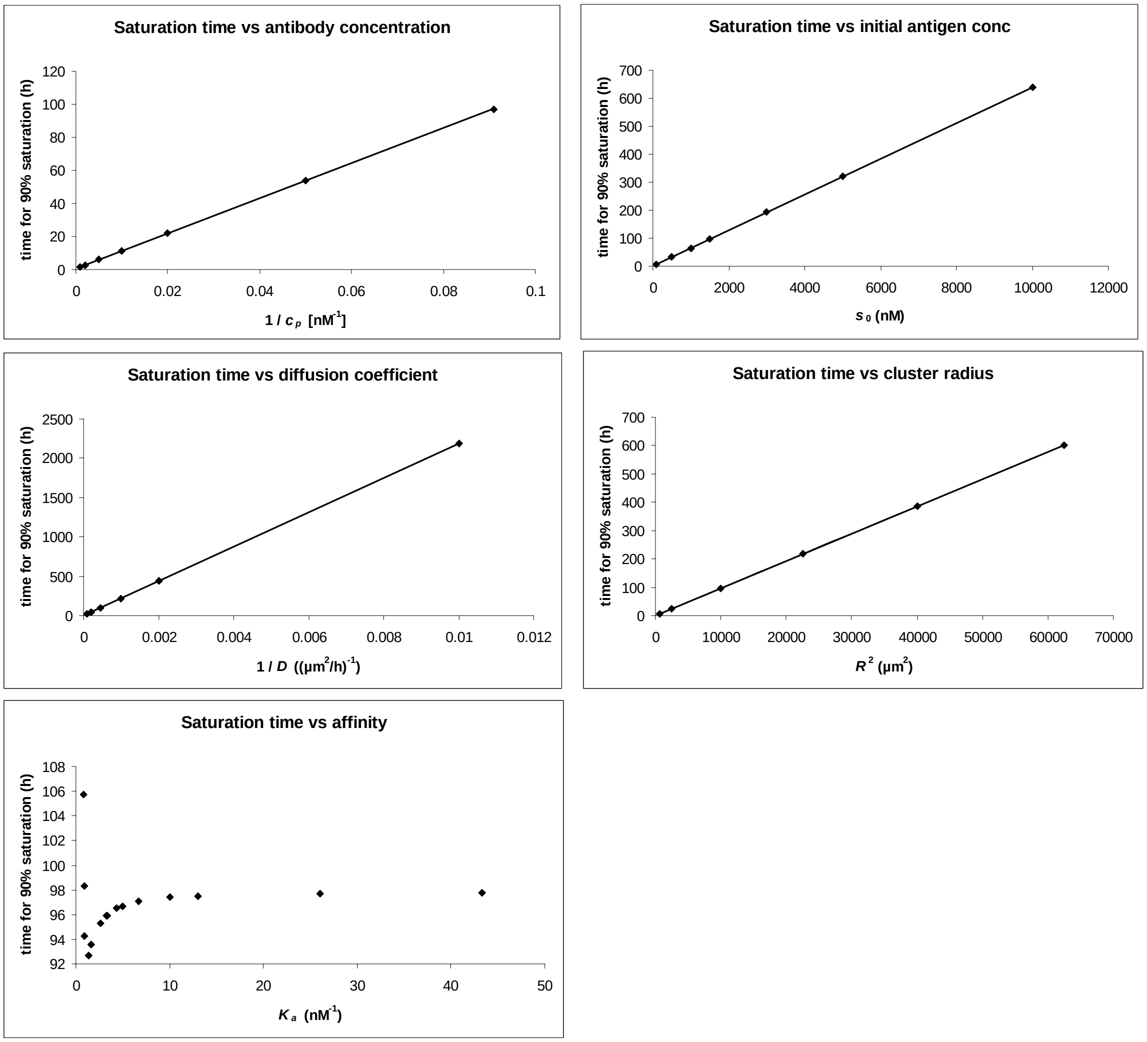

Figure 22a-e: Time for 90 % saturation (t_{90}) as function of different parameters of the model. As can be seen, t_{90} is inversely proportional to the (constant) antibody concentration outside the cluster (fig 22a) and to the diffusion coefficient (fig 22c). t_{90} is directly proportional to the initial free antigen concentration (fig 22b) and proportional to the square of the cluster radius (fig 22d). The relationship of t_{90} to the antibody-antigen affinity (fig 22e) is somewhat more complex for an affinity below 10 nM^{-1}, but t_{90} is independent of the affinity for higher values.

The relationship between the 90 % saturation time and the affinity is somewhat more complex. From the plot it is obvious that the saturation time rises towards infinity when the affinity approaches zero. Naturally, zero affinity antibodies will never be able to saturate the antigen sites. The saturation time has one local minimum where the affinity is approximately 1 nM^{-1}. When increasing the affinity further, the saturation time increases up to an affinity of about 10 nM^{-1} where the saturation time approaches a constant value. With the “binding site barrier”-phenomena in mind this seems understandable. When the affinity is low, the antibodies can diffuse relatively freely throughout the cluster volume, resulting in a faster saturation. With increasing affinity, the transport process gets hindered to a higher degree by the interaction process. As the affinity has reached a certain level, further increase doesn’t affect the saturation time because the reaction rate is already much faster than the diffusive transport. According to this result, there is no need for increasing the affinity further regarding the uptake phase. Increased affinity might, however, play a more important role for the retention phase (which is not studied in detail here).

Thus, assuming affinities of 10 nM^{-1} or more, the saturation time can approximately be described as

$$t_{90} \approx C \cdot \frac{s_0 \cdot R^2}{c_{p,0} \cdot D} \qquad \textbf{(eq. 9)}$$

with C being the constant of proportionality. A more careful examination of this expression shows that it holds for an initial free antigen concentration at least ten times the antibody concentration in the plasma, but it is rather insensitive for changes in cluster radius and diffusion rate coefficient. The constant of proportionality is examined for a wide range of values of the parameters (figure 23).

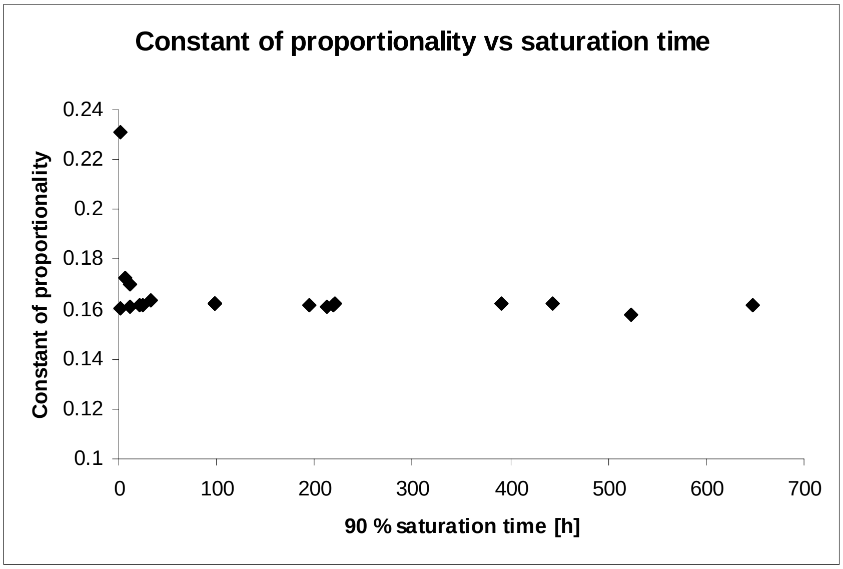

Figure 23: Calculated constant of proportionality for different saturation times (for affinities above 10 nM^{-1} and a binding valence of 2). For 90 % saturation times of 20 hours or more, the value is about 0.162. For t_{90} less than 20 hours, the relationship is not very accurate.

Although a constant antibody concentration outside the cluster may be possible to achieve in practice, a bolus injection of antibodies normally is the case. For example, the plasma kinetics of antibodies following a bolus injection can often be described by a bi-exponential equation, like

$$c_p(t) = c_{p,0}\left(\alpha \exp(-\lambda_1 t) + (1-\alpha)\exp(-\lambda_2 t)\right)$$

It would therefore be valuable with a general expression of the saturation time applicable to other modes of antibody concentration outside the cluster. The saturation of the cluster is dependent on having a high enough antibody concentration outside the cluster for a time long enough. For constant concentration ($c_p(t) = c_{p,0}$) outside the cluster, the area under the concentration curve can be written

$$\int_0^{t_{90}} c_p(t)dt = c_{p,0} \cdot t_{90} \approx c_{p,0} \cdot C \cdot \frac{s_0 \cdot R^2}{c_{p,0} \cdot D} = C\frac{s_0 \cdot R^2}{D}$$

by using eq. 9 (assuming that $s_0 \geq 10 \cdot c_p(t)$ at every time). For an arbitrary concentration curve, $c_p(t)$, the general expression then would be

$$\int_0^{t_{90}} c_p(t)dt \approx C\frac{s_0 \cdot R^2}{D} \qquad \textbf{(eq. 10)}$$

Solving this equation for the appropriate antibody concentration curve outside the cluster gives the saturation time. As example, a mono exponential concentration curve,

$$c_p(t) = c_{p,0}\exp(-\lambda t)$$

where λ is the clearance rate of the antibody concentration outside the cluster, gives the solution

$$\int_0^{t_{90}} c_{p,0}\exp(-\lambda t)dt = c_{p,0}\frac{1}{\lambda}\left(1-\exp(-\lambda t_{90})\right) \approx C\frac{s_0 \cdot R^2}{D} \Leftrightarrow$$

$$\Leftrightarrow t_{90} \approx -\frac{1}{\lambda}\ln\left(1 - C\frac{s_0 \cdot R^2 \cdot \lambda}{c_{p,0} \cdot D}\right)$$

The equation is only defined for

$$C\frac{s_0 R^2 \lambda}{c_{p,0} D} < 1$$

or

$$T_{1/2} > C \frac{s_0 R^2 \ln 2}{c_{p,0} D}$$

where $T_{1/2}$ is the biological half-life of the antibody concentration in plasma. The expression indicates that there is a limit for the biological half-life, below which saturation is impossible. The expression for the saturation time, in the case of a mono exponential decay of concentration outside the cluster, as a function of the biological half-life of the antibody concentration in the plasma was checked by calculations (figure 24). The same parameters as in the baseline simulation are used, except that the concentration in plasma now is modeled as a mono exponential decay.

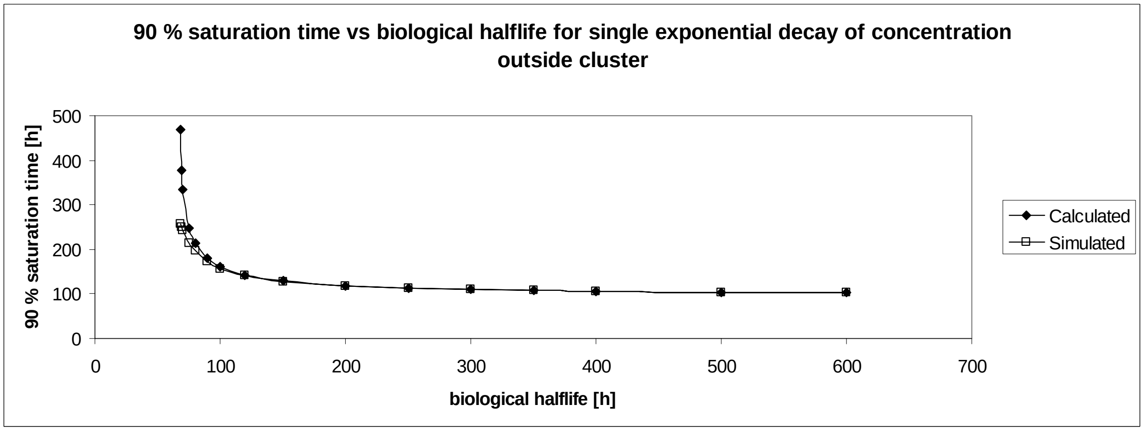

Figure 24: 90 % saturation time as function of the biological half-life for a single exponential clearance of antibodies outside the cluster, calculated and simulated. The simplified formula describes the saturation time with good accuracy for the region where the biological half-life is not very close to the limiting half-life. In this case, the limit half-life for saturation is 67.43 hours. For a half-life of 68 hours, the calculated saturation is about 80% above the simulated value. The difference then decreases rapidly; at a half-life of 80 hours the calculated value is about 9% above the simulated. Although the big difference in calculated and simulated saturation time at half-lives close to the limit, the calculated limit itself is predicted with great accuracy.

In the case of the bi-exponential function, which often is used for describing the plasma kinetics, it is not trivial to calculate the value for t_{90}. In general, however, the requirements on the time-activity curve describing the plasma kinetics for at least 90 % saturation in the tumor cluster is (still that assuming $s_0 \geq 10 \cdot c_p(t)$ at all times), according to equation 10, that

$$\int_0^t c_p(t)dt \geq C \frac{s_0 \cdot R^2}{D} \qquad \textbf{(eq. 11)}$$

So far only the case of the time for 90 % saturation has been investigated, but the general expression holds for other saturation degrees as well if the value for the constant of proportionality is modified. The value for different saturation degrees has been calculated and can be seen in table 5.

Percentage saturation	**Constant of proportionality, *C***
95 %	0.165
90 %	0.162
85 %	0.157
80 %	0.150
75 %	0.141

Table 5: Calculated values for the constant of proportionality, *C*, for different percentage of saturation (for affinities above 10 nM^{-1} and a binding valence of 2). By modifying the value for *C*, t_{80} and t_{75} (etc.) can be evaluated using eq. 9.

Discussion

A model for investigating the pharmacokinetics of monoclonal antibodies for microscopic tumor nodules has been developed. The basic ideas for the model have been adapted from previous works by Sgouros and Weinstein et al. The purpose for the model in the described form is to study the pharmacokinetics for microscopic metastases in the circulating plasma. Radioimmunotherapy is often optimized, by choices of treatment strategy, for treatment of the macroscopic tumors that can be visualized by various imaging techniques, for example by scintillation camera. In the case where microscopic tumor nodules are suspected, the treatment strategy should be optimized to treat these as well. The model presented here might be useful for evaluate such treatment strategies.

As the basic model equations presented may be difficult to assess and requires specific computer programs to be solved, an approximate, simplified expression is derived for studying the saturation as function of the model parameters. It was found that the time it takes to saturate the cluster could be related to the parameters by an easy expression under certain conditions. This could be useful as the values of the different parameters in the model may vary a lot in the clinical cases. The relationship of the saturation time to the parameters of the model found in this work corresponds to an expression previous publication by Graff et al [Graff et al].

There are a few limitations of the model. First it must be remembered that the model described here is limited to the case of microscopic clusters because of the simplifying assumptions stated above. Also, antigen turnover has been neglected in the analysis so far. This could easily be introduced in the model by specifying turn-over rates. Internalization of antigen is not dealt with here as well, but could be incorporated in the model by introducing one new species to the equation system, together with internalization rates. So far, the model is assuming tumor cell clusters completely surrounded by plasma (by the use of the Dirichlet boundary condition), but the model could be used to study tumor nodules with blood supply at the nodule surface by capillaries, using a different (Neumann) boundary condition.

General conclusions

Macroscopic model

The overall good fit to the therapy data indicates that the model in fact, despite its simplicity, is suitable for describing the pharmacokinetics of monoclonal antibodies in radioimmunotherapy, and that it might become useful as a tool for evaluation of clinical strategies. By fitting the model to data from a diagnostic study, the treatment data could be predicted by introducing ECAT as a perturbation to the model. Combined with dosimetry, this feature could be used for treatment planning for radionuclide therapy.

In terms of optimization, there are several different parameters of the model which can be evaluated. For example, the onset time and duration of the ECAT procedure can be evaluated and possibly optimized by investigating different strategies in the model. Also, strategies that include two or more ECAT procedures at different time points could be assessed.

The choice of radionuclide for therapy could also be evaluated by finding an optimal choice for physical half-life in the model. This could, in turn, be complemented by dosimetric calculations.

Microscopic model

The main purpose of the microscopic model is to evaluate the pharmacokinetics in suspected micrometastases. As an overall treatment strategy should be optimized for the treatment of micrometastases as well as macroscopic tumors, a microscopic model like this is useful. The optimization in this case includes modeling of different types of monoclonal antibodies and fragments, which have different transport properties as affinities and diffusion rates. Although the model is applicable only to microscopic lesions at this point, qualitative conclusions from the simulations may be drawn that has consequences in the macroscopic scale also.

By combining the pharmacokinetics with the use of point-dose kernels, the dosimetry of micrometastases can be assessed and different choices regarding radionuclides can be evaluated.

Acknowledgement

First of all, I would like to thank my supervisor Sven-Erik Strand for introducing me to the exciting field of radioimmunotherapy and for excellent guidance. I would also like to thank Katarina Sjögreen, Michael Ljungberg and Karin Wingårdh who provided me with the quantitative patient data, Kristin Bingen for professional help with Femlab, and prof Larry Williams for fruitful discussion on compartmental modeling. A special thanks also to Cecilia Hindorf, for all support during this work. And most of all, I wish to thank my beloved Annette Öderwall for all encouragement.

References

1. **Banerjee, R. K., et al. "Finite element model of antibody penetration in a prevascular tumor nodule embedded in normal tissue." J.Control Release 74.1-3 (2001): 193-202.**

2. **Boerman, O. C., et al. "Pretargeted radioimmunotherapy of cancer: progress step by step." J.Nucl.Med. 44.3 (2003): 400-11.**

3. **Chinol, M., et al. "Pretargeted Radioimmunotherapy of Cancer." In: Abrams, P. G. and Fritzberg, A. R., (eds.) Radioimmunotherapy of Cancer, Marcel Dekker Inc., New York, 2000, pp. 169-193.**

4. **Cremonesi, M., et al. "Three-step radioimmunotherapy with yttrium-90 biotin: dosimetry and pharmacokinetics in cancer patients." Eur.J.Nucl.Med. 26.2 (1999): 110-20.**

5. **Dvorak, H.F., et al. "Tumor architecture and Targeted Delivery." In: Abrams, P. G. and Fritzberg, A. R., (eds.) Radioimmunotherapy of Cancer, Marcel Dekker Inc., New York, 2000, pp. 107-135.**

6. **Flessner, M. F. and R. L. Dedrick. "Tissue-level transport mechanisms of intraperitoneally-administered monoclonal antibodies." J.Control Release 53.1-3 (1998): 69-75.**

7. **Fujimori, K., et al. "A modeling analysis of monoclonal antibody percolation through tumors: a binding-site barrier." J.Nucl.Med. 31.7 (1990): 1191-98.**

8. **Fujimori, K., D. R. Fisher, and J. N. Weinstein. "Integrated microscopic-macroscopic pharmacology of monoclonal antibody radioconjugates: the radiation dose distribution." Cancer Res. 51.18 (1991): 4821-27.**

9. **Garkavij, M., et al. "Extracorporeal immunoadsorption from whole blood based on the avidin-biotin concept. Evaluation of a new method." Acta Oncol. 35.3 (1996): 309-12.**

10. **Garkavij, M., et al. "Enhanced radioimmunotargeting of 125I-labeled L6-biotin monoclonal antibody (MAb) by combining preload of cold L6 MAb and subsequent immunoadsorption in rats." Cancer Res. 55.23 Suppl (1995): 5874s-80s.**

11. **Garkavij, M., et al. "Improving radioimmunotargeting of tumors: the impact of preloading unlabeled L6 monoclonal antibody on the biodistribution of 125I-L6 in rats." J.Nucl.Biol.Med. 38.4 (1994): 594-600.**

12. **Garkavij, M., et al. "Extracorporeal whole-blood immunoadsorption enhances radioimmunotargeting of iodine-125-labeled BR96-biotin monoclonal antibody." J.Nucl.Med. 38.6 (1997): 895-901.**

13. **Graff, C. P. and K. D. Wittrup. "Theoretical analysis of antibody targeting of tumor spheroids: importance of dosage for penetration, and affinity for retention." Cancer Res. 63.6 (2003): 1288-96.**

14. **Grana, C., et al. "Pretargeted adjuvant radioimmunotherapy with yttrium-90-biotin in malignant glioma patients: a pilot study." Br.J.Cancer 86.2 (2002): 207-12.**

15. **Green, A. J., et al. "Mathematical model of antibody targeting: important parameters defined using clinical data." Phys.Med.Biol. 46.6 (2001): 1679-93.**

16. **Hartmann, C., et al. "A pharmacokinetic model describing the removal of circulating radiolabeled antibody by extracorporeal immunoadsorption." J.Pharmacokinet.Biopharm. 19.4 (1991): 385-403.**

17. **Jain, R. K. "Transport of molecules, particles, and cells in solid tumors." Annu.Rev.Biomed.Eng 1 (1999): 241-63.**

18. **Jang, S. H., et al. "Drug delivery and transport to solid tumors." Pharm.Res. 20.9 (2003): 1337-50.**

19. **Koizumi, K., et al. "Multicompartmental analysis of the kinetics of radioiodinated monoclonal antibody in patients with cancer." J.Nucl.Med. 27.8 (1986): 1243-54.**

20. **Leggett, R. W. and L. R. Williams. "Suggested reference values for regional blood volumes in humans." Health Phys. 60.2 (1991): 139-54.**

21. **---. "A proposed blood circulation model for Reference Man." Health Phys. 69.2 (1995): 187-201.**

22. **Levitt, D. G. "The pharmacokinetics of the interstitial space in humans." BMC.Clin.Pharmacol. 3.1 (2003): 3.**

23. **Linden, O., et al. "Single tumor cell uptake and dosimetry of technetium-99m Fab' or minute anti-CD22 in low-grade B-cell lymphoma." Cancer 94.4 Suppl (2002): 1270-74.**

24. **Linden, O., et al. "Radioimmunotherapy using 131I-labeled anti-CD22 monoclonal antibody (LL2) in patients with previously treated B-cell lymphomas." Clin.Cancer Res. 5.10 Suppl (1999): 3287s-91s.**

25. **Linden, O., et al. "131I-labelled anti-CD22 MAb (LL2) in patients with B-cell lymphomas failing chemotherapy. Treatment outcome, haematological toxicity and bone marrow absorbed dose estimates." Acta Oncol. 41.3 (2002): 297-303.**

26. **Loevinger, R., et al. "MIRD Primer for Absorbed Dose Calculations (revised edition)." The Society of Nuclear Medicine, New York, 1991.**

27. **Norrgren, K., S. E. Strand, and C. Ingvar. "Contrast Enhancement in RII and Modification of the Therapeutic Ratio in RIT: A Theoretical Evaluation of Simulated Extracorporeal Immunoadsorbtion." Antobody.Immunoconj.Radiopharm. 5 (1992): 61-73.**

28. **Norrgren, K., et al. "A general, extracorporeal immunoadsorption method to increase the tumor-to-normal tissue ratio in radioimmunoimaging and radioimmunotherapy." J.Nucl.Med. 34.3 (1993): 448-54.**

29. O'Donoghue, J.A., "Dosimetric Principles of Targeted Radiotherapy" In: Abrams, P. G. and Fritzberg, A. R., (eds.) Radioimmunotherapy of Cancer, Marcel Dekker Inc., New York, 2000, pp. 1-20.

30. Odom-Maryon, T. L., et al. "Pharmacokinetic modeling and absorbed dose estimation for chimeric anti-CEA antibody in humans." J.Nucl.Med. 38.12 (1997): 1959-66.

31. Paganelli, G., et al. "Antibody-guided three-step therapy for high grade glioma with yttrium-90 biotin." Eur.J.Nucl.Med. 26.4 (1999): 348-57.

32. Saga, T., et al. "Targeting cancer micrometastases with monoclonal antibodies: a binding-site barrier." Proc.Natl.Acad.Sci.U.S.A 92.19 (1995): 8999-9003.

33. Sgouros, G. "Plasmapheresis in radioimmunotherapy of micrometastases: a mathematical modeling and dosimetrical analysis." J.Nucl.Med. 33.12 (1992): 2167-79.

34. Sgouros, G., et al. "Modeling and dosimetry of monoclonal antibody M195 (anti-CD33) in acute myelogenous leukemia." J.Nucl.Med. 34.3 (1993): 422-30.

35. Slavin-Chiorini, D.C., et al. "Antibodies and Novel Constructs for Tumor Targeting." In: Abrams, P. G. and Fritzberg, A. R., (eds.) Radioimmunotherapy of Cancer, Marcel Dekker Inc., New York, 2000, pp. 137-167.

36. Stabin, M. G., et al. "Radiation dosimetry in nuclear medicine." Appl.Radiat.Isot. 50.1 (1999): 73-87.

37. Strand, S. E., et al. "Extracorporeal Techniques in Radioimmunotherapy." In: Abrams, P. G. and Fritzberg, A. R., (eds.) Radioimmunotherapy of Cancer, Marcel Dekker Inc., New York, 2000, pp. 223-243.

38. Strand, S. E., P. Zanzonico, and T. K. Johnson. "Pharmacokinetic modeling." Med.Phys. 20.2 Pt 2 (1993): 515-27.

39. Sung, C., et al. "Predicted and observed effects of antibody affinity and antigen density on monoclonal antibody uptake in solid tumors." Cancer Res. 52.2 (1992): 377-84.

40. Sung, C., et al. "Streptavidin distribution in metastatic tumors pretargeted with a biotinylated monoclonal antibody: theoretical and experimental pharmacokinetics." Cancer Res. 54.8 (1994): 2166-75.

41. van Osdol, W. W., et al. "A distributed pharmacokinetic model of two-step imaging and treatment protocols: application to streptavidin-conjugated monoclonal antibodies and radiolabeled biotin." J.Nucl.Med. 34.9 (1993): 1552-64.

42. van, Osdol W., K. Fujimori, and J. N. Weinstein. "An analysis of monoclonal antibody distribution in microscopic tumor nodules: consequences of a "binding site barrier"." Cancer Res. 51.18 (1991): 4776-84.

43. **Williams, L. E., et al. "Figures of merit (FOMs) for imaging and therapy using monoclonal antibodies." Med.Phys. 22.12 (1995): 2025-27.**

44. **Williams, L. E., et al. "Truncation of blood curves to enhance imaging and therapy with monoclonal antibodies." Med.Phys. 27.5 (2000): 988-94.**

45. **Williams, L. E., et al. "On the correction for radioactive decay in pharmacokinetic modeling." Med.Phys. 22.10 (1995): 1619-26.**

46. **Williams, L. E., et al. "Numerical selection of optimal tumor imaging agents with application to engineered antibodies." Cancer Biother.Radiopharm. 16.1 (2001): 25-35.**

Appendix

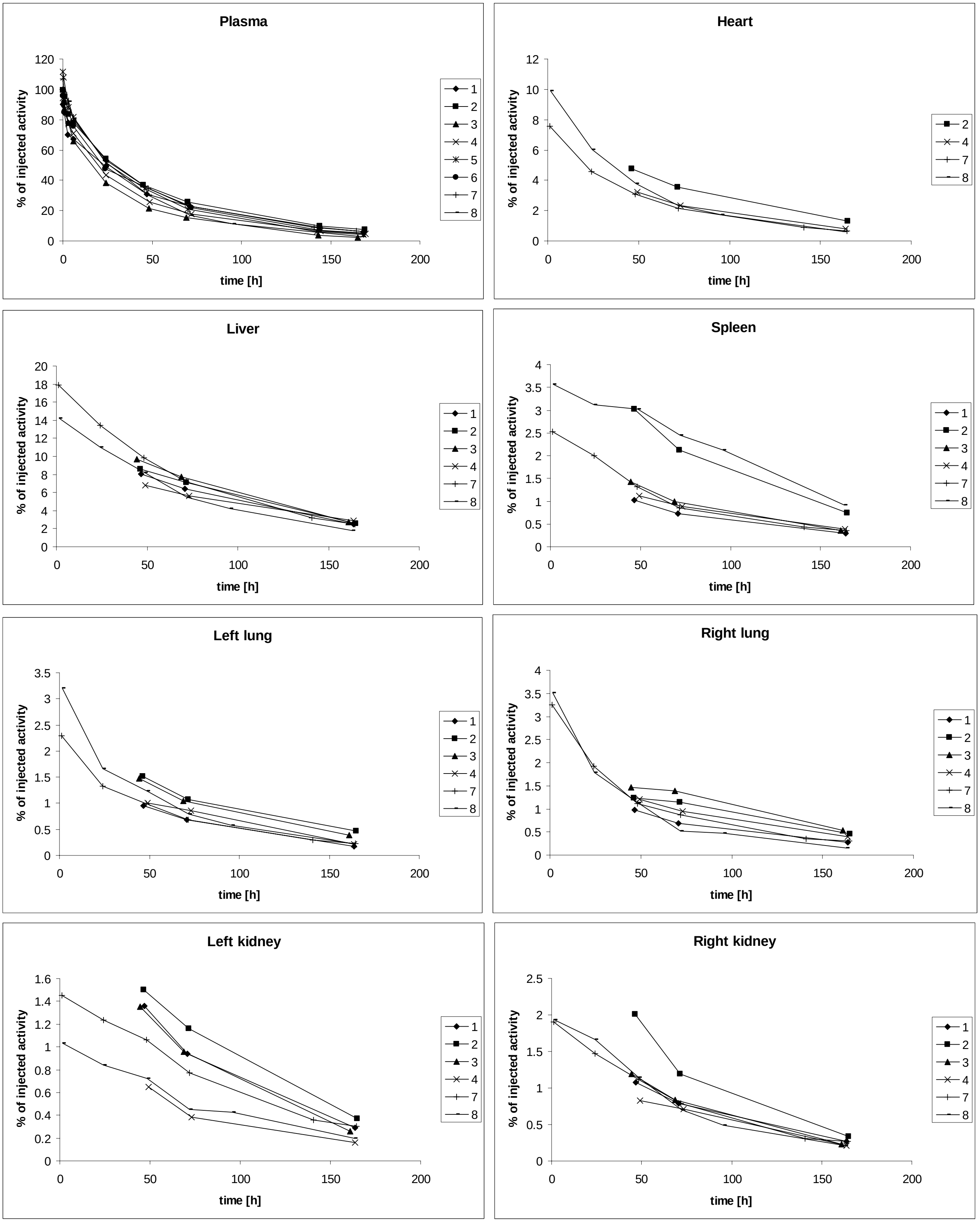

Fig A:1 Time-activity curves for the diagnostic phase

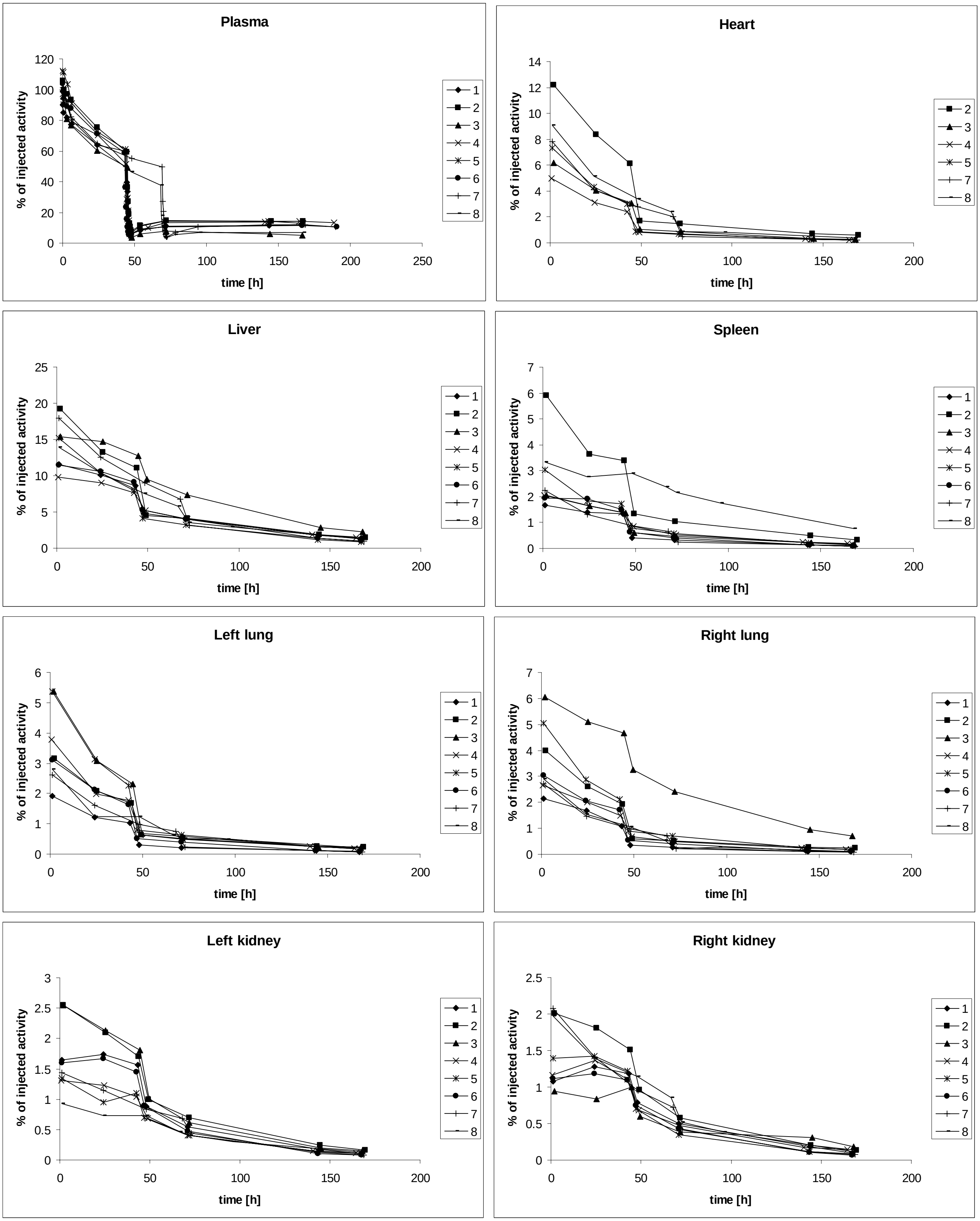

Fig A:2 Time-activity curves for therapeutic phase

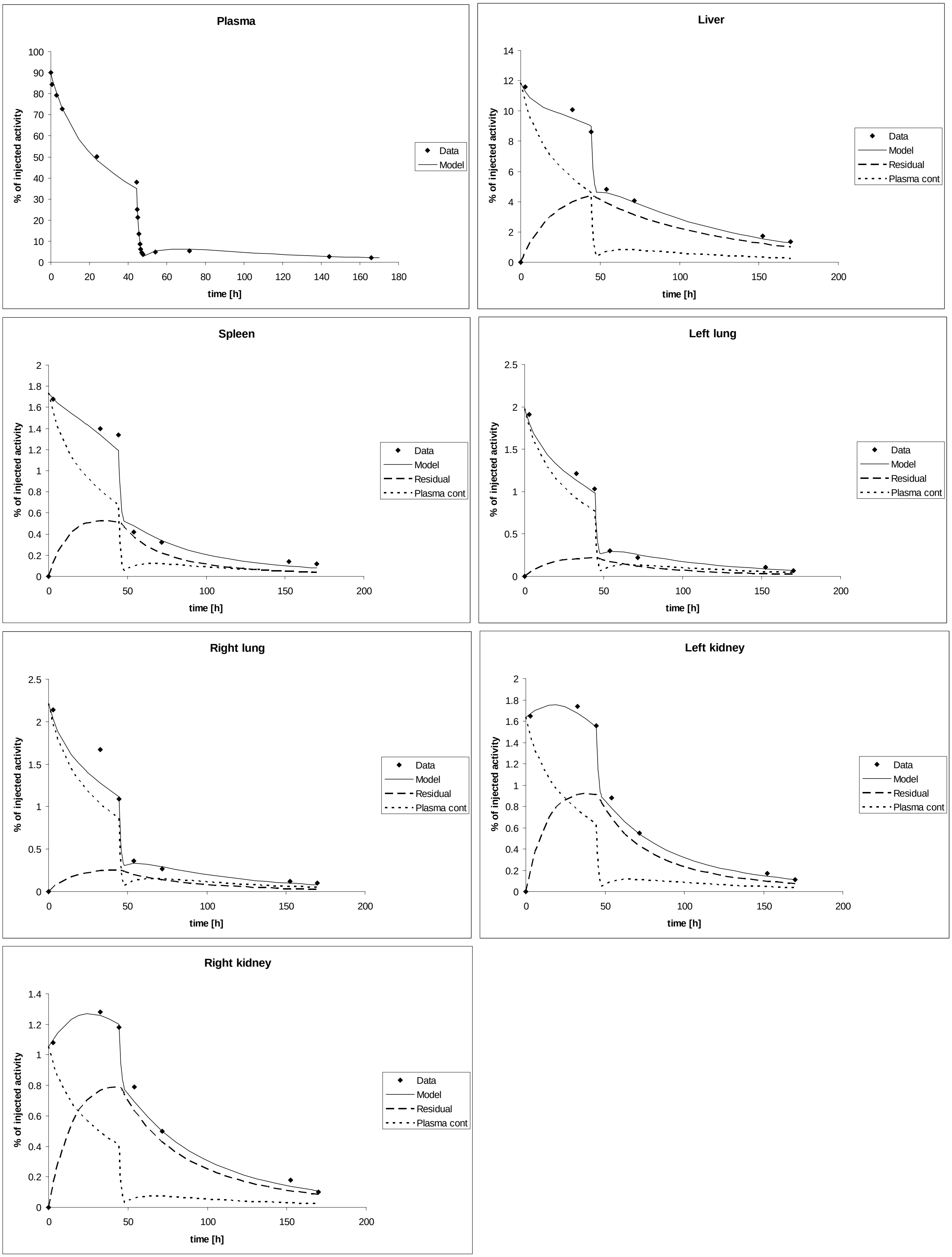

Fig A:3 Model plot for patient #1

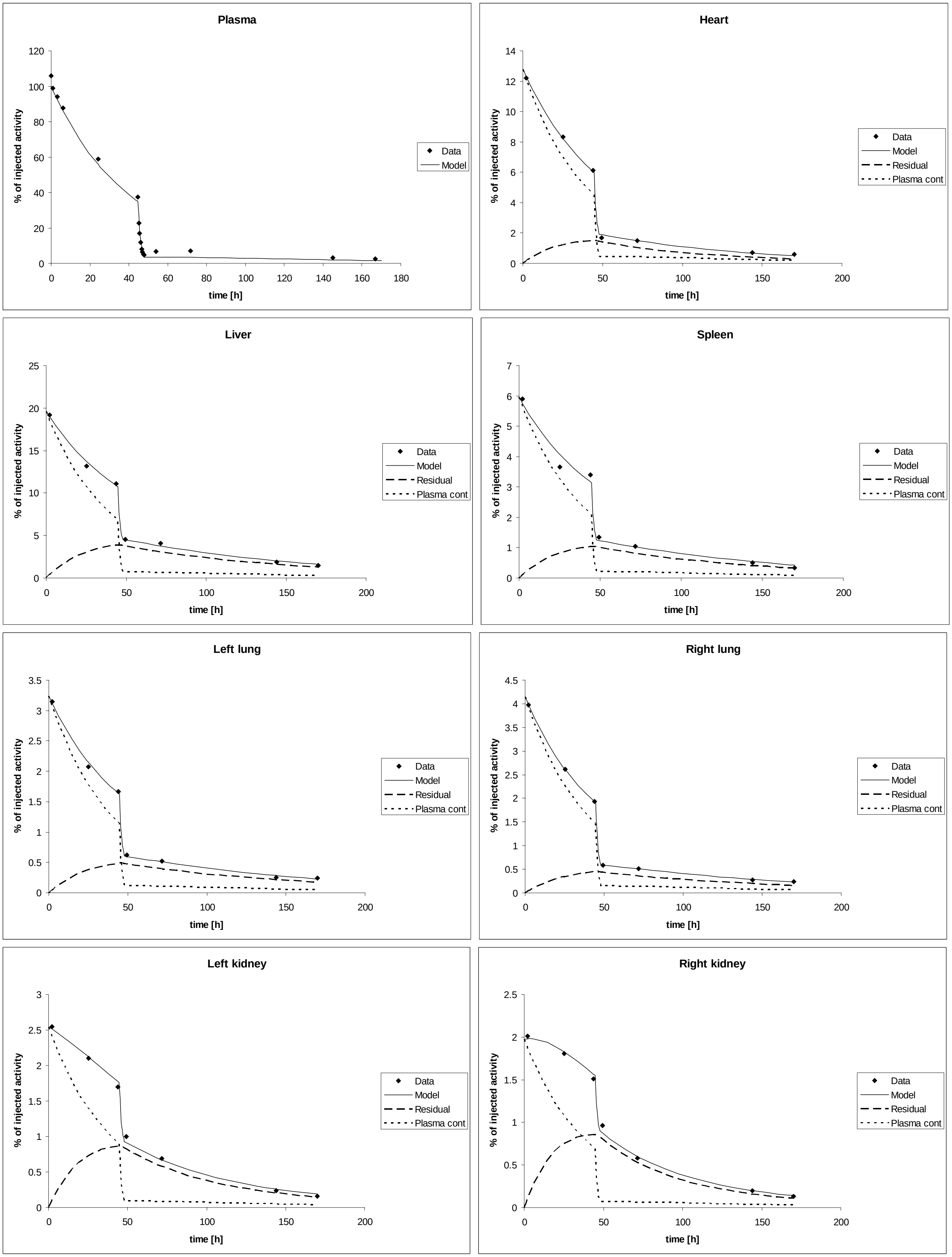

Fig A:4 Model plot for patient #2

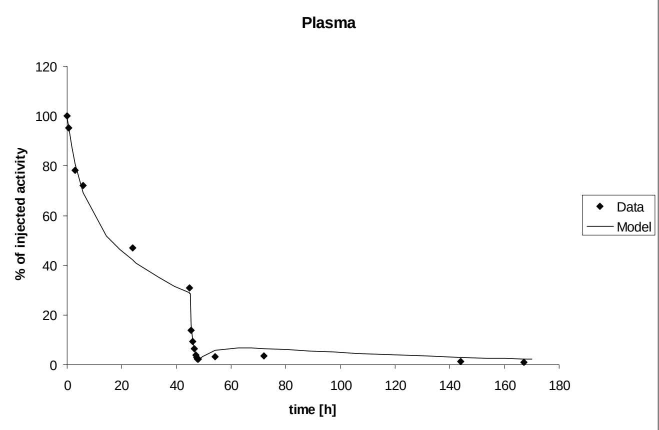
Plasma
% of injected activity
120
100
80
60
40
20
0
0
20
40
60
80
100
120
140
160
180
time [h]
Data
Model

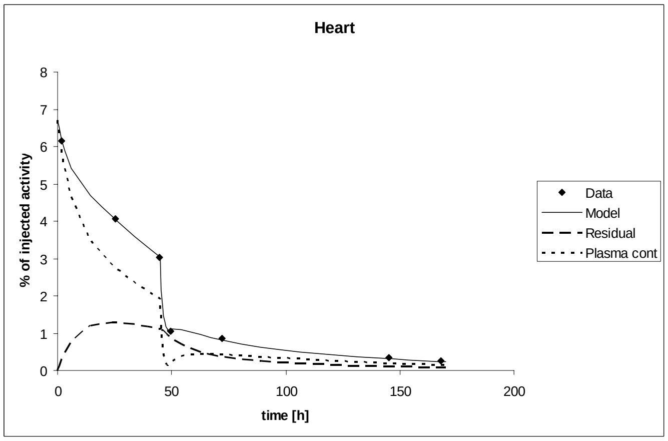
Heart
% of injected activity
8
7
6
5
4
3
2
1
0
0
50
100
150
200
time [h]
Data
Model
Residual
Plasma cont

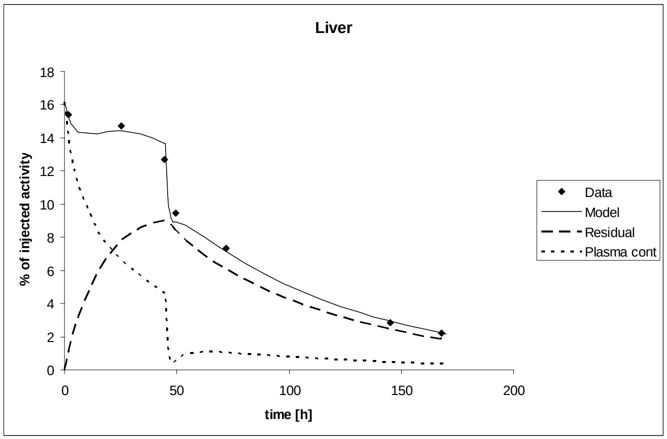
Liver
% of injected activity
18
16
14
12
10
8
6
4
2
0
0
50
100
150
200
time [h]
Data
Model
Residual
Plasma cont

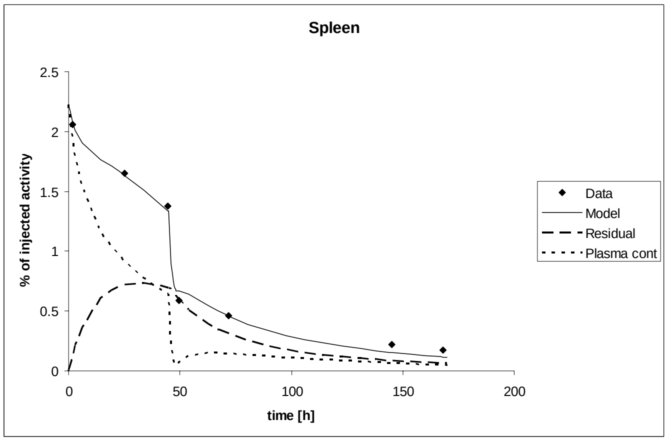
Spleen
% of injected activity
2.5
2
1.5
1
0.5
0
0
50
100
150
200
time [h]
Data
Model
Residual
Plasma cont

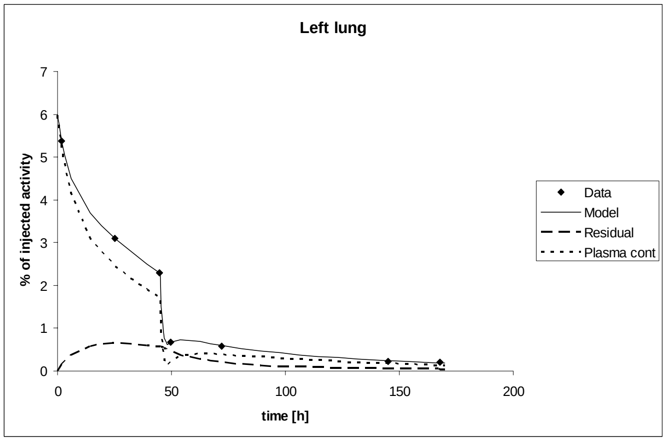
Left lung
% of injected activity
7
6
5
4
3
2
1
0
0
50
100
150
200
time [h]
Data
Model
Residual
Plasma cont

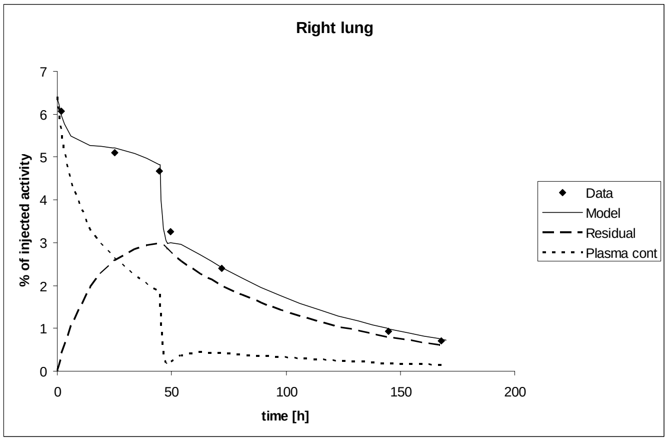
Right lung
% of injected activity
7
6
5
4
3
2
1
0
0
50
100
150
200
time [h]
Data
Model
Residual
Plasma cont

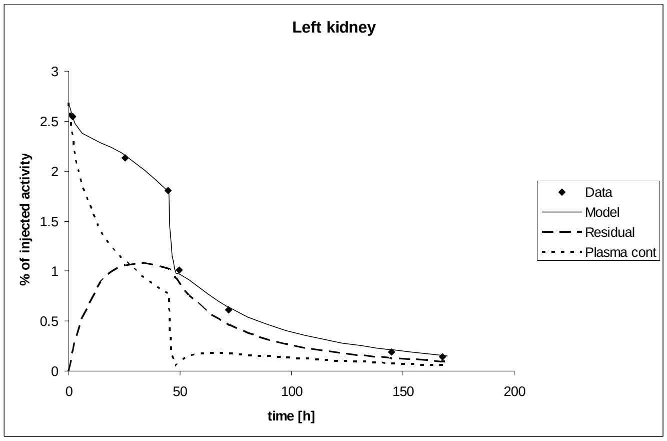
Left kidney
% of injected activity
3
2.5
2
1.5
1
0.5
0
0
50
100
150
200
time [h]
Data
Model
Residual
Plasma cont

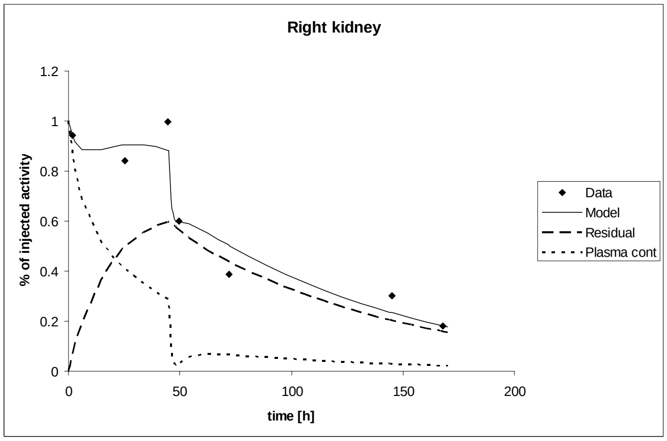
Right kidney
% of injected activity
1.2
1
0.8
0.6
0.4
0.2
0
0
50
100
150
200
time [h]
Data
Model
Residual
Plasma cont

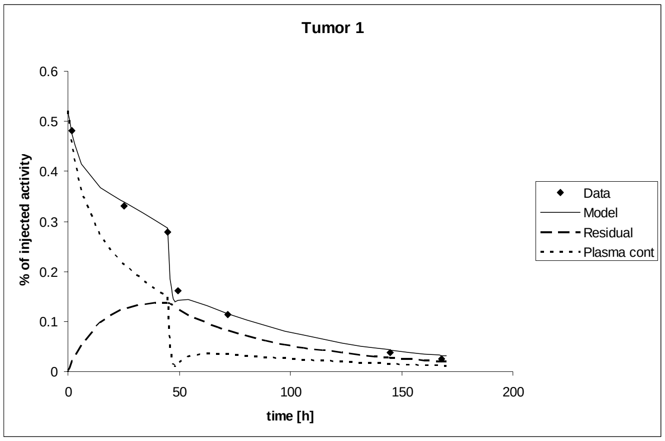

Fig A:5 Model plot for patient #3

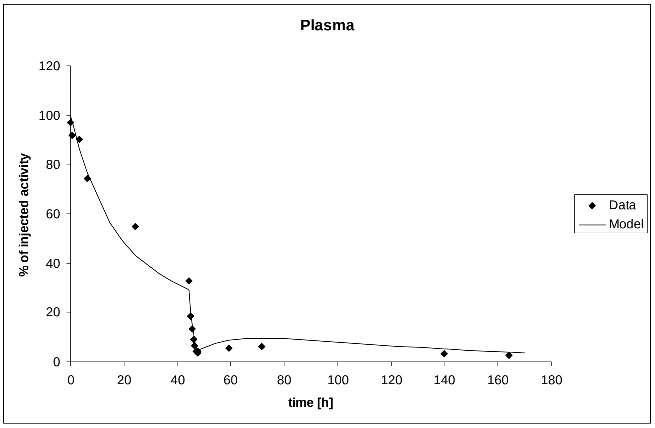
Plasma
120
100
80
60
40
20
0
% of injected activity
0
20
40
60
80
100
120
140
160
180
time [h]
Data
Model

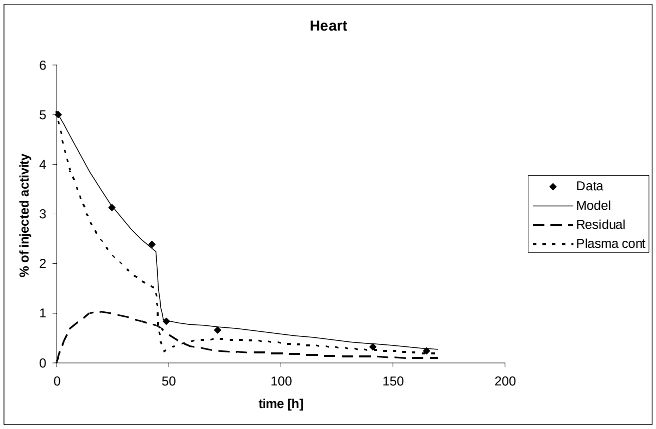
Heart
6
5
4
3
2
1
0
% of injected activity
0
50
100
150
200
time [h]
Data
Model
Residual
Plasma cont

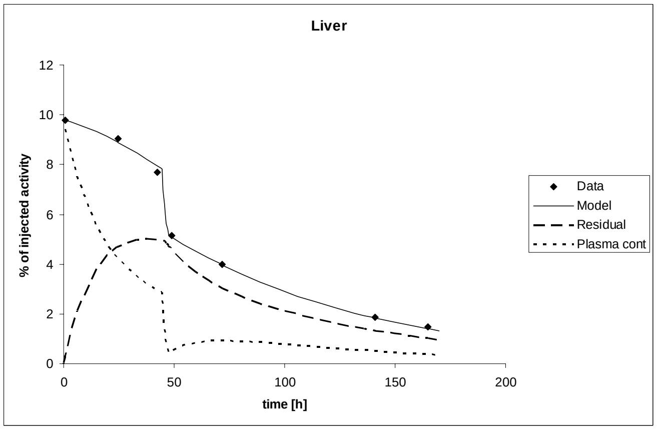
Liver
12
10
8
6
4
2
0
% of injected activity
0
50
100
150
200
time [h]
Data
Model
Residual
Plasma cont

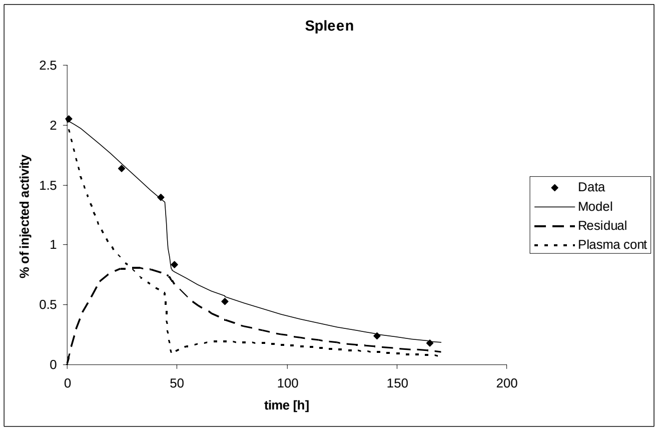
Spleen
2.5
2
1.5
1
0.5
0
% of injected activity
0
50
100
150
200
time [h]
Data
Model
Residual
Plasma cont

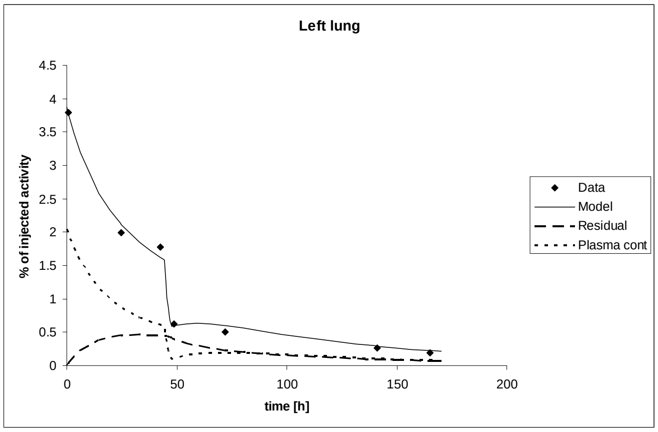
Left lung
4.5
4
3.5
3
2.5
2
1.5
1
0.5
0
% of injected activity
0
50
100
150
200
time [h]
Data
Model
Residual
Plasma cont

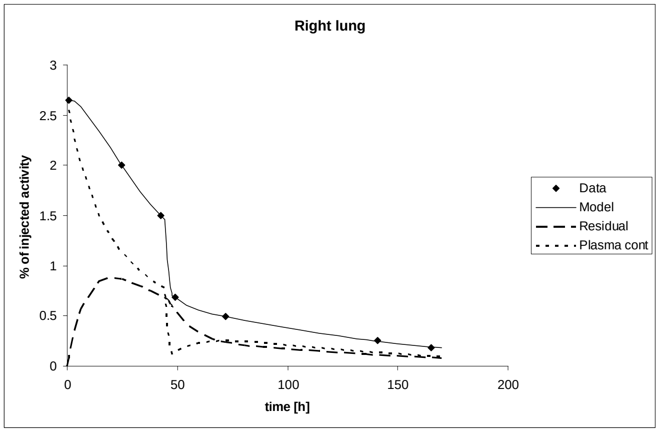
Right lung
3
2.5
2
1.5
1
0.5
0
% of injected activity
0
50
100
150
200
time [h]
Data
Model
Residual
Plasma cont

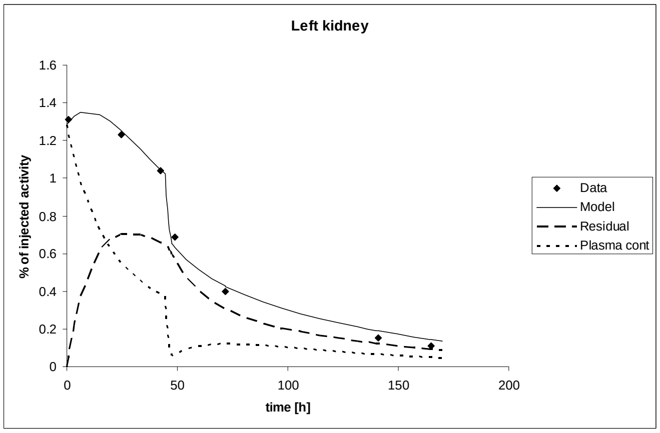
Left kidney
1.6
1.4
1.2
1
0.8
0.6
0.4
0.2
0
% of injected activity
0
50
100
150
200
time [h]
Data
Model
Residual
Plasma cont

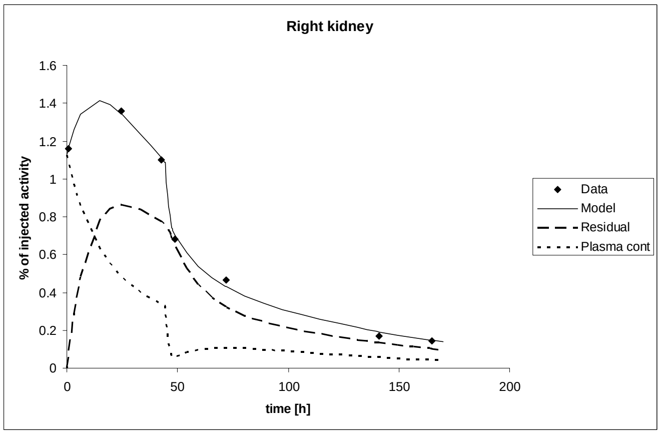
Right kidney
1.6
1.4
1.2
1
0.8
0.6
0.4
0.2
0
% of injected activity
0
50
100
150
200
time [h]
Data
Model
Residual
Plasma cont

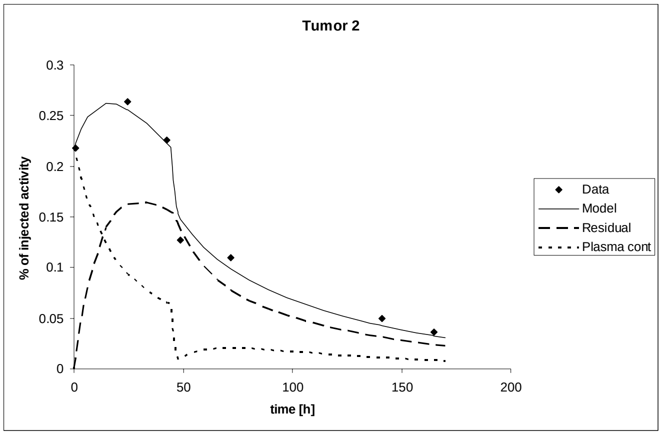

Fig A:6 Model plot for patient #4

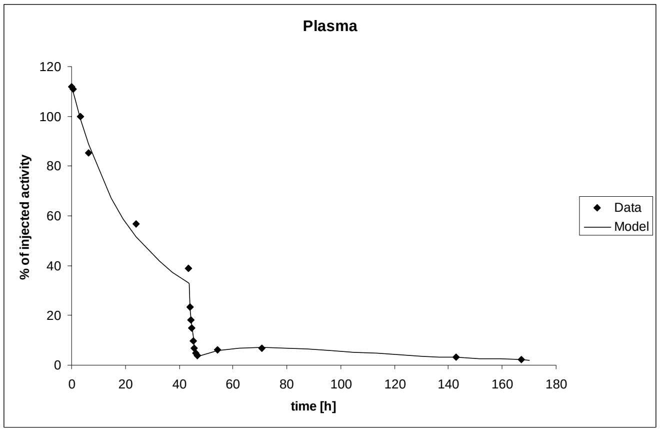
Plasma
% of injected activity
0
20
40
60
80
100
120
time [h]
0
20
40
60
80
100
120
140
160
180
Data
Model

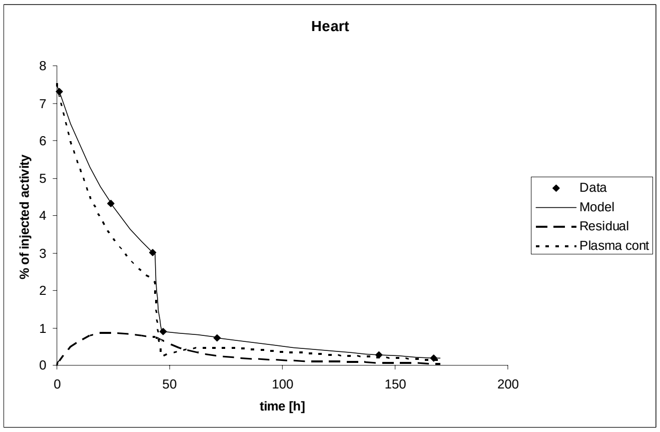
Heart
% of injected activity
0
1
2
3
4
5
6
7
8
time [h]
0
50
100
150
200
Data
Model
Residual
Plasma cont

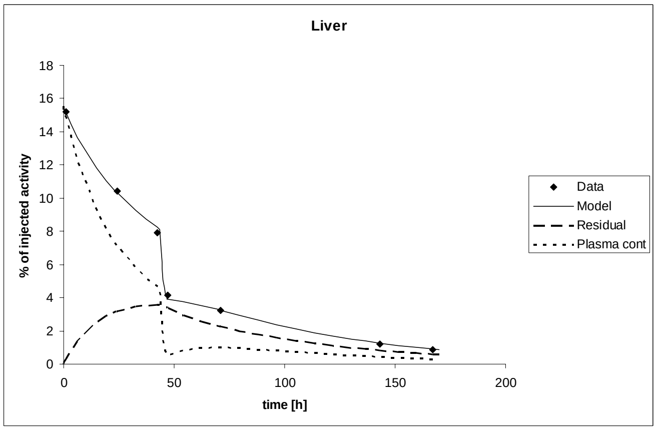
Liver
% of injected activity
0
2
4
6
8
10
12
14
16
18
time [h]
0
50
100
150
200
Data
Model
Residual
Plasma cont

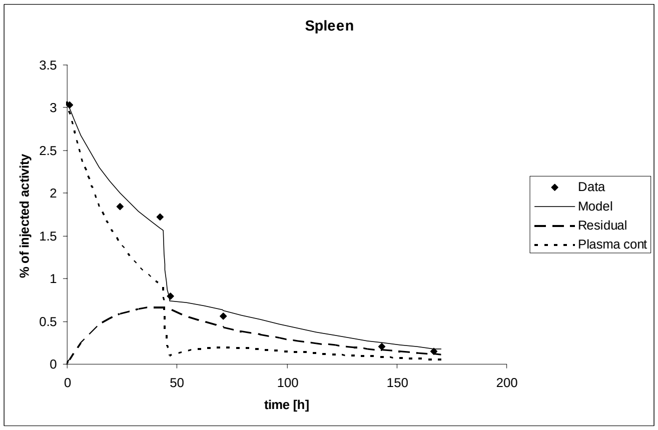
Spleen
% of injected activity
0
0.5
1
1.5
2
2.5
3
3.5
time [h]
0
50
100
150
200
Data
Model
Residual
Plasma cont

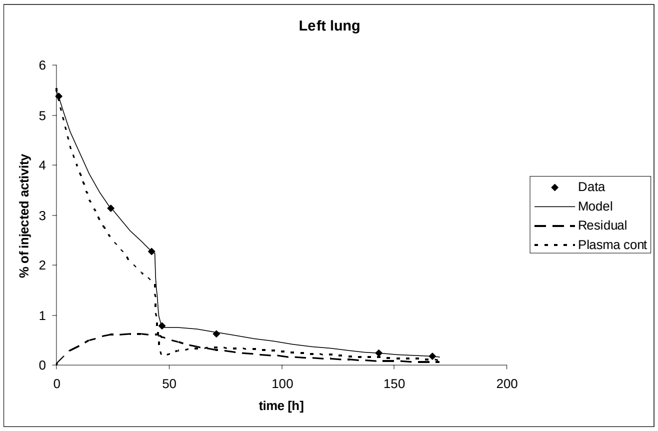
Left lung
% of injected activity
0
1
2
3
4
5
6
time [h]
0
50
100
150
200
Data
Model
Residual
Plasma cont

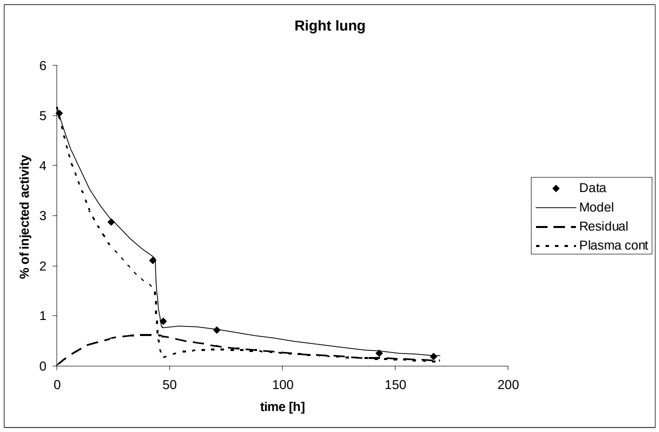
Right lung
% of injected activity
0
1
2
3
4
5
6
time [h]
0
50
100
150
200
Data
Model
Residual
Plasma cont

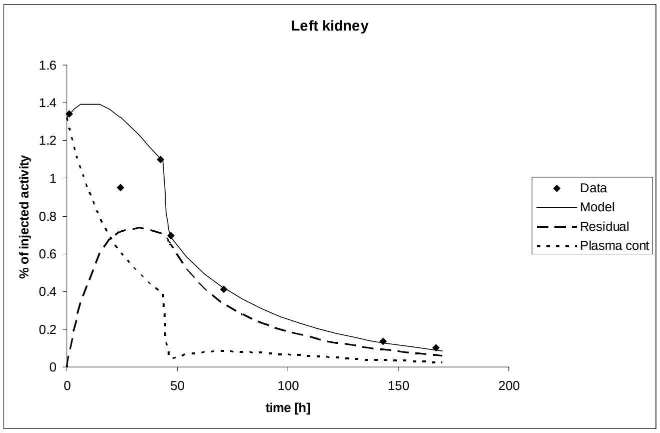
Left kidney
% of injected activity
0
0.2
0.4
0.6
0.8
1
1.2
1.4
1.6
time [h]
0
50
100
150
200
Data
Model
Residual
Plasma cont

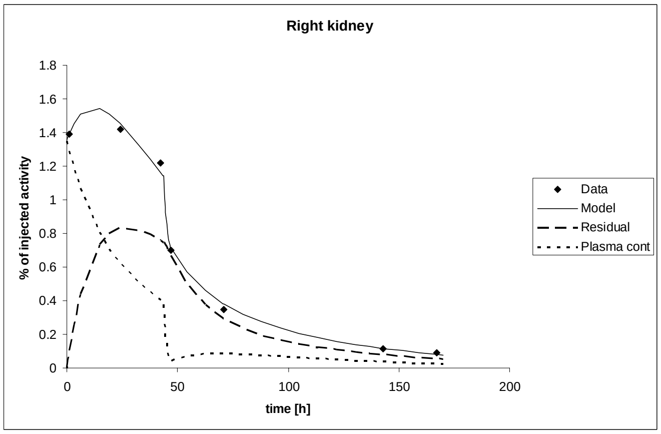
Right kidney
% of injected activity
0
0.2
0.4
0.6
0.8
1
1.2
1.4
1.6
1.8
time [h]
0
50
100
150
200
Data
Model
Residual
Plasma cont

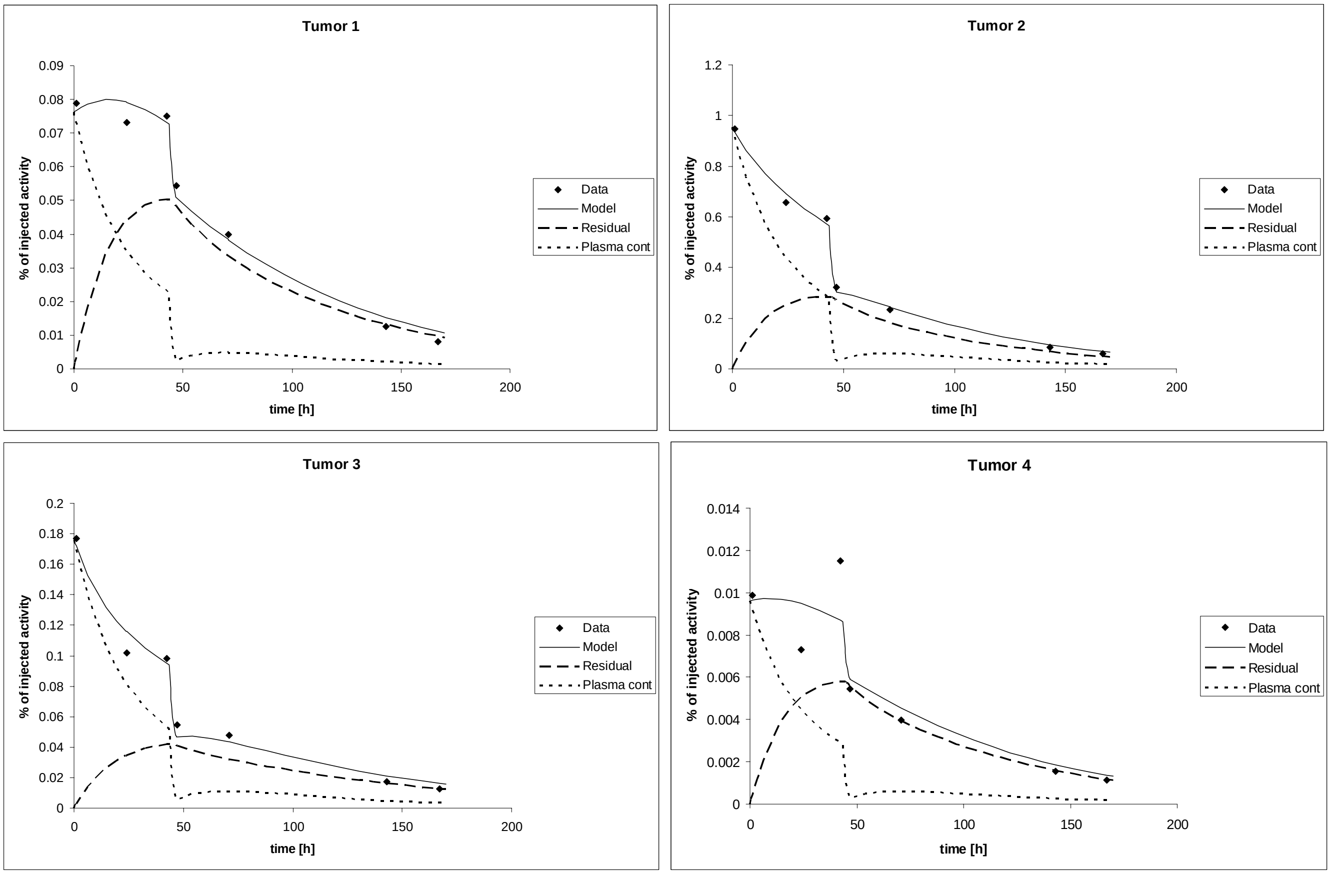

Fig A:7 Model plot for patient #5

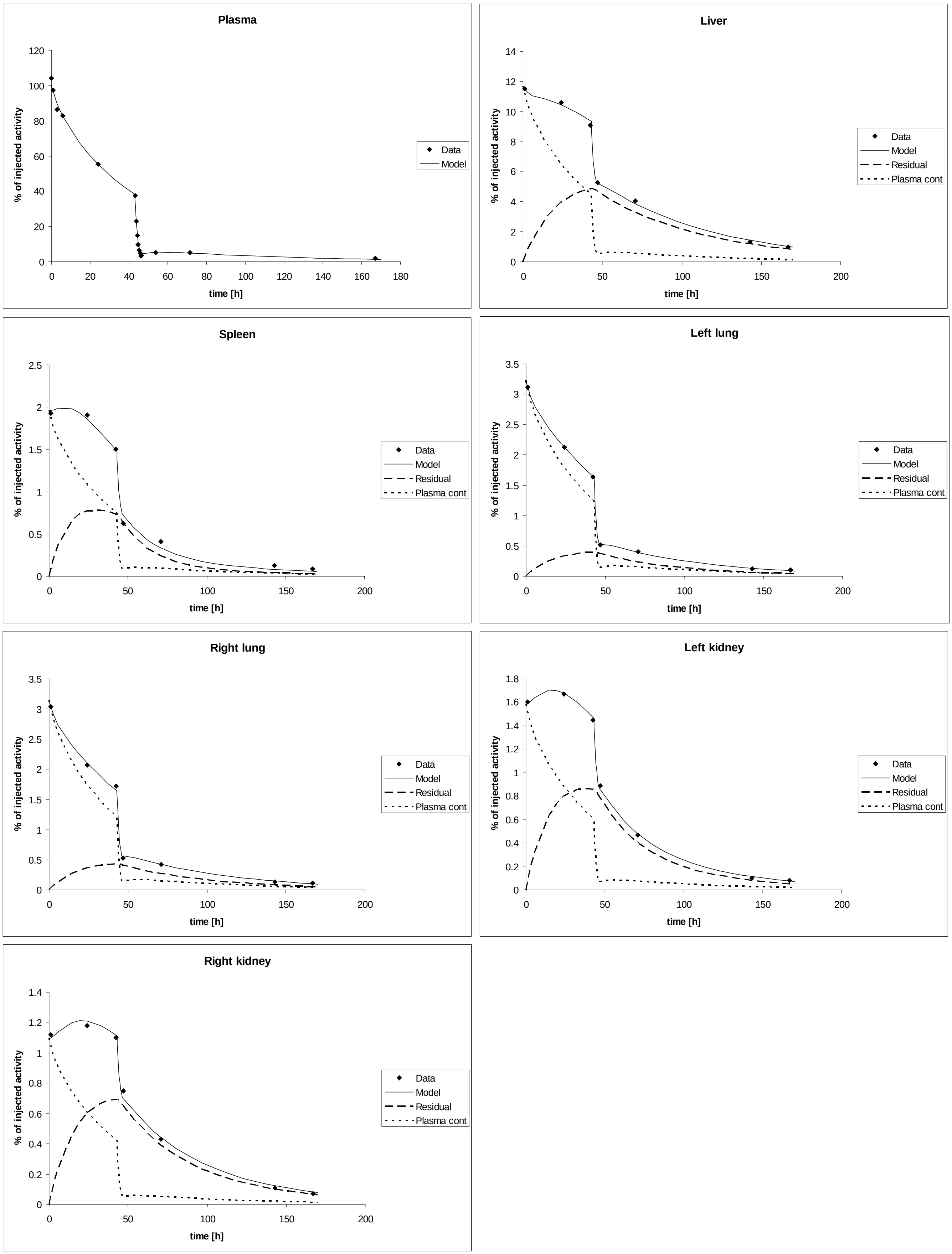
Plasma

Liver

Spleen

Left lung

Right lung

Left kidney

Right kidney

Fig A:8 Model plot for patient #6

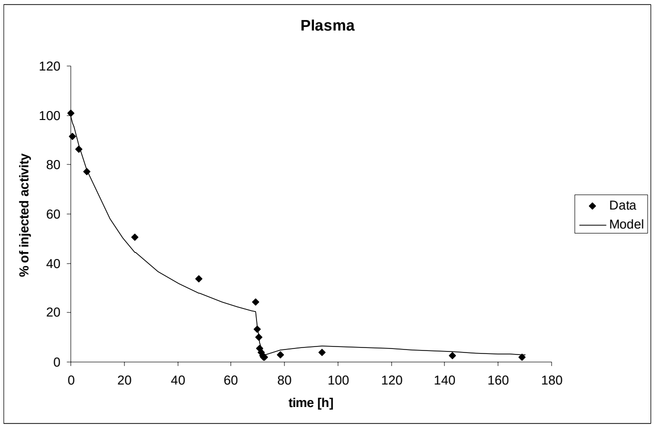
Plasma
% of injected activity
0
20
40
60
80
100
120
time [h]
0
20
40
60
80
100
120
140
160
180
Data
Model

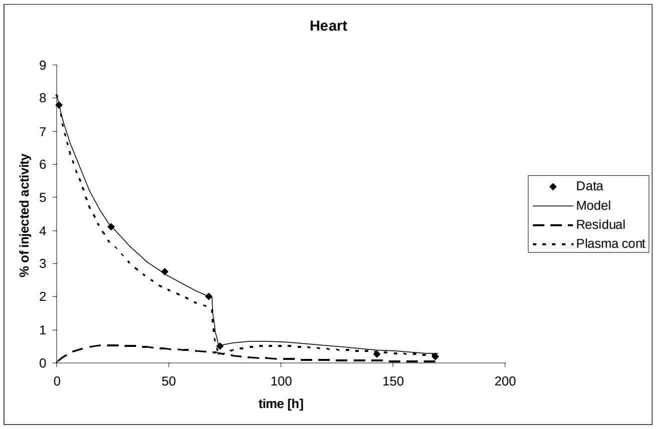
Heart
% of injected activity
0
1
2
3
4
5
6
7
8
9
time [h]
0
50
100
150
200
Data
Model
Residual
Plasma cont

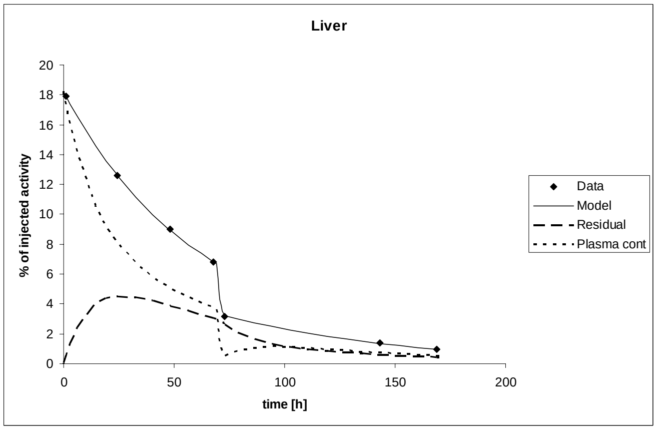
Liver
% of injected activity
0
2
4
6
8
10
12
14
16
18
20
time [h]
0
50
100
150
200
Data
Model
Residual
Plasma cont

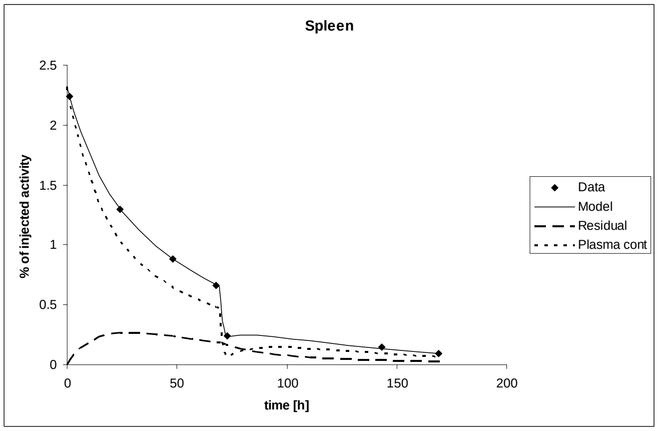
Spleen
% of injected activity
0
0.5
1
1.5
2
2.5
time [h]
0
50
100
150
200
Data
Model
Residual
Plasma cont

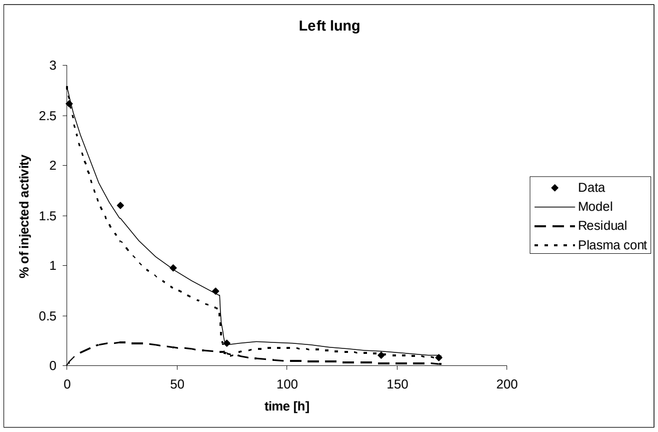
Left lung
% of injected activity
0
0.5
1
1.5
2
2.5
3
time [h]
0
50
100
150
200
Data
Model
Residual
Plasma cont

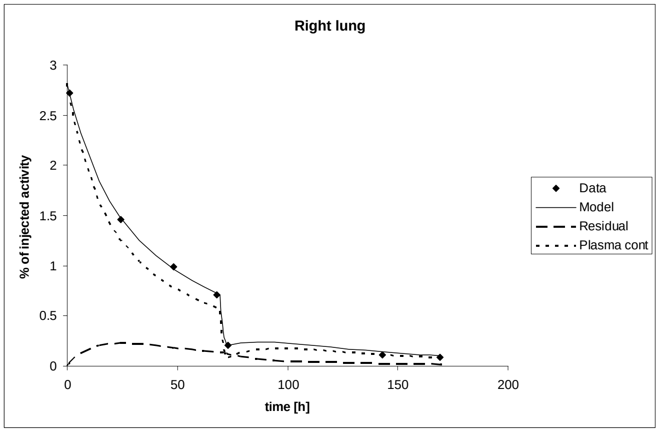
Right lung
% of injected activity
0
0.5
1
1.5
2
2.5
3
time [h]
0
50
100
150
200
Data
Model
Residual
Plasma cont

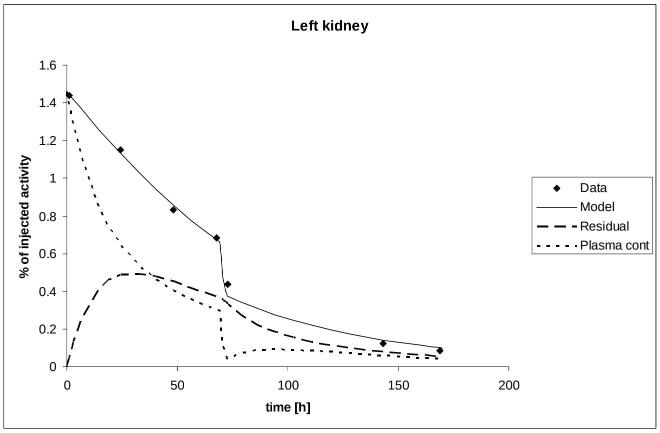
Left kidney
% of injected activity
0
0.2
0.4
0.6
0.8
1
1.2
1.4
1.6
time [h]
0
50
100
150
200
Data
Model
Residual
Plasma cont

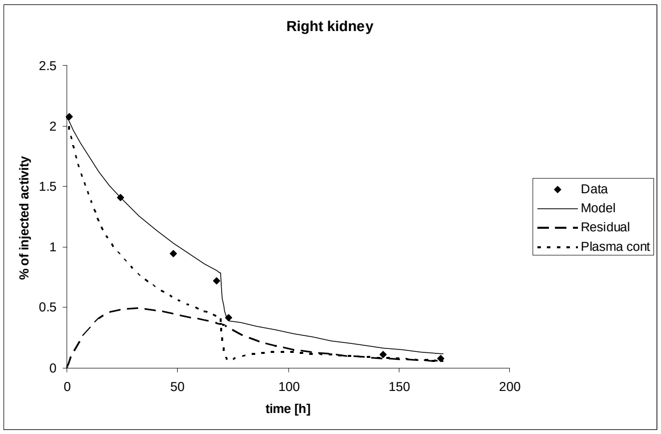
Right kidney
% of injected activity
0
0.5
1
1.5
2
2.5
time [h]
0
50
100
150
200
Data
Model
Residual
Plasma cont

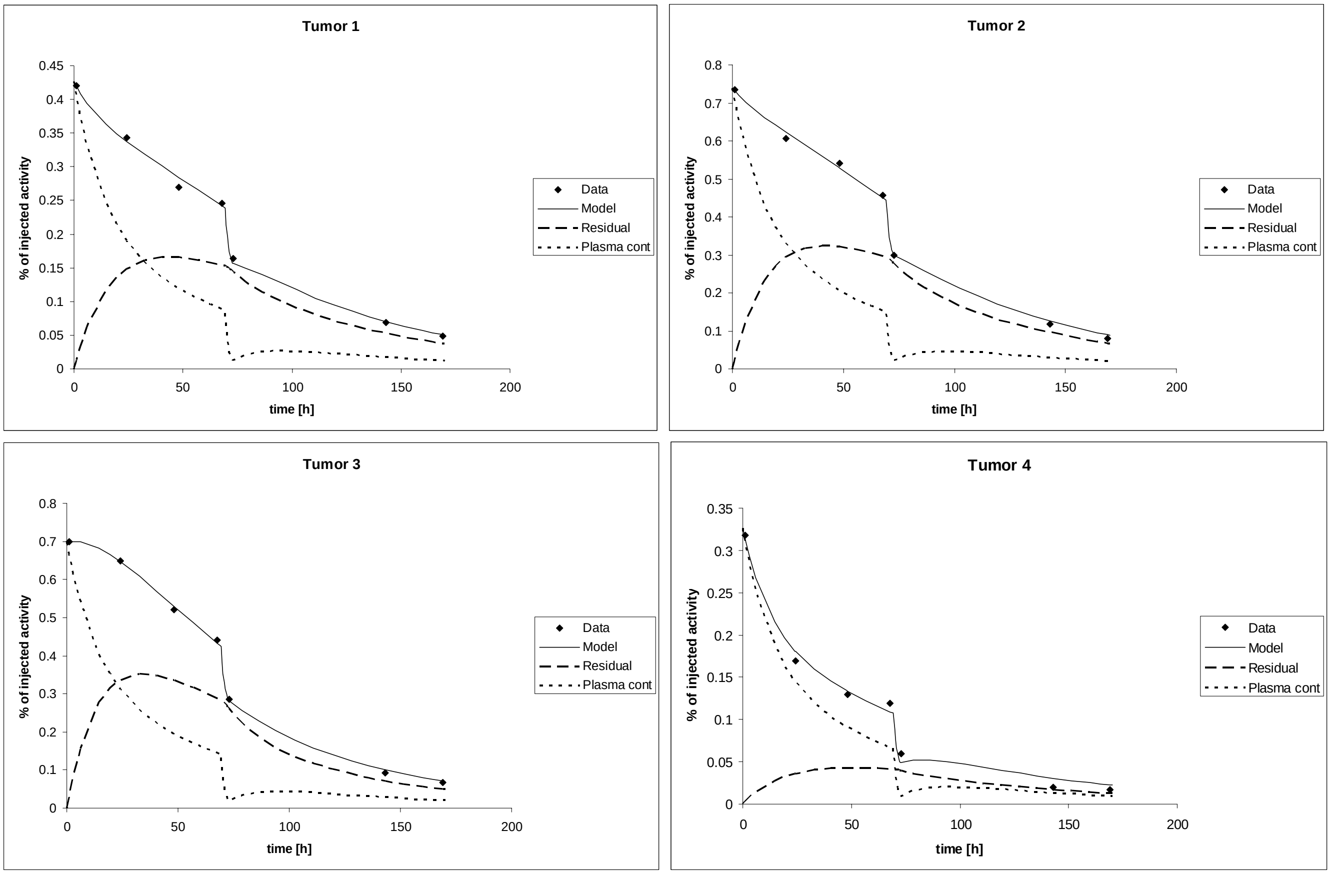

Fig A:9a Model plot for patient #7 (therapeutic part)

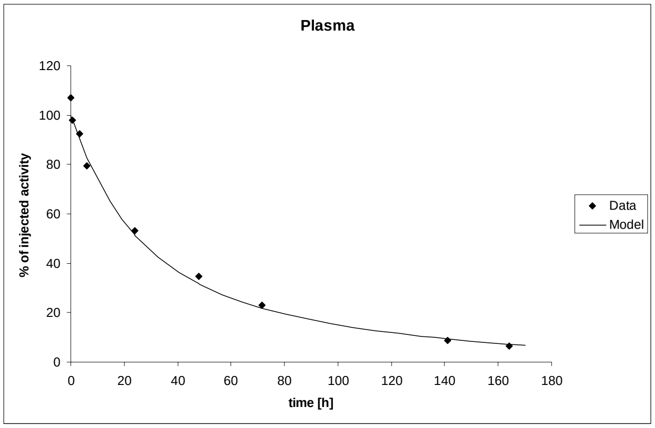
Plasma
% of injected activity
0
20
40
60
80
100
120
time [h]
0
20
40
60
80
100
120
140
160
180
Data
Model

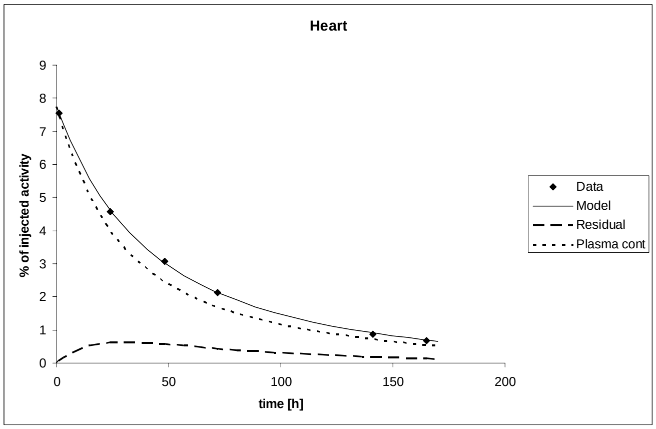
Heart
% of injected activity
0
1
2
3
4
5
6
7
8
9
time [h]
0
50
100
150
200
Data
Model
Residual
Plasma cont

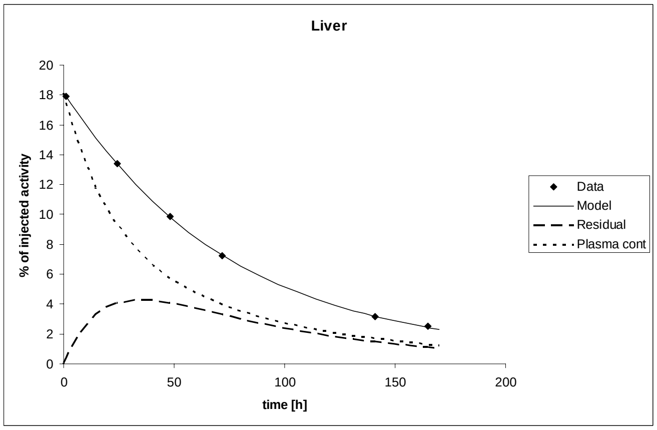
Liver
% of injected activity
0
2
4
6
8
10
12
14
16
18
20
time [h]
0
50
100
150
200
Data
Model
Residual
Plasma cont

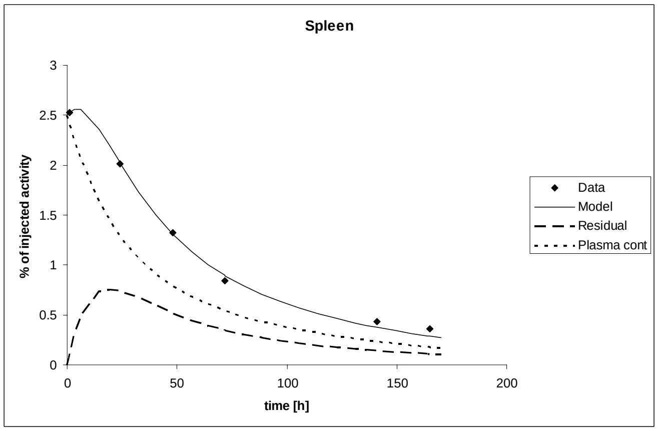
Spleen
% of injected activity
0
0.5
1
1.5
2
2.5
3
time [h]
0
50
100
150
200
Data
Model
Residual
Plasma cont

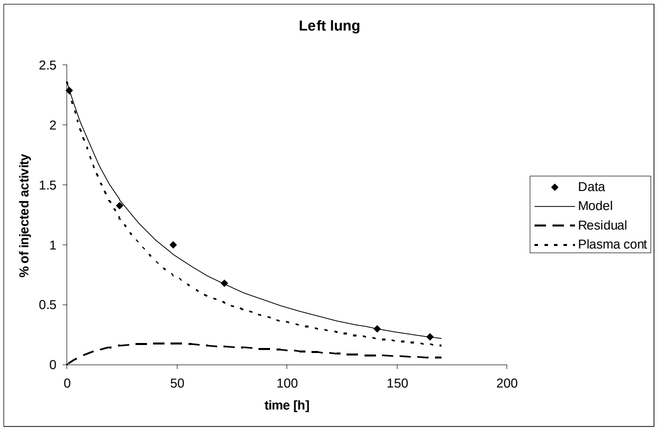
Left lung
% of injected activity
0
0.5
1
1.5
2
2.5
time [h]
0
50
100
150
200
Data
Model
Residual
Plasma cont

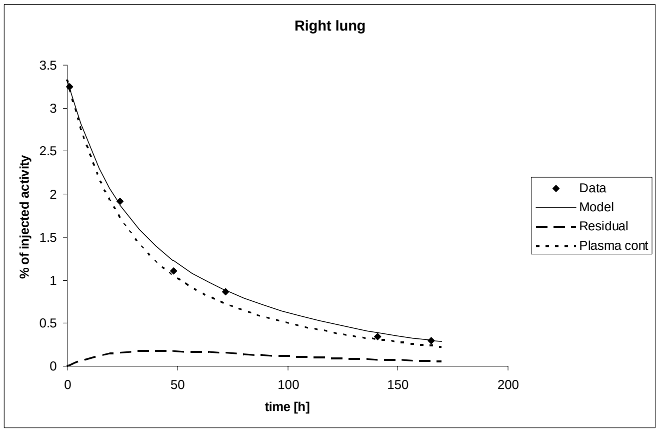
Right lung
% of injected activity
0
0.5
1
1.5
2
2.5
3
3.5
time [h]
0
50
100
150
200
Data
Model
Residual
Plasma cont

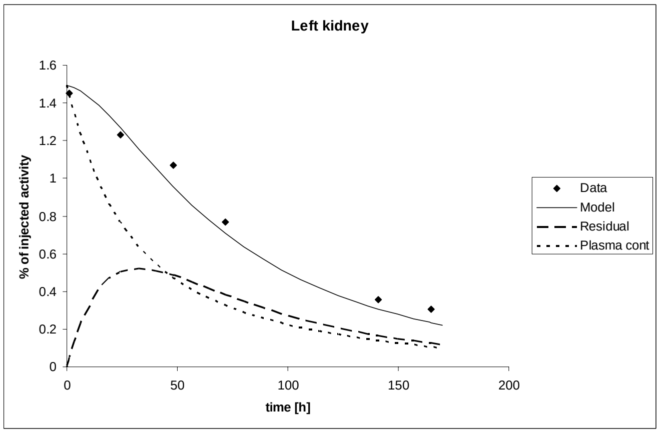
Left kidney
% of injected activity
0
0.2
0.4
0.6
0.8
1
1.2
1.4
1.6
time [h]
0
50
100
150
200
Data
Model
Residual
Plasma cont

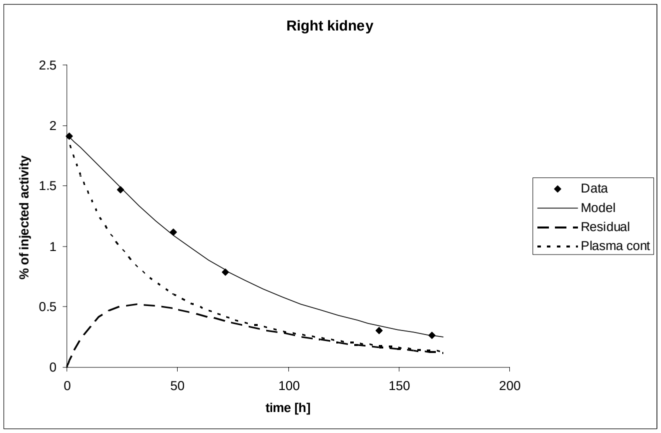
Right kidney
% of injected activity
0
0.5
1
1.5
2
2.5
time [h]
0
50
100
150
200
Data
Model
Residual
Plasma cont

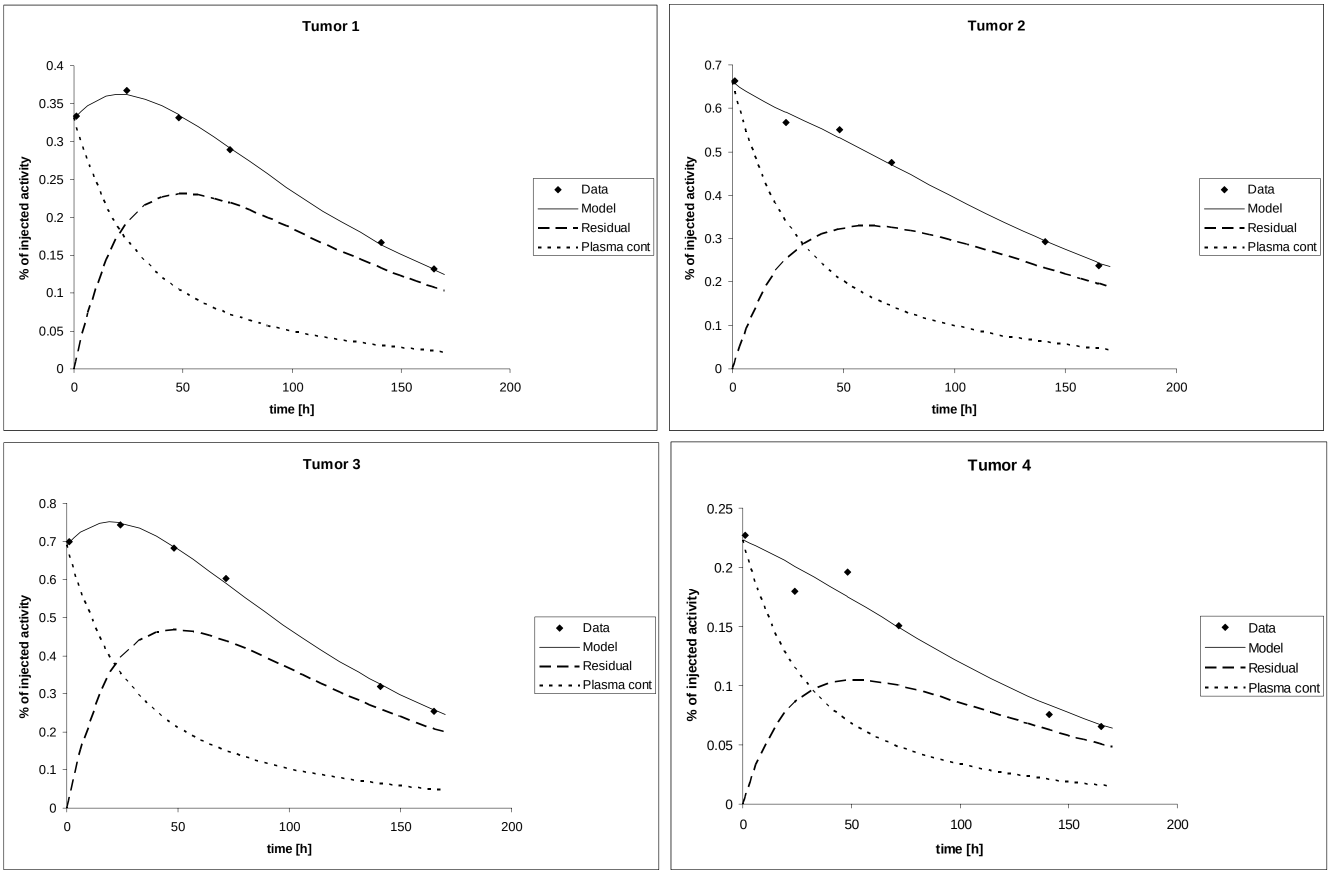

Fig A:9b Model plot for patient #7 (diagnostic part)

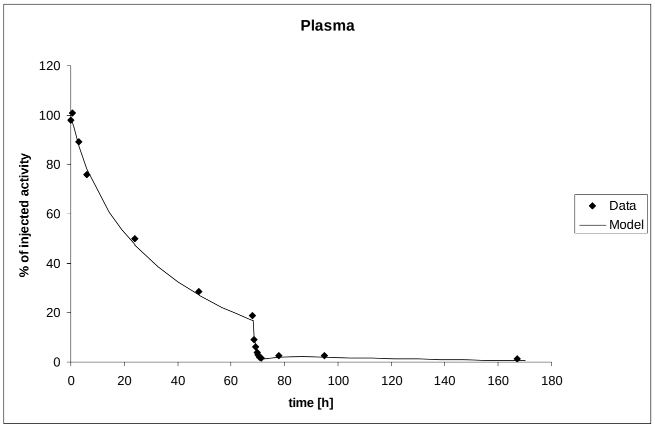
Plasma
% of injected activity
120
100
80
60
40
20
0
0
20
40
60
80
100
120
140
160
180
time [h]
Data
Model

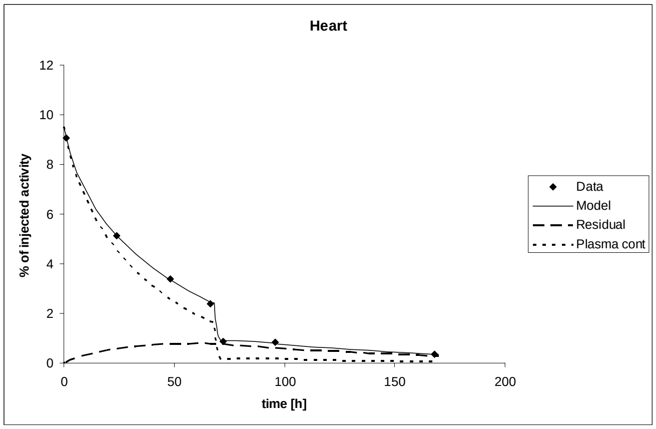
Heart
% of injected activity
12
10
8
6
4
2
0
0
50
100
150
200
time [h]
Data
Model
Residual
Plasma cont

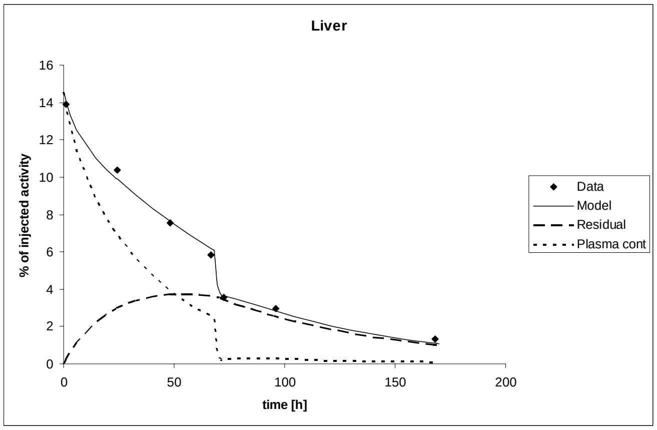
Liver
% of injected activity
16
14
12
10
8
6
4
2
0
0
50
100
150
200
time [h]
Data
Model
Residual
Plasma cont

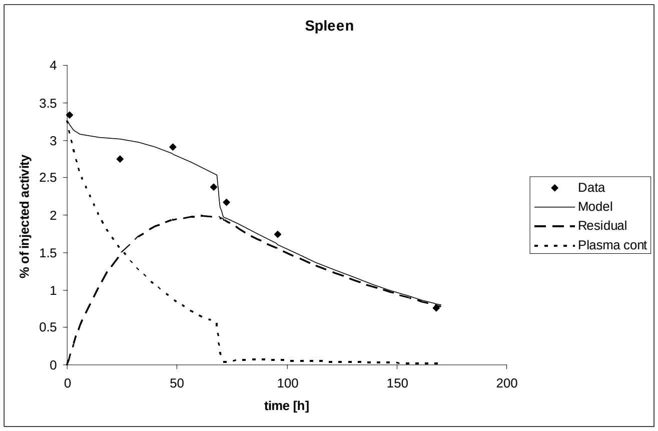
Spleen
% of injected activity
4
3.5
3
2.5
2
1.5
1
0.5
0
0
50
100
150
200
time [h]
Data
Model
Residual
Plasma cont

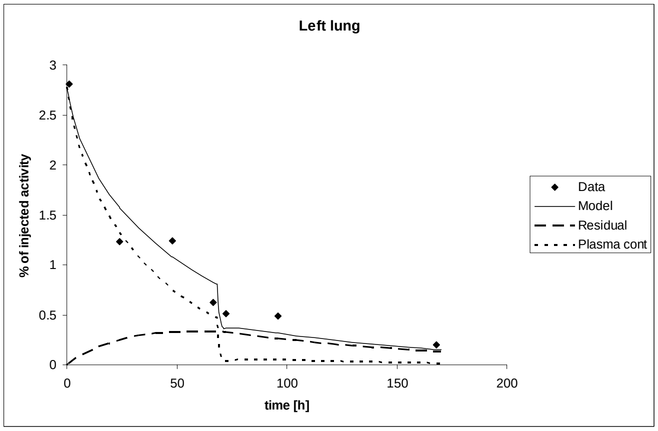
Left lung
% of injected activity
3
2.5
2
1.5
1
0.5
0
0
50
100
150
200
time [h]
Data
Model
Residual
Plasma cont

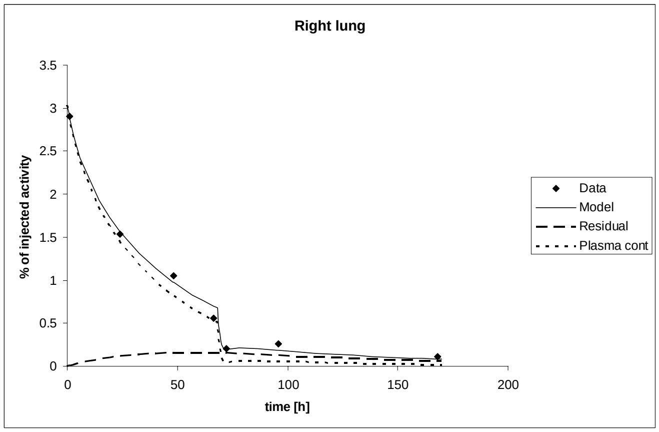
Right lung
% of injected activity
3.5
3
2.5
2
1.5
1
0.5
0
0
50
100
150
200
time [h]
Data
Model
Residual
Plasma cont

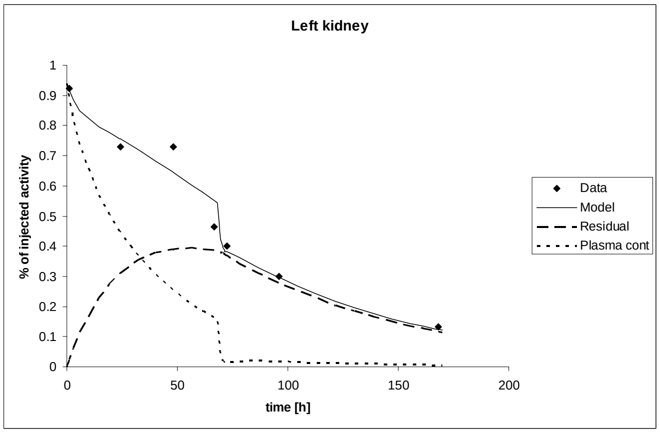
Left kidney
% of injected activity
1
0.9
0.8
0.7
0.6
0.5
0.4
0.3
0.2
0.1
0
0
50
100
150
200
time [h]
Data
Model
Residual
Plasma cont

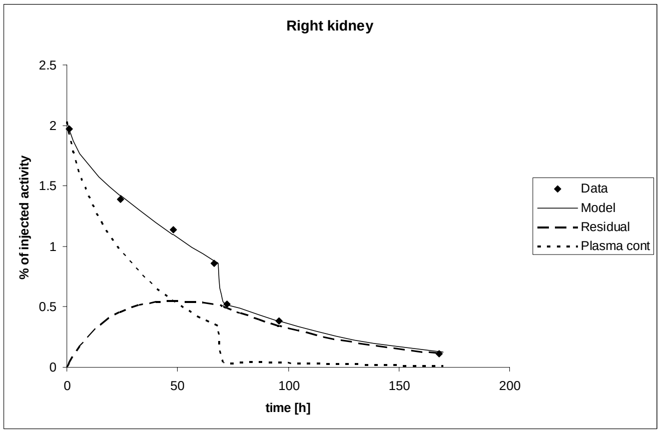
Right kidney
% of injected activity
2.5
2
1.5
1
0.5
0
0
50
100
150
200
time [h]
Data
Model
Residual
Plasma cont

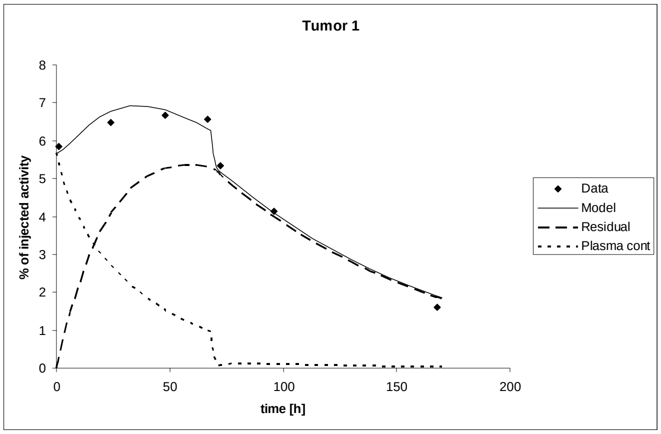

Fig A:10a Model plot for patient #8 (therapeutic part)

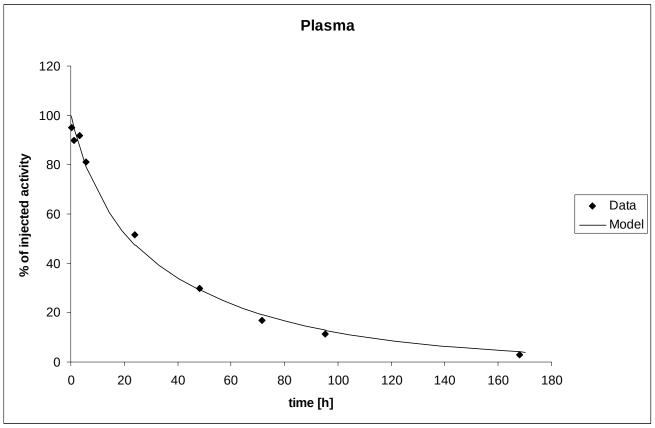
Plasma

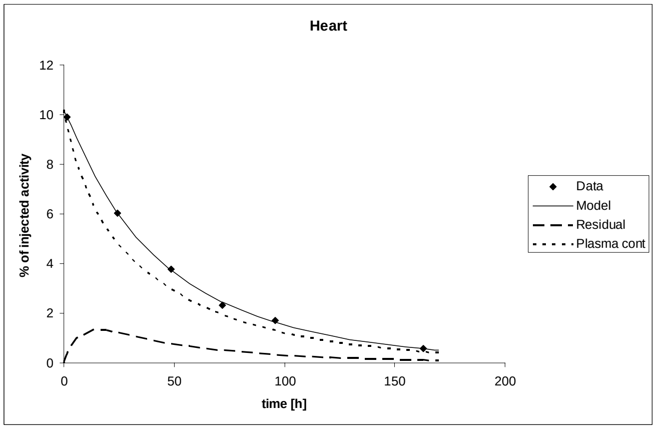
Heart

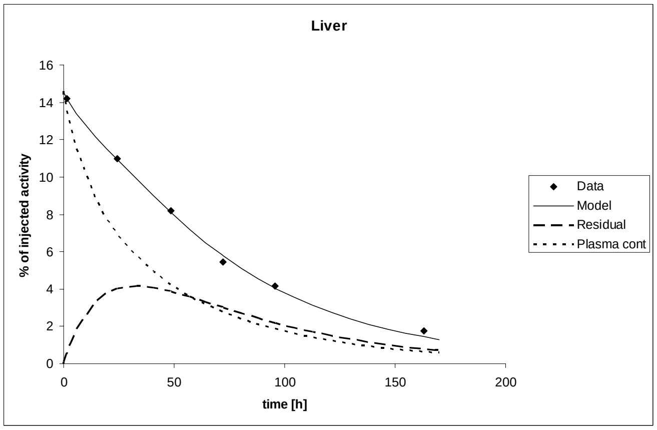
Liver

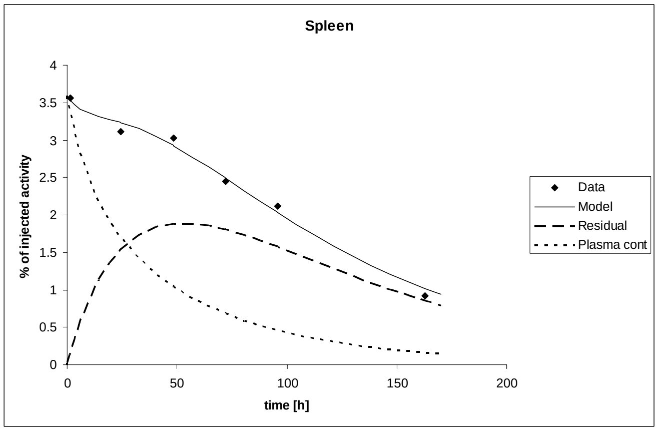
Spleen

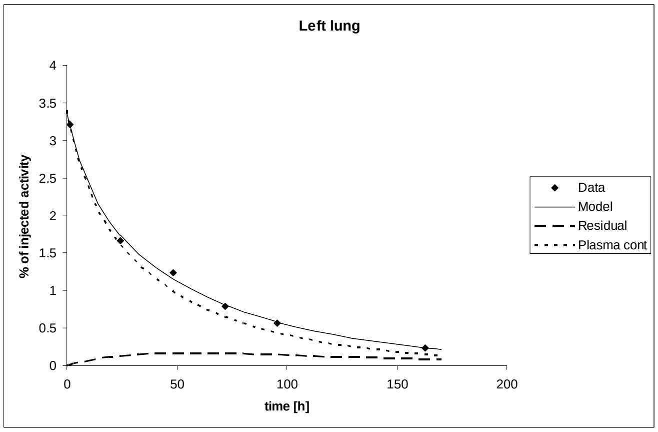
Left lung

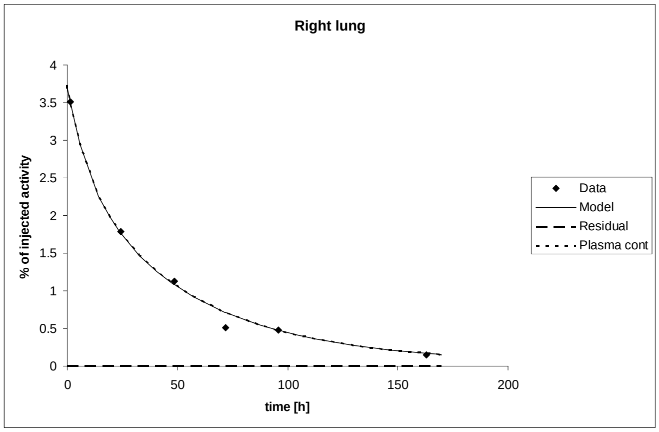
Right lung

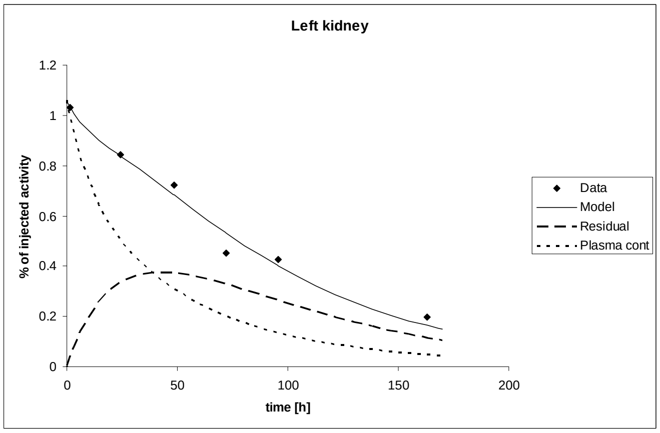
Left kidney

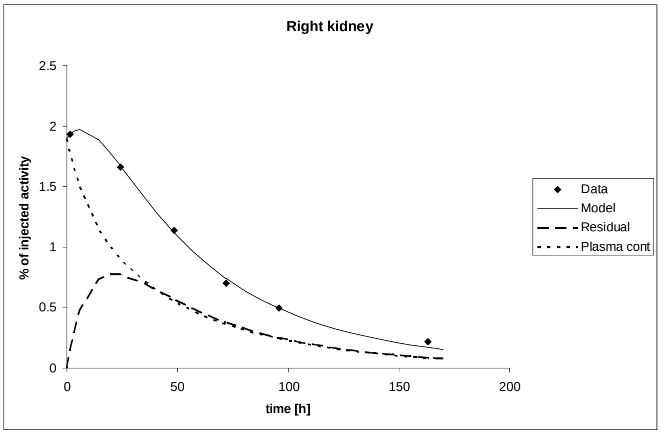
Right kidney

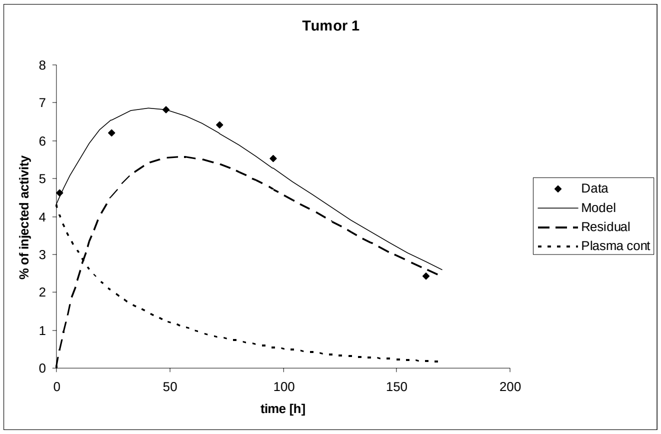

Fig A:10b Model plot for patient #8 (diagnostic part)

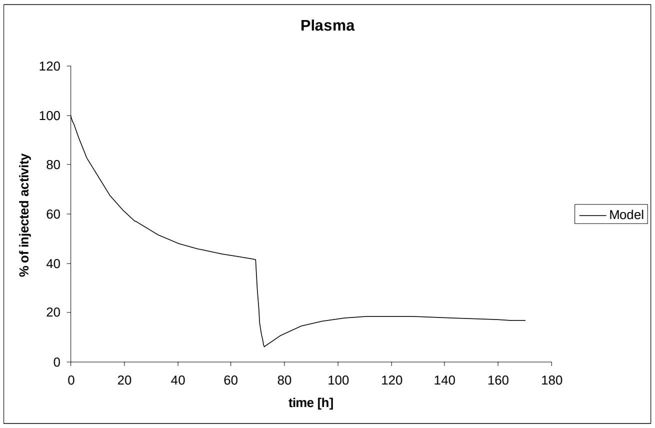
Plasma
% of injected activity
0
20
40
60
80
100
120
0
20
40
60
80
100
120
140
160
180
time [h]
Model

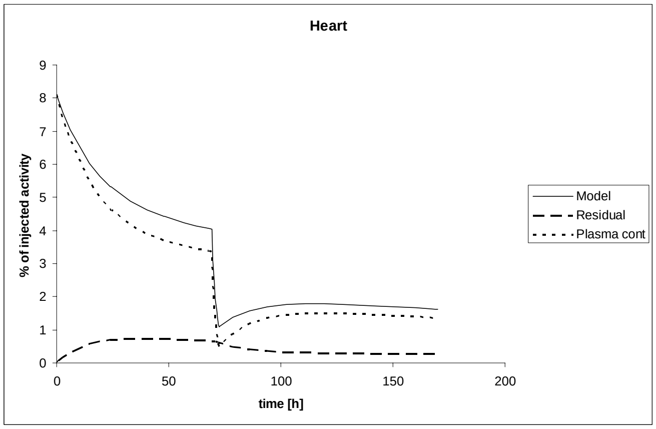
Heart
% of injected activity
0
1
2
3
4
5
6
7
8
9
0
50
100
150
200
time [h]
Model
Residual
Plasma cont

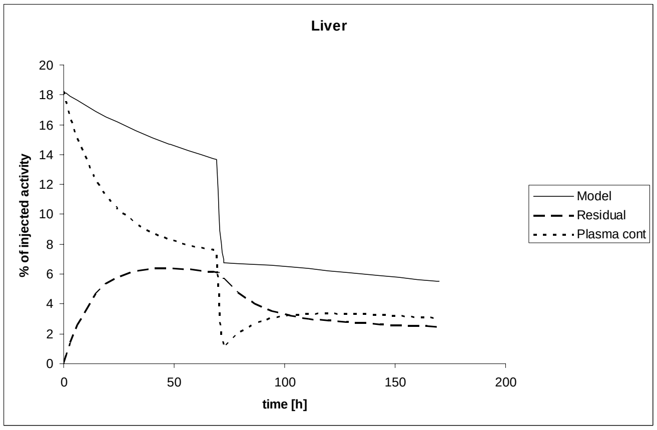
Liver
% of injected activity
0
2
4
6
8
10
12
14
16
18
20
0
50
100
150
200
time [h]
Model
Residual
Plasma cont

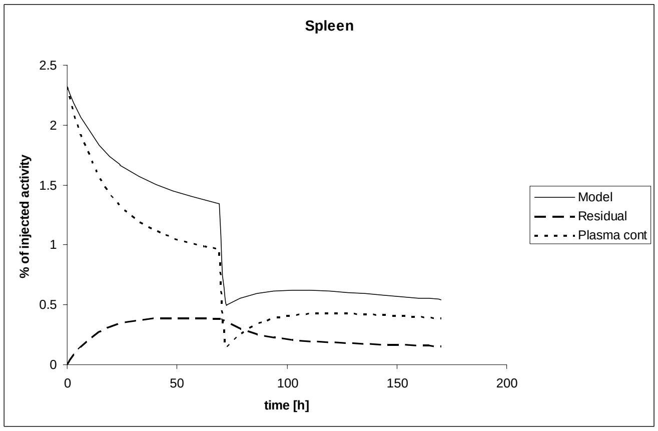
Spleen
% of injected activity
0
0.5
1
1.5
2
2.5
0
50
100
150
200
time [h]
Model
Residual
Plasma cont

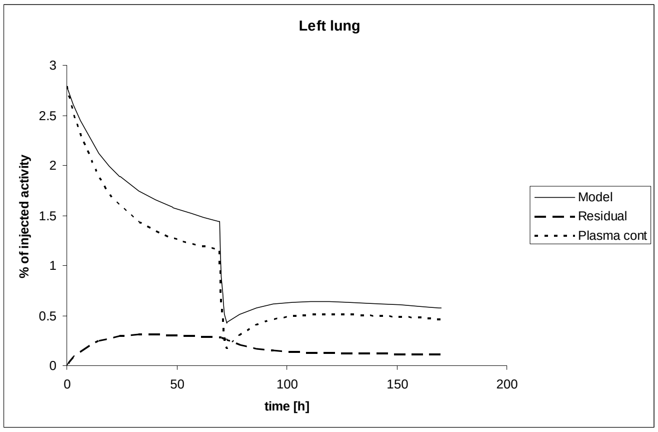
Left lung
% of injected activity
0
0.5
1
1.5
2
2.5
3
0
50
100
150
200
time [h]
Model
Residual
Plasma cont

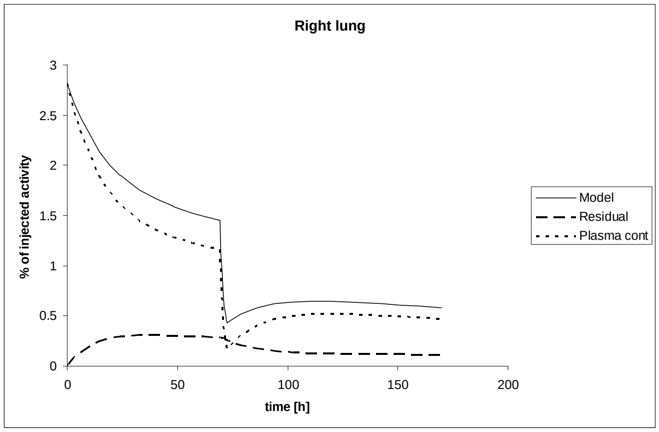
Right lung
% of injected activity
0
0.5
1
1.5
2
2.5
3
0
50
100
150
200
time [h]
Model
Residual
Plasma cont

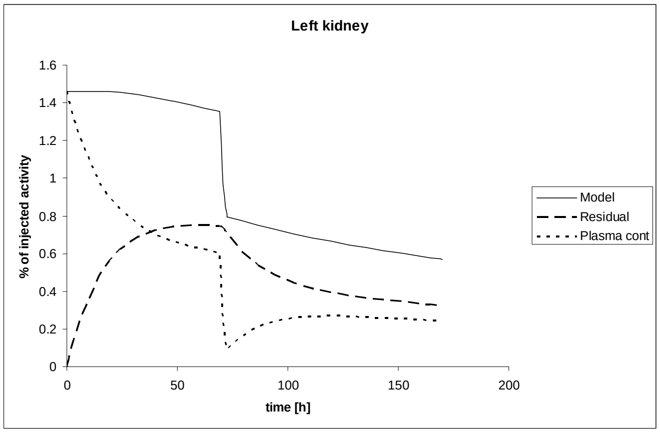
Left kidney
% of injected activity
0
0.2
0.4
0.6
0.8
1
1.2
1.4
1.6
0
50
100
150
200
time [h]
Model
Residual
Plasma cont

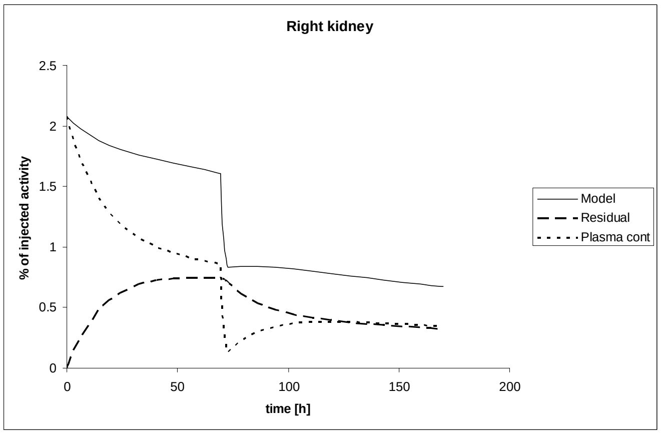
Right kidney
% of injected activity
0
0.5
1
1.5
2
2.5
0
50
100
150
200
time [h]
Model
Residual
Plasma cont

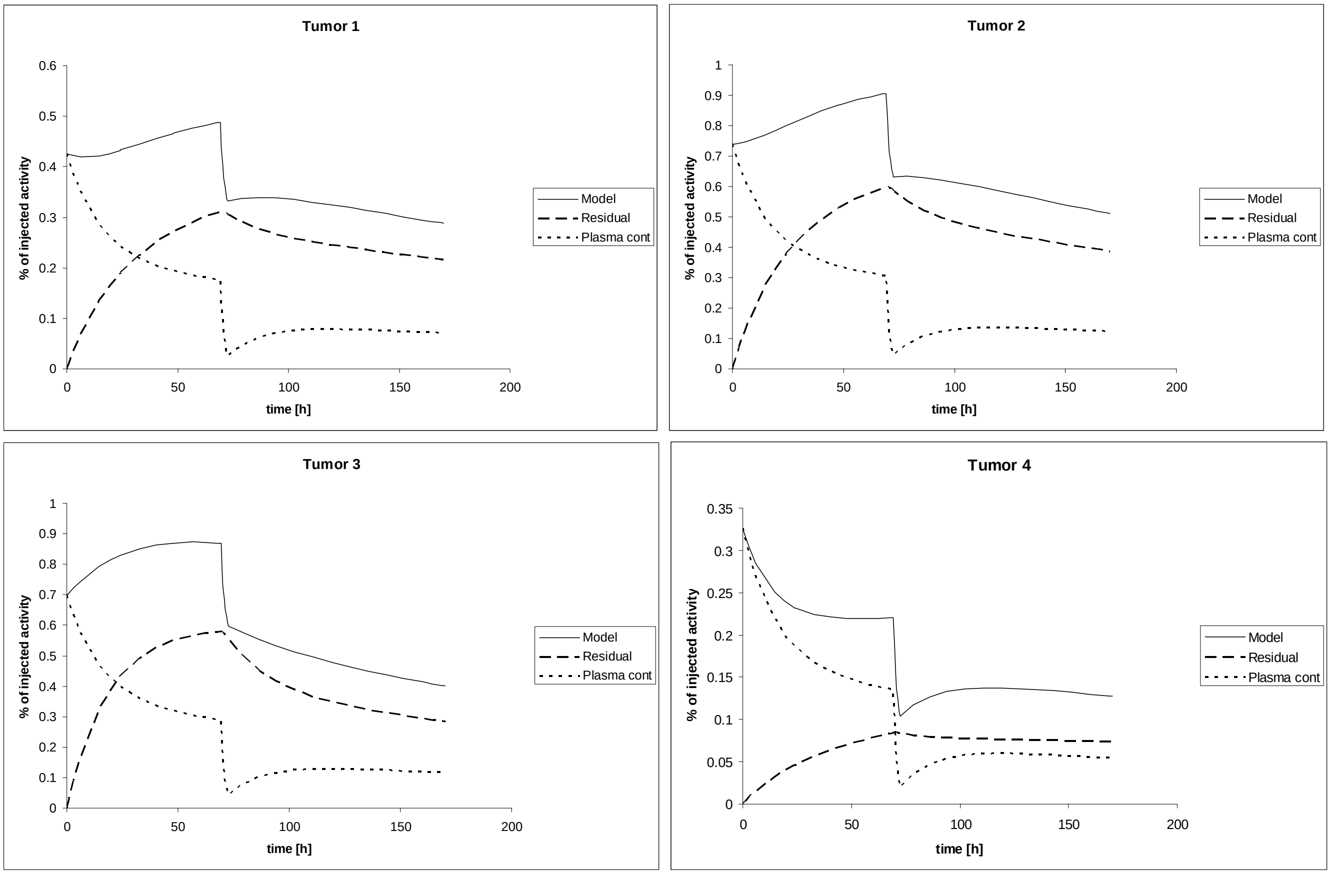

Fig A:11 Decay corrected plot for patient #7 (therapeutic part)

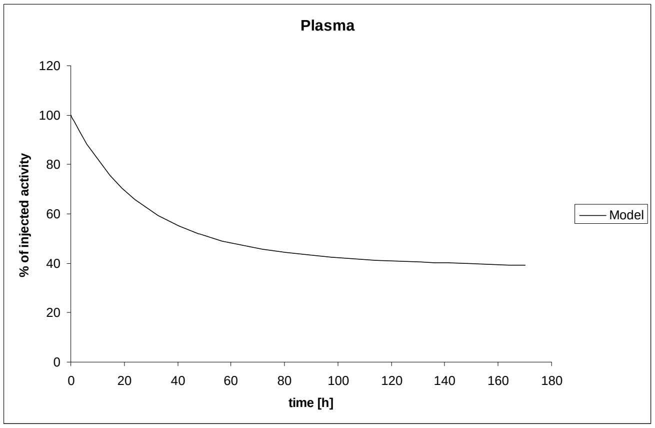

Plasma

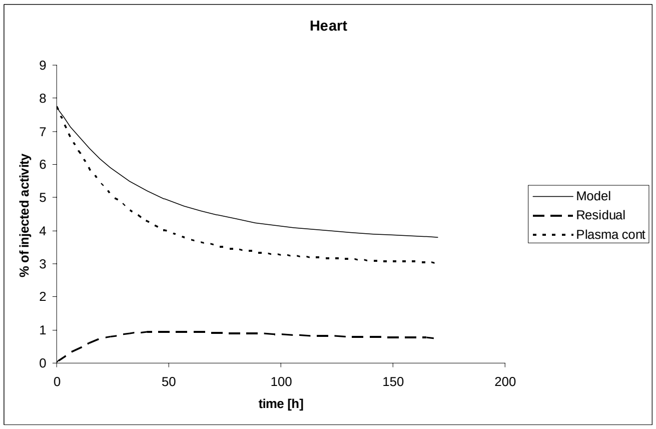

Heart

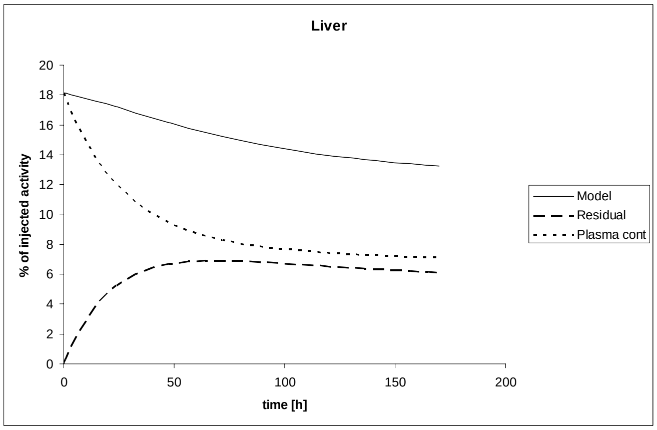

Liver

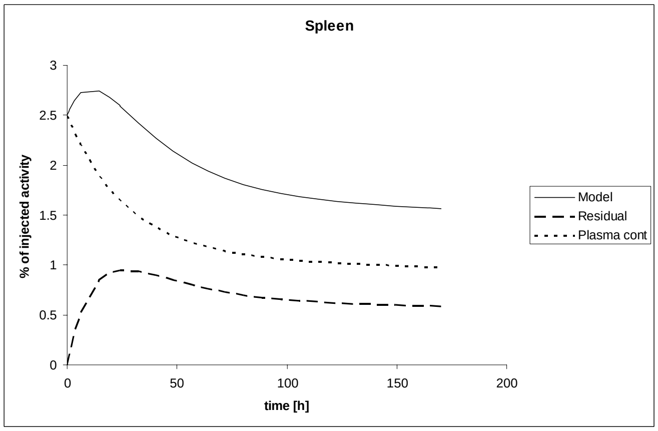

Spleen

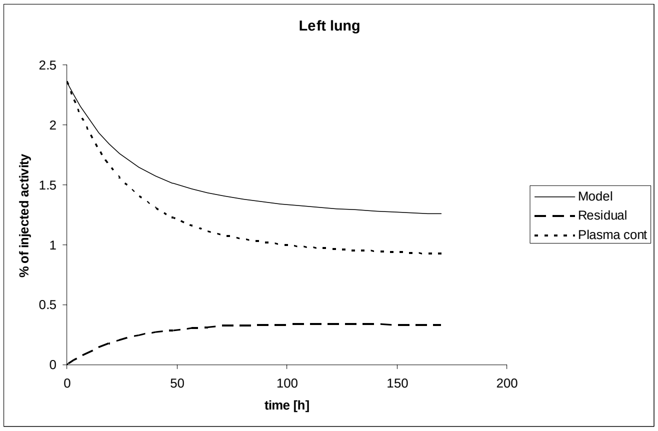

Left lung

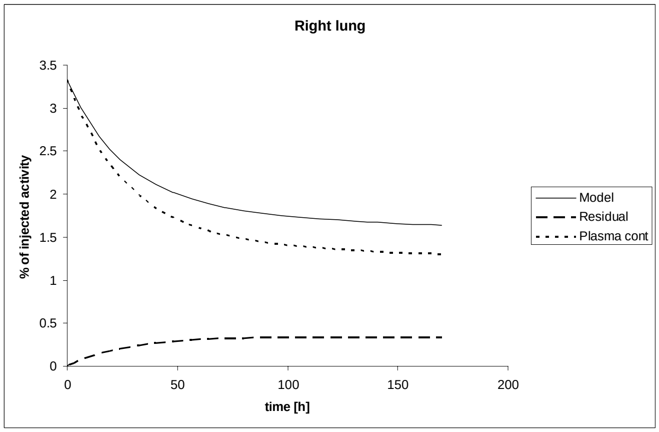

Right lung

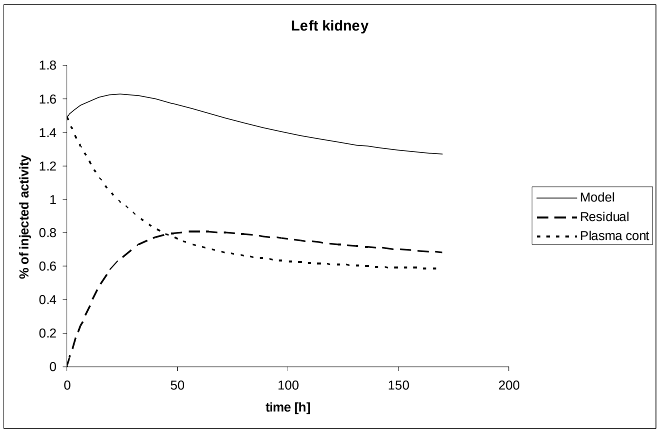

Left kidney

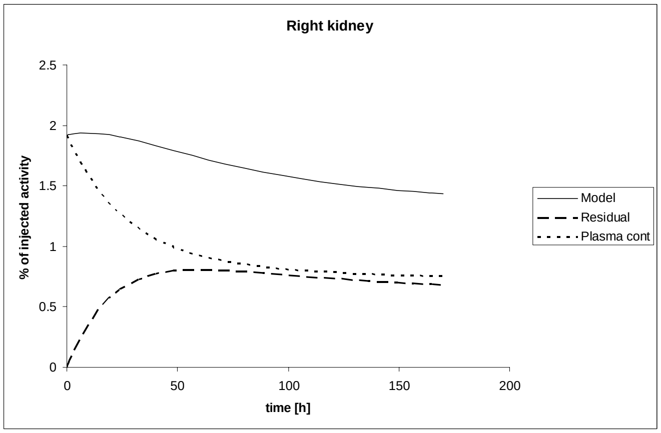

Right kidney

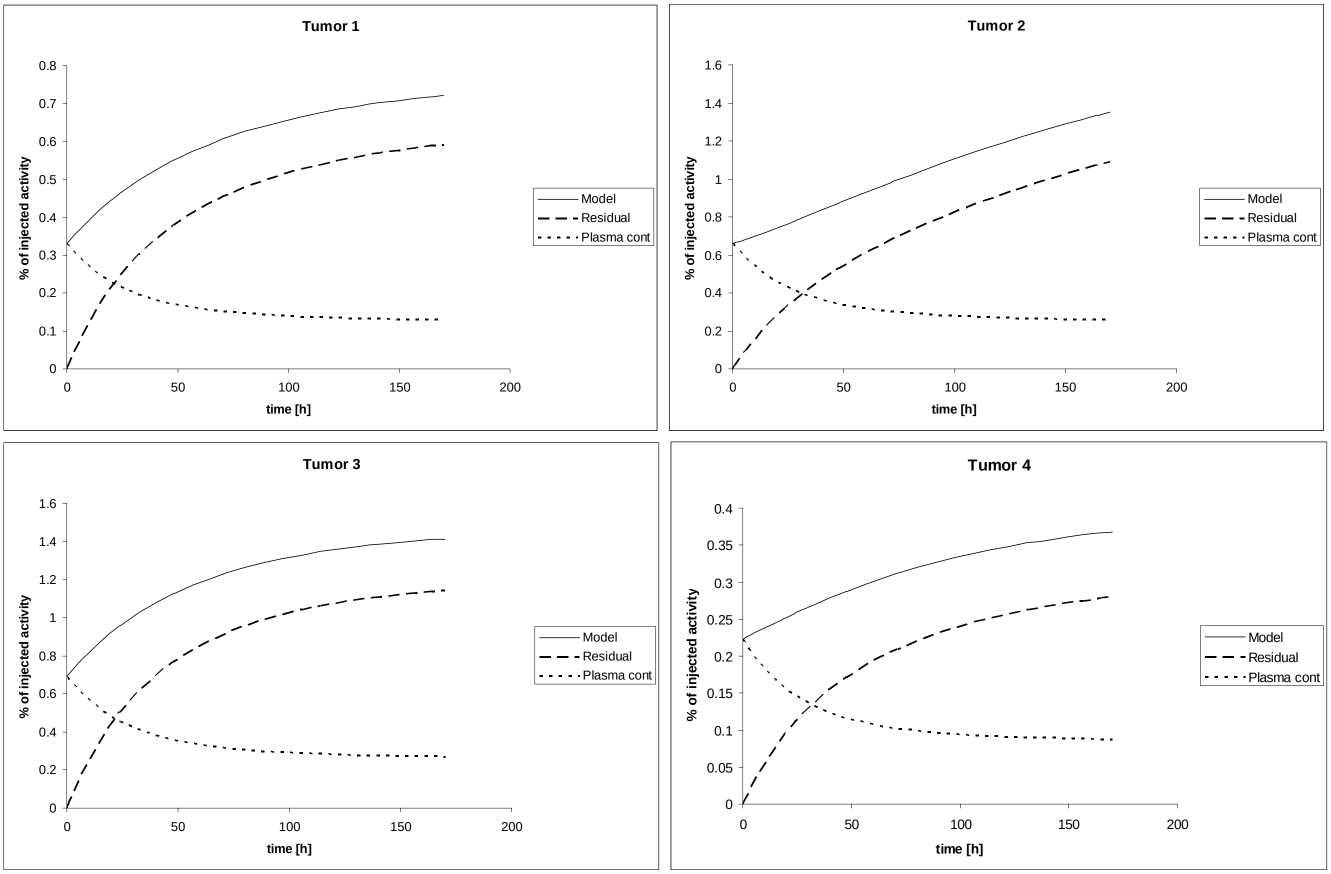

Fig A:12 Decay corrected plot for patient #7 (diagnostic part)

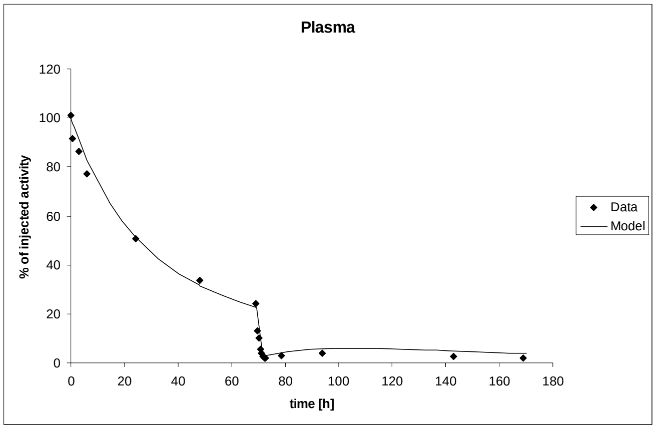
Plasma
% of injected activity
0
20
40
60
80
100
120
time [h]
0
20
40
60
80
100
120
140
160
180
Data
Model

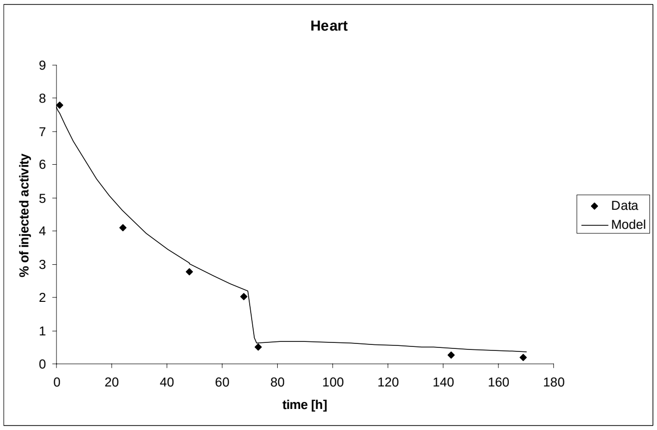
Heart
% of injected activity
0
1
2
3
4
5
6
7
8
9
time [h]
0
20
40
60
80
100
120
140
160
180
Data
Model

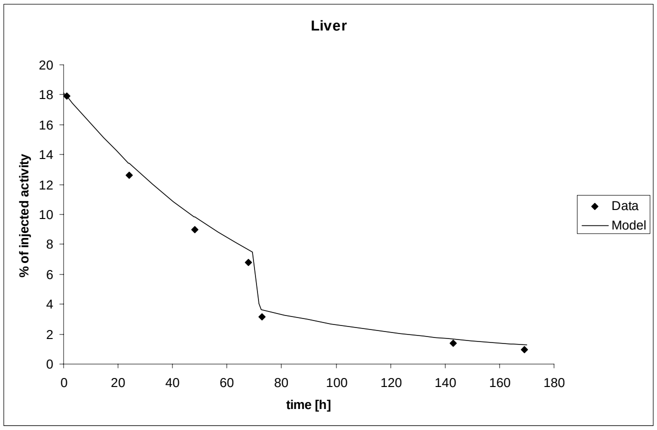
Liver
% of injected activity
0
2
4
6
8
10
12
14
16
18
20
time [h]
0
20
40
60
80
100
120
140
160
180
Data
Model

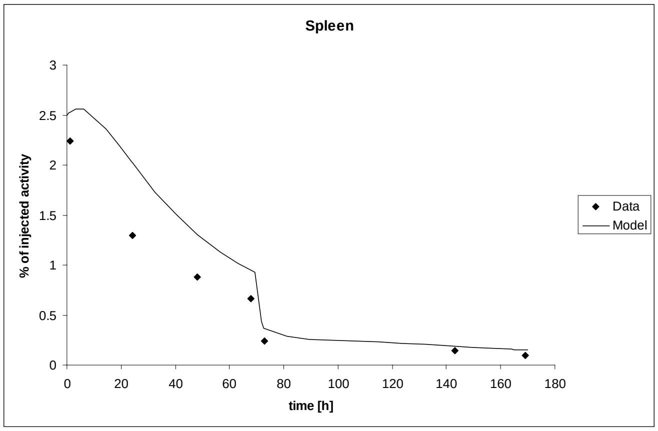
Spleen
% of injected activity
0
0.5
1
1.5
2
2.5
3
time [h]
0
20
40
60
80
100
120
140
160
180
Data
Model

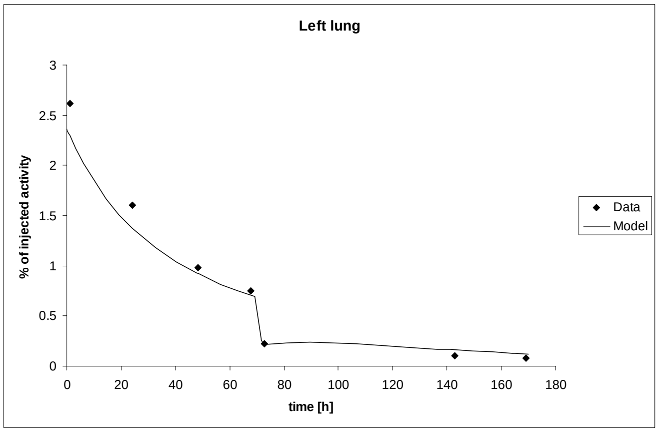
Left lung
% of injected activity
0
0.5
1
1.5
2
2.5
3
time [h]
0
20
40
60
80
100
120
140
160
180
Data
Model

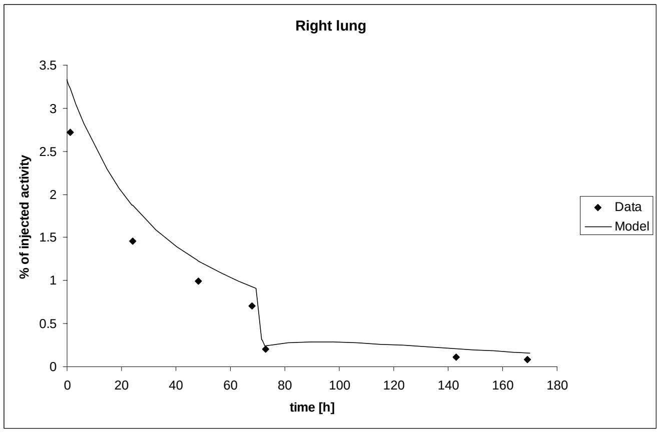
Right lung
% of injected activity
0
0.5
1
1.5
2
2.5
3
3.5
time [h]
0
20
40
60
80
100
120
140
160
180
Data
Model

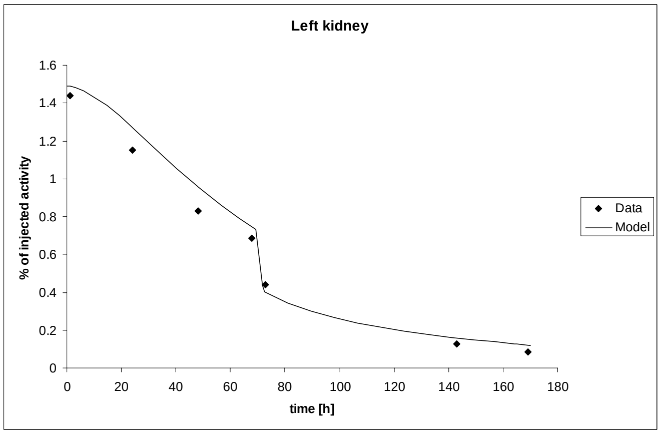
Left kidney
% of injected activity
0
0.2
0.4
0.6
0.8
1
1.2
1.4
1.6
time [h]
0
20
40
60
80
100
120
140
160
180
Data
Model

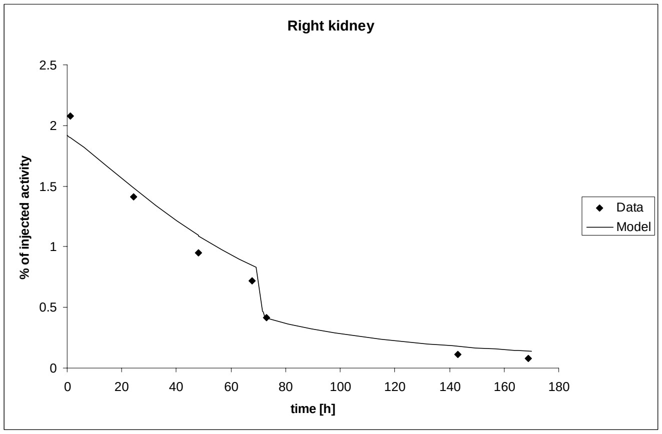
Right kidney
% of injected activity
0
0.5
1
1.5
2
2.5
time [h]
0
20
40
60
80
100
120
140
160
180
Data
Model

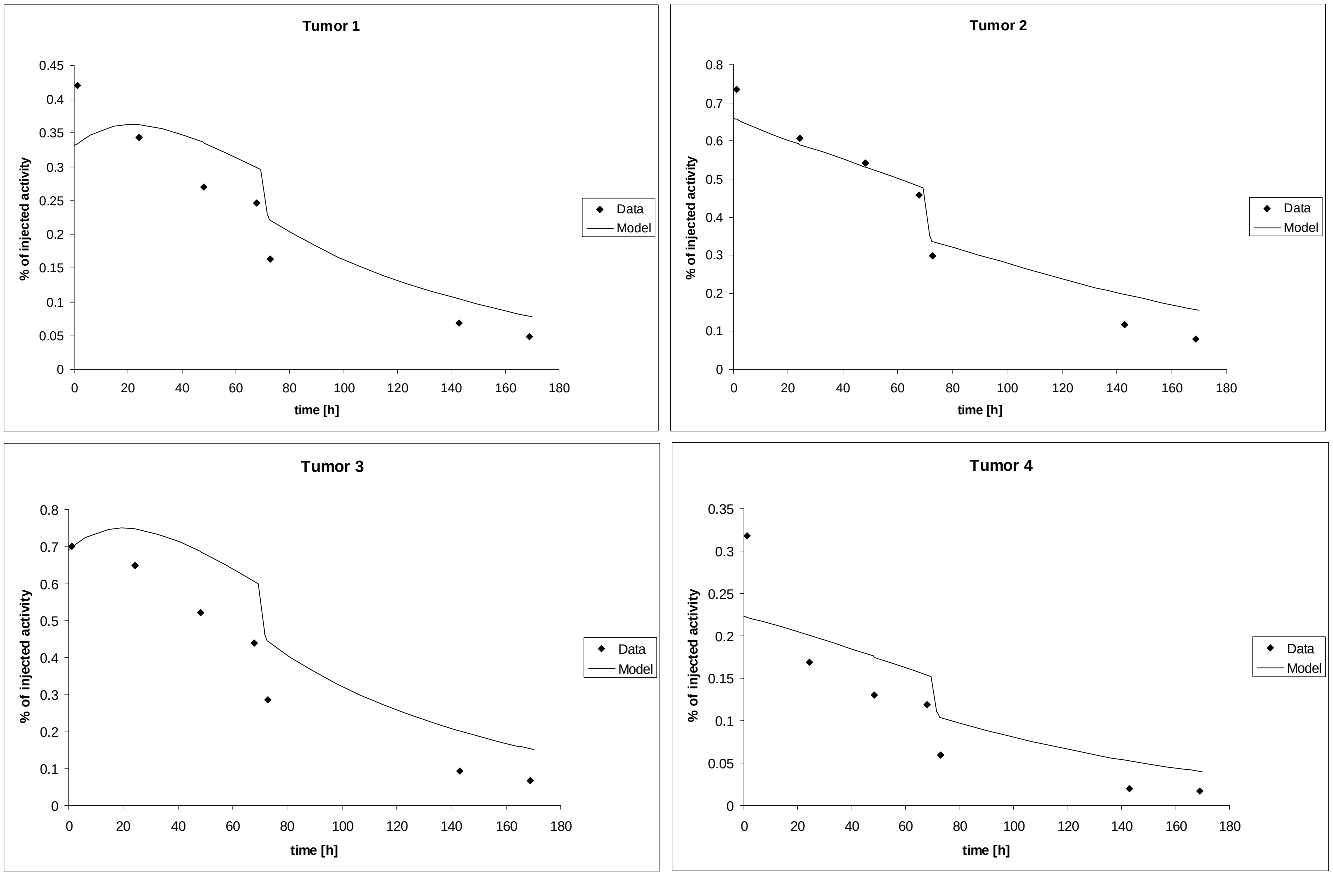

Fig A:13 Model prediction of ECAT for patient #7

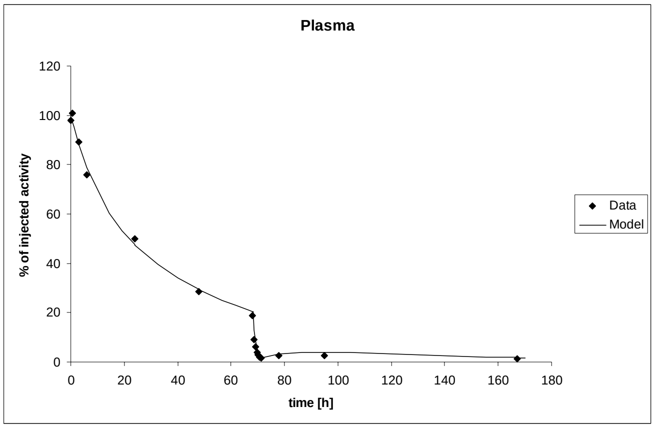
Plasma
% of injected activity
120
100
80
60
40
20
0
0
20
40
60
80
100
120
140
160
180
time [h]
Data
Model

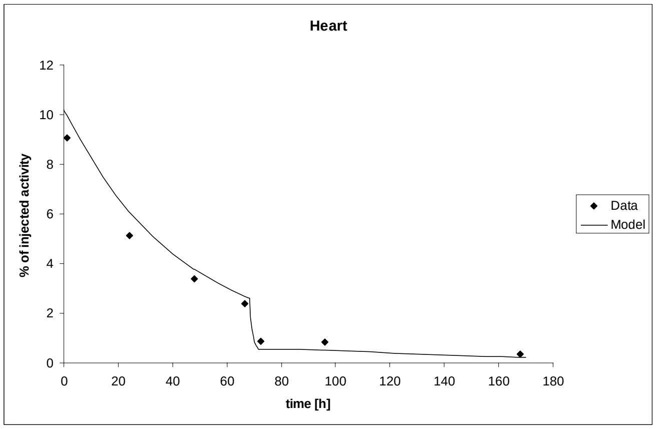
Heart
% of injected activity
12
10
8
6
4
2
0
0
20
40
60
80
100
120
140
160
180
time [h]
Data
Model

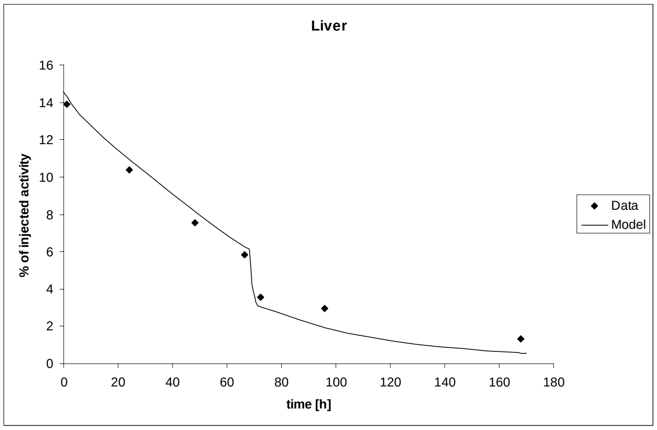
Liver
% of injected activity
16
14
12
10
8
6
4
2
0
0
20
40
60
80
100
120
140
160
180
time [h]
Data
Model

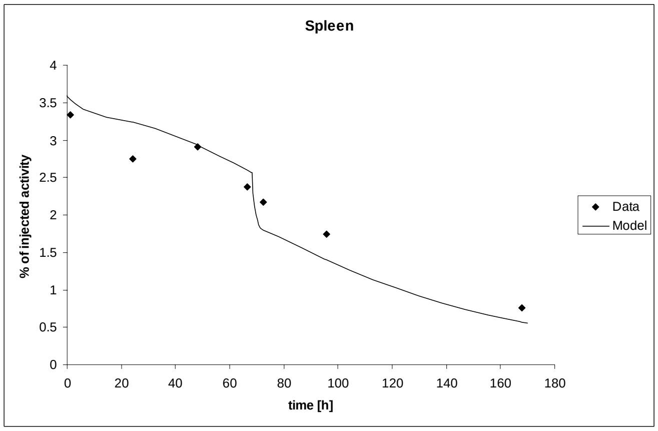
Spleen
% of injected activity
4
3.5
3
2.5
2
1.5
1
0.5
0
0
20
40
60
80
100
120
140
160
180
time [h]
Data
Model

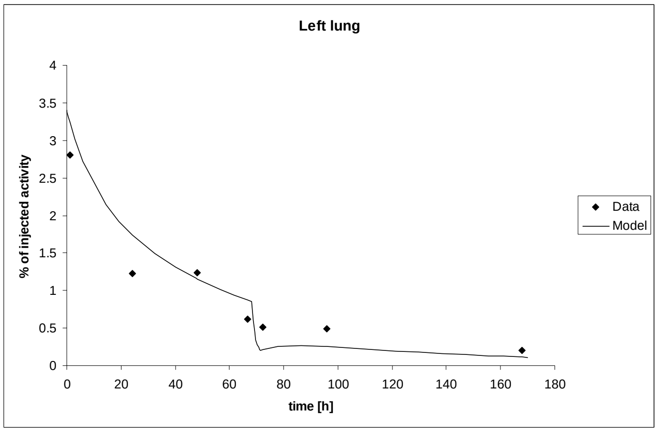
Left lung
% of injected activity
4
3.5
3
2.5
2
1.5
1
0.5
0
0
20
40
60
80
100
120
140
160
180
time [h]
Data
Model

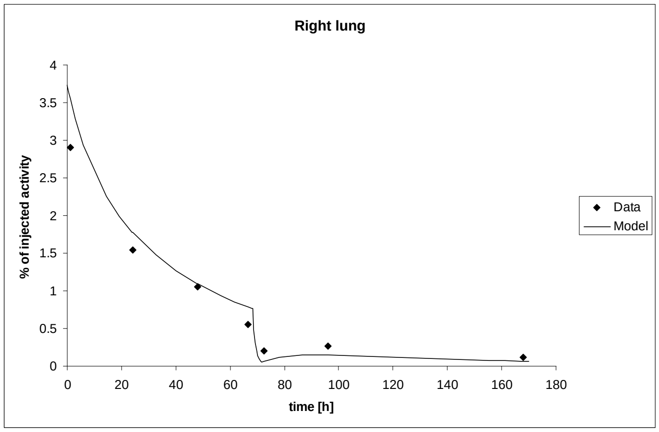
Right lung
% of injected activity
4
3.5
3
2.5
2
1.5
1
0.5
0
0
20
40
60
80
100
120
140
160
180
time [h]
Data
Model

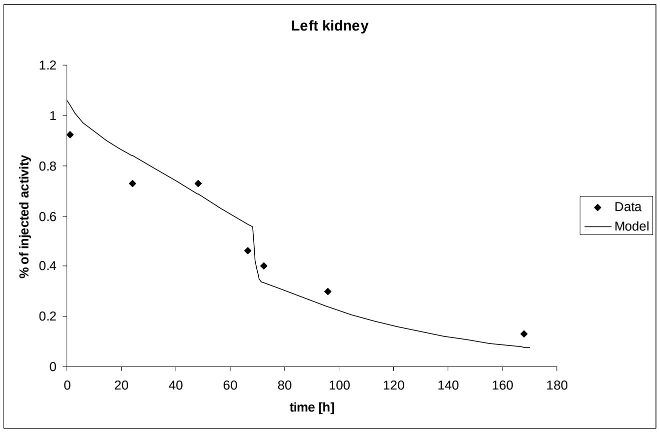
Left kidney
% of injected activity
1.2
1
0.8
0.6
0.4
0.2
0
0
20
40
60
80
100
120
140
160
180
time [h]
Data
Model

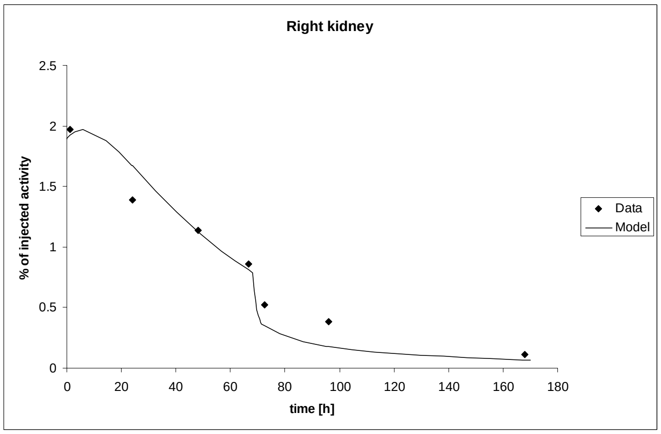
Right kidney
% of injected activity
2.5
2
1.5
1
0.5
0
0
20
40
60
80
100
120
140
160
180
time [h]
Data
Model

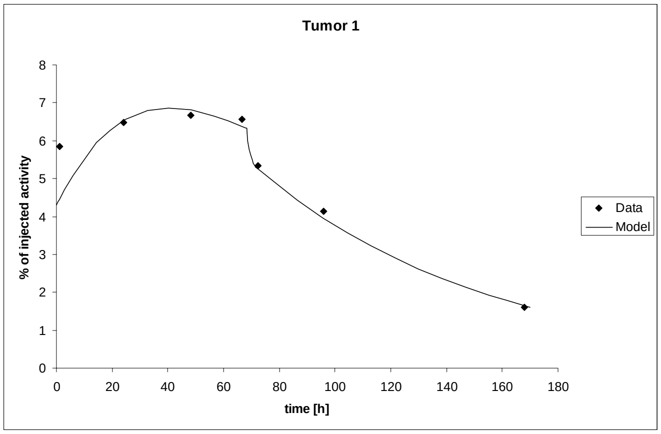

Fig A:14 Model prediction of ECAT for patient #8